Self-Healing Behavior in 12Cr Steels

Self-Healing Behavior in 12Cr Steels

by

Yang Su

to obtain the degree of Master of Science
at the Delft University of Technology,
to be defendend publicly on Monday May 30, 2022 at 9:30 hour.

Student number:	5157587	
Project duration:	September 20, 2021 - May 30, 2022	
Thesis supervisors:	Prof. dr. ir. S. van der Zwaag,	TU Delft, supervisor
	Dr. N. H. van Dijk,	TU Delft, supervisor
	P.h.D. candidate Y. Fu,	TU Delft, daily supervisor
Thesis committee:	Prof. dr. ir. S. van der Zwaag,	TU Delft, supervisor
	Dr. N. H. van Dijk,	TU Delft, supervisor
	Ir. J. Sinke,	TU Delft

Science is a wonderful thing
if one does not have to earn one's living at it.

Albert Einstein

Contents

Summary

Self-healing of creep-induced damage in newly designed 12Cr self-healing ferritic steels is studied. The damage healing is achieved by the segregation of supersaturated solute atoms at the free surface of the creep-induced cavities, and in this research, the healing phase is the W-riched Laves phase. Two kinds of self-healing steel with different precipitation driving forces of Laves phase are investigated, namely fast self-healing steel (FSHS) and slow self-healing steel (SSHS), in which the FSHS is designed to show the healing effect after 280 hours, while SSHS is designed to show healing effect after 27000 hours. Although both systems are self-healing systems, only FSHS is expected to show the self-healing phenomenon under the testing condition of this study, while SSHS not. Creep tests were performed on bone-shaped samples with constant stresses ranging from 100 to 260 MPa at 550 °C. The creep behavior is compared with traditional 9-12Cr ferritic steels, the relationship between the minimum creep rate and stress obeys Norton's power law, and the relationship between the lifetime and stress also obeys a power law. The total strain and stress exponents in power law of both SSHS and FSHS are relatively high compared to traditional 12Cr ferritic steel with similar grain size. The microstructure of the creep-failed samples, including the fracture surfaces, the uniformly-strained region (i.e., the stress-affected region), and the stress-free region are investigated with scanning electron microscopy (SEM). By comparing the feature of stress-affected region and stress-free region exposed to the same thermal history, the effect of high-temperature exposure could be isolated from this. The effect of stress on the Laves phase precipitation behavior and the damage evolution could be understood more clearly. For both the SSHS and FSHS, a ductile and transgranular fracture mode is confirmed by analyzing the fracture surfaces. In the stress-affected region and stress-free region of the creep-failed samples, $M_{23}C_6$ precipitates, Si/C-rich impurities, and pores were found in all observed samples. The Laves phase was only found in the samples with a longer lifetime ($>$ 300 h). A TEM observation and EDX scanning was conducted on the FSHS sample with a lifetime of 2487.2 hours. Laves phase precipitates were found on the grain boundaries and in the matrix, while no grain boundary cavities were found. Statistics based on pores observed on samples tested under different stress showed that the pores were present prior to creep tests and are generally not due to creep. A combined analysis of creep behavior and microstructure showed that dislocation climbing is likely the dominant creep mechanism. The absence of typical creep grain-boundary cavities was allocated to the relatively ductile matrix of 12Cr self-healing steel or the unfavorable dominating creep mechanism for creep cavity forming. With the prerequisite of self-healing not found in all tested samples, self-healing was considered not found under current testing conditions. The statistics based on the Laves phase showed that the precipitation depends on creep time, and the stress is in-

deed lowering the nucleation barrier, thus promoting the Laves phase to precipitate in the stress-affected areas.

1

Introduction

1

High-performance ferritic creep-resistant steel is one of the essential material categories in engineering applications, such as constructing a thermal power generating unit and the first-wall or blanket structure of fusion reactors. Two clear demand-led strategies in this material category can be seen throughout the development history. One is to increase the operating temperature to obtain higher heat efficiency of thermal power plants, as the turbine thermal efficiency is positively related to the steam temperature [1, 2], thus saving heat resources. Another trend is to substitute the alloying element with high activation, such as molybdenum (Mo) and niobium (Nb), by low activation elements such as tungsten (W) and vanadium (V) while maintaining the creep-resistant properties. By this strategy, the decommissioned nuclear reactor becomes more manageable and safer [3, 4]. Note that other performances such as tolerance of neutron-induced embrittlement and excellent corrosion resistance [5] are required for nuclear applications but not explicitly addressed in this review.

Ferritic creep-resistant steel with 9-12wt.% of chromium (Cr) is a steel family with over fifty years of developing history while remaining popular in constructing steam pipe of ultra-supercritical (USC) thermal generators and some other components due to its good thermal conductivity, low coefficient of thermal expansion, good fatigue-resistant properties, and relatively low-cost [6]. Besides, it is also finding its way into nuclear application. Many different alloying elements were added and optimized in order to enhance the effect of solid solution strengthening (e.g., Mo and W) [7] or precipitate strengthening (e.g., V and Nb) [8]. The ratio of compositions and heat treatments are also optimized to obtain desirable grain size and distribution of strengthening precipitates. [9] Those strategies collectively increase the creep lifetime by inhibiting the formation of damage and reducing the initial damage.

As an alternative design strategy to the ”damage prevention” scheme, self-healing based on ”damage management” conceptualized by Van der Zwaag in 2008 [10] has been widely studied over the last ten years. Many material classes have successfully implemented this designing concept to reach desirable healing properties, including polymers [11], concretes [12] and asphalts [13]. The self-healing materials mentioned above can partially or fully repair the damage during their service life. Such characteristics are highly desirable to high-temperature components, which require a typical lifetime of over 100,000 h [9]. Since in traditional creep-resistant steels, once the damage takes place, there is hardly any means to reverse the degradation of the material. Some undetected manufacturing flaws or creep damage formed at microstructural weak points could grow and propagate rapidly, causing the unexpected fracture. By implementing self-healing in the creep-resistant steels, such drawbacks could be compensated and increase the credibility of the nominal lifetime.

The implementation of self-healing in the creep-resistant steel is dedicated to creep damage filling. The tungsten-rich Laves phase is chosen as the healing agent. The tungsten is being brought into the supersaturated status before the service stage. Due to the sheer difference in atomic size between tungsten and iron, a significant strain energy barrier prevents tungsten from homogeneous precipitation

into Laves phase when there is no damage. When the creep cavity forms free surface within the material, the strain energy barrier is reduced and the Laves phase could precipitate at the cavity, thus perfoms the healing. Based on this strategy, a computational model was developed to design self-healing ferritic steels working under 550 °C with comparable composition as commercial creep-resistant ferritic steels [14]. A genetic algorithm was designed to enumerate and filtrate composition with decent mechanical properties among C, Cr, Mn, Si, and W within a certain proportion range. A few go/no-go criteria were set in the algorithm to ensure specific microstructure after annealing and during the in-service period. The compositions and corresponding solid solution strengthinging factors and precipitation hardening contribution factors were recorded. The Laves phase driving force was determined as the parameter to describe the healing efficiency. The Laves phase driving force was related with strenghtening factors, and a few candidates with similar mechanical properties but different healing efficiency was selected manually.

In this thesis, two kinds of 12Cr self-healing ferritic steels with different precipitation driving forces of Laves phase, namely fast self-healing steel (FSHS) and slow self-healing steel (SSHS), designed by this computational model, were put to the creep tests at 550 °C under different stresses. The FSHS is designed to show the healing effect after 280 hours, while SSHS is designed to show healing effect after 27000 hours. Only FSHS is expected to show healing effect within the time limit of this study. The creep data were collected and compared with commercial steel. The creep failed samples were observed on the fracture surface, the uniformly-strained region (i.e., the stress-affected region), and the stress-free region using scanning electron microscopy (SEM) and transmitting electron microscopy (TEM). The damage evolution of FSHS and SSHS in the stress-affected region and stress-free region were investigated and compared. The behavior of Laves phase was also investigated in FSHS on both stress-affected and stress-free regions to find the filling of cavities by Laves phase, as it is designed to show healing behavior within the time scale of this study.

The thisis starts with theoretical background on creep deformation in 9-12Cr ferritic steel, current theories on creep cavity nucleation and growth, the strengthening mechanisms in traditionally designed 9-12Cr creep-resistant steel, and factors related creep-resistant properties (Chapter 2). Then, the mechanism and design strategies of self-healing in creep-resistant steel are introduced, together with previous development in self-healing model alloys and detailed illustration of the computational model used to design the self-healing systems tested in this thesis (Chapter 3). Subsequently, the experiment detail is introduced, including geometry specifications and heat treatment of the creep samples, creep experiment setups and microscopy setups (Chapter 4). Then, the creep results and microstructural observations of FSHS and SSHS are presented (Chapter 5). The analysis of creep data, discussion on damage evolution and Laves phase precipitation behavior based on microscopy results are presented in the following chapter (Chapter 6). Finally, the conclusions and recommendation for next generation of SH steels are drawn.

2

Creep Deformation

2

Creep is a phenomenon in which a material undergoes time-dependent plastic deformation under constant stress below the quasistatic yield stress at an elevated temperature. The elevated temperature is often quantified by the homologous temperature, which is defined as $T_h = T/T_m$ in which T is the test environment temperature, and T_m is the melting temperature of the material (both in Kelvin). Often, creep starts to greatly influence the design when the homologous temperature reaches beyond 0.4, which is a rule-of-thumb from an engineering point of view. Indeed, there were researches showing creep phenomenon in steels below this temperature [15], but it is not the major concerning aspect in this research. One of the engineering application examples is the main steam pipe in USC thermal power plant, the steam temperature in the pipe can reach 600-650 °C, and the melting temperature for one of the most widely used ferritic creep-resistant steel P92 is about 1370 °C. In this case, the homologous temperature is around 0.44-0.47, and with the existence of steam pressure, creep degradation constantly erodes the material's performance. Therefore, creep is one of the dominant damage effects limiting these components' lifetime.

This section focuses fundamental aspects of creep in ferritic creep-resistant steels.

2.1. Overview of Creep

2.1.1. Three Stages of Creep

The process of creep can generally be divided into three regions, as shown in Figure 2.1.

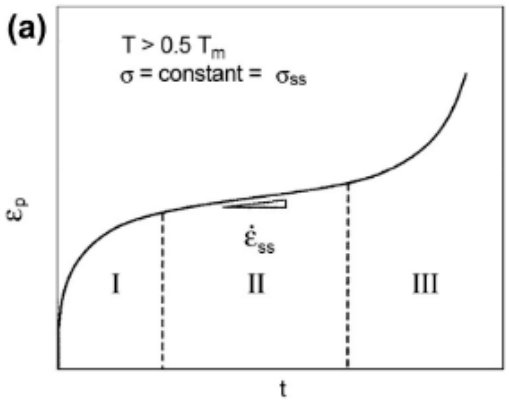

Figure 2.1: Strain-time curve for constant true stress in pure and class M metals [16]

In the first stage, the strain rate decreases with increasing strain or time; this stage is also known as primary creep or transient creep. In this stage, the strengthening mechanisms surpass the softening mechanisms at the beginning. The activation of primary glide systems causes a high initial creep rate. The primary dislocations become mobile and adapt to the tensile deformation. Meanwhile, the

Frank-Read source can multiply the primary dislocations during the deformation and increase the resistance towards deformation. This process is called work hardening, causing the creep rate to decrease with time. However, the strengthening effect does not always surpass the softening effect at an elevated temperature. The recovery (annihilation) of dislocation caused by diffusion also softens the material during this process. Two factors slowly reach an equilibrium at the end of the first stage, and the equilibrium indicates the start of the second stage.

In the second stage, known as the steady-state creep, the strain rate tends to be constant. This stage usually takes up most of the creep lifetime. In this stage, softening mechanisms such as dislocation climb and dislocation annihilation maintain balance with strengthening mechanisms, and dynamic equilibrium between strengthening and softening is established.

In the third stage, also known as the tertiary stage, the creep rate increases rapidly, eventually leading to fracture. In this stage, creep cavities previously formed coalesce and reduce the material strength significantly. The actual stress also increases considerably due to local shrinkage of the cross-section (i.e., necking). Final fracture is usually caused by insufficient fracture toughness to prevent catastrophic failure due to the coalesced grain pores having reached the critical size.

2.1.2. Creep Behavior of Ferritic Steels

Power-law creep, a largely phenomenological relationship between the steady-state strain rate $\dot{\epsilon}_{ss}$ and stress σ_{ss} was described in [17] (shown as equation 2.1) and was consistent with Norton's Law first proposed it in 1929 [18].

$$\dot{\epsilon}_{ss} = A_0 exp[-Q_c/kT](\sigma_{ss}/E)^n \tag{2.1}$$

where A_0 is a constant, k is Boltzmann's constant, E is Young's modulus, and Q_c is the activation energy for creep. This relationship is also conveniently named five-power-law because exponent n is about 5 (4-7) for pure metals, ceramic, and other alloys over a relatively wide range of creep temperatures and strain rates [17]. However, the name of this creep relationship does not show any of the microstructural mechanisms. In fact, the underlying mechanism is still under debate. In some of the "mechanism-wise" creep categorize methods [19], creep can be divided into solid state diffusion dominated creep and dislocation motion dominated creep. The solid state diffusion dominated creep includes Nabarro-Herring creep, and Coble creep, in which the stress exponent is 1; the dislocation motion dominated creep includes many other creep phenomena with their stress exponent higher than 3, five-power-law naturally falls into this category according to the definition. However, some [17] claim that such categorize method may be misleading as dislocation climb control appears to occur in other regimes such as Harper-Dorn creep, superplasticity, power-law break down (PLB), etc. Furthermore, an excellent correlation has been found between the activation energy for five-power-law creep Q_c and self-diffusion Q_{sd} for over 20 kinds of metals, as shown in Figure 2.2. On the other hand, some experimental observations on microscopic local effective stress during secondary creep showed that it produces dislocation emission and controls

the creep rate [20]. Though the correlation between Q_c and Q_{sd} becomes a consensus, experimental evidence on dislocation dominance is still not to be ignored and adopted by many researchers. The mechanism involved in power law creep could be material specific, temperature specific, and stress specific.

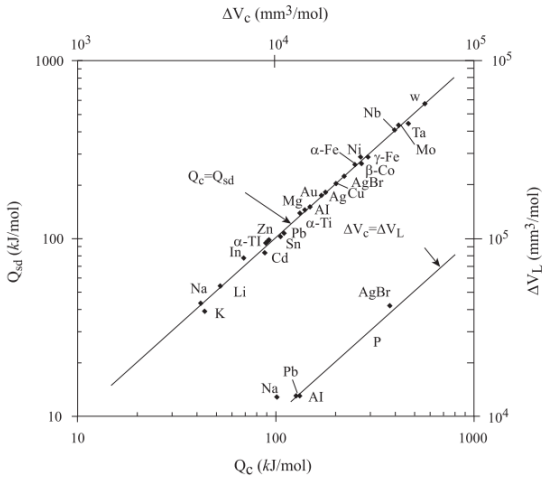

Figure 2.2: The activation energy and volume for lattice self-diffusion versus the activation energy and volume for creep. [21]

For some of the ferritic creep-resistant steels working in their designed environment, the steady-state creep region is sometimes absent due to instability of the microstructure at elevated temperature, and no dynamic microstructural equilibrium is reached [9]. Such continuous change in creep rate is more evident in the creep rate-time graph than a strain-time graph, as shown in Figure 2.3. Therefore, the terminology ”minimum creep rate” is sometimes more informative than ”steady-state creep rate” when estimating the creep lifetime of the steels.

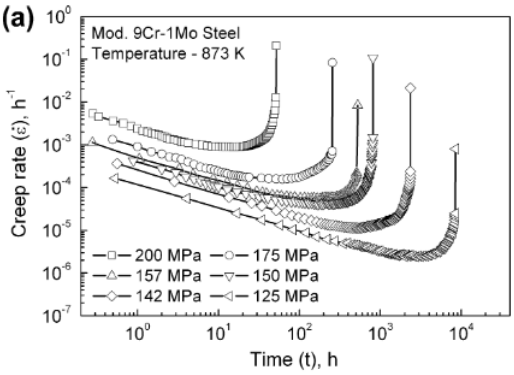

Figure 2.3: Creep rate-time curve for a 9Cr creep-resistant steel at different applied stresses [22]

Even so, a generalized power law was still found between minimum creep rate and applied stress at a fixed temperature in many of the reported chromium-containing ferritic steels. Choudhary and Isaac Samuel [22] investigated the creep behavior of a modified 9Cr-1Mo ferritic steel. The result showed that the stress dependence of the minimum creep rate followed Norton's power law. The exponents for 550°C, 575°C, and 600°C were 12.9, 12.7, and 12.4, respectively. Similarly, the rupture life dependence on stress obeys the power-law but slightly different exponents. Sklenička et al. [23] also reported that the power-law stress exponent of P91 and P92 under test temperature of 600°C could vary between 12 and 18 for the high-stress region ($\sigma \geq 100$ MPa). The investigation conducted by Abe and Nakazawa [24] on the effect of tungsten on the creep behavior of ferritic steel also shows a power-law relationship between rupture life and stress. Ferritic steels with higher chromium content, for instance, 12Cr [25], collectively show power-law behavior. Similar creep characteristics were also found in some other studies for ferritic creep-resistant steels [23, 26].

When discussing one material under a constant temperature, the equation can be written more simply by compressing the constants mentioned above into constant A, as shown in equation 2.2.

$$\dot{\epsilon}_{min} = A\sigma^n \tag{2.2}$$

As the total failure strain in creep loading is often constant (i.e., independent of the imposed stress), a power-law can also be found between time to rupture and imposed stress, as shown in equation 3.

$$t_R = A'\sigma^{-n} \tag{2.3}$$

2.2. Creep Damage Mechanisms

Characterizing creep cavities is essential to evaluate the self-healing effect. Therefore, this section is dedicated to collecting and understanding the creep damage and cavitation mechanisms. According to the investigation on 12Cr steel tested above 600°C conducted by Wu and Sandström [27, 28], the number of cavities per unit area, mean cavity diameter, and cavitated area fraction are positively related to strain or creep time in 12Cr steel. At the same strain, the number of cavities per unit area is dependent on the material and test conditions. The cavity nucleation rate is dependent on the stress and temperature; decreasing the temperature or stress will prolong the time available for cavity nucleation [27]. The larger average cavity size at a given strain is obtained at lower stress levels if the stress sensitivity of the creep rate is high [29]. The grain boundary creep cavities were reported in [30] when testing P91 steel under 66 MPa at 650 °C, while no creep cavities were reported in [22] when testing P91 steel under 125-200 MPa at 650 °C. In general, longer creep time and larger strain tend to lead to more severe creep damage. The average creep cavity size depends on the stress sensitivity of the creep rate.

2.2.1. Nucleation of Creep Cavities

Although the creep cavity nucleation mechanism is still not fully classified, there are three generally recognized mechanisms of creep cavity nucleation, namely:

- Vacancy accumulation
- Grain Boundary Sliding
- Dislocation Pile-ups (Zener-Stroh mechanism)

The mechanisms mentioned above are schematically shown in Figure 2.4a-c. A schematic figure of combined cavity nucleation mechanism working on a particle-obstacle is also shown in Figure 2.4d.

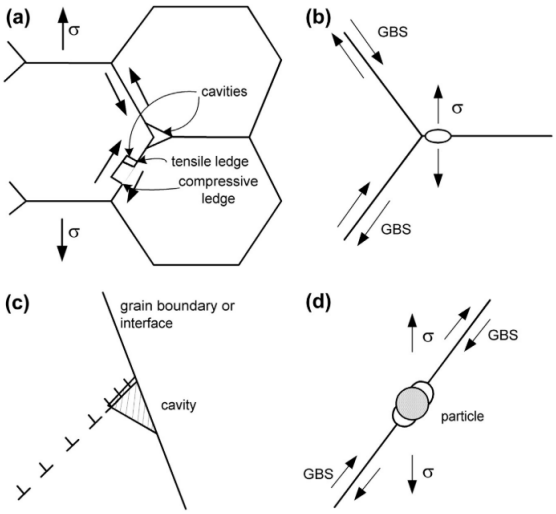

Figure 2.4: Cavity nucleation mechanism. (a) Sliding leading to cavitation from ledges (and triple points). (b) Cavity nucleation from vacancy condensation at a high stress region. (c) Cavity nucleation from a Zener-Stroh mechanism. (d) The formation of a cavity from a particle-obstacle in conjunction with the mechanisms described in (a–c). [31]

Vacancy Accumulation

The vacancy accumulation theory was developed by Raj and Ashby [32] in an attempt to build a creep lifetime prediction model considering microstructural evolution during creep. The theory was based on the free energy change of the system due to the formation of voids. A direct relationship was built between nucleation rate and applied stress with the geometry of the cavity considered. There are three parts of the energy related to the nucleation of a void in a grain boundary with the presence of tensile stress σ_n: (a) the work done by the system to its surroundings, (b) the interface energy, (c) the elastic energy. The elastic energy is usually neglected since it is much smaller compared to the energy term in (a). The change in free energy for the nucleation of one void can be expressed as:

$$\Delta G = -V\sigma_n + S\gamma - B\gamma_B \tag{2.4}$$

In which V is the volume of the void, S is the surface area of the void, B is the area of the grain boundary which the void occupies, γ is the surface free energy per unit area of the matrix material, and γ_B is the interface free energy per unit area of the matrix grain boundary. The geometry parameters (V, S, B) mentioned above are related to the radius of the void surface r, and the angle at the junction of the void and the grain boundary α. Specific expression can be found in [32]. The critical radius of the nucleated void can be obtained when ΔG reaches the maximum ΔG_c, as shown in equation 2.5, in which V_c is the critical volume of the void. The critical radius is shown in equation 2.6.

$$\Delta G_c = \frac{V_c \sigma_n}{2} \tag{2.5}$$

$$r_c = \frac{2\gamma}{\sigma_n} \tag{2.6}$$

A void can only proceed into the growth phase if its radius exceeds the critical radius. Otherwise, it re-dissolves into the matrix. The number of critical nuclei per unit area is given by

$$\rho_c = \rho_{max} exp(-\frac{\Delta G_c}{kT}), \tag{2.7}$$

in which ρ_{max} is the maximum number of potential nucleation sites at the grain boundary per unit area. The nucleation rate can be calculated by ρ_c times the time-dependent probability, which is related to boundary self-diffusion coefficient, D_{gb}, and the probability of finding a vacancy at the perimeter of the nucleus with critical size. By assuming uniform nucleation over the creep lifetime, the nucleation rate can be written in a more concise form, as shown in equation 2.8 proposed by Kassner [31].

$$\dot{\rho} = \rho_c D_{gb} \tag{2.8}$$

Grain Boundary Sliding (GBS)

The effect of grain boundary sliding (GBS) in cavity nucleation is still largely unclear. Although GBS could lead to stress concentrations at the conjunction points of the grain boundaries and hard particles, there were debates on whether the stress is sufficient enough to nucleate cavities [33, 34]. The ”transverse” boundaries, which represent boundaries perpendicular to the tensile direction in some of the 2D observation techniques, tend to nucleate cavities without obvious GBS[35]. On the other hand, an experiment conducted on bicrystal copper showed that the specimen prestrained in favor of GBS and subsequently subjected to stress normal to the sliding direction nucleate more cavities than the specimen that had not been subjected to GBS [33]. The grain boundary sliding could affect the creep cavity nucleation since it at least promotes the stress concentration at the weak points, but no numerical relationship was built like the vacancy accumulation theory.

Dislocation Pile-Ups

The dislocation pile-ups theory is widely accepted as a mechanism explaining vacancy accumulates at the hard second phase particles at transverse grain boundaries [31]. The dislocation pile-ups can lead to cavitation related to hard particles inside the grain as well, but without fast diffusion paths such as grain boundaries, the nucleated cavities may not expand as fast as the cavities nucleated at the boundaries. The Zener-Stroh mechanism (a dislocation-related cavity nucleation mechanism under room temperature) could also be in effect during high temperature creep since more cavities were found in ambient temperature prestrained specimens as reported [36]. Dyson [37] showed that the nucleation process could be continuous throughout creep, and the growth and nucleation of the cavity could happen simultaneously; this is also agreed by some other researchers [34, 38]. The predisposition for creep cavitation of dislocation-abundant specimen combined with continuous nucleation perspective leads to the point of plasticity controlled nucleation under the dislocation pile-ups theory [31], and this point consists with some of the experimental observations [39, 40]. As a result, the dislocation pile-ups mechanism is considered to be a plasticity-controlled nucleation process that requires the interaction between obstacles and the Zener-Stroh mechanism.

Although the nucleation mechanism is still not fully understood, the prevailing theories could point out the sites prone to nucleate creep cavities, namely rigid inclusions at the grain boundaries and conjunction points of the grain boundaries. The critical size of nucleated voids was predicted to be 2-5nm [41]. Based on these theories, qualitative or quantitative predictions on the newly developed creep-resistant steel are possible.

2.2.2. Growth of Creep Cavities

As briefly mentioned before, cavity nucleation is generally considered a continuous procedure during creep, and creep cavities form at a very early stage of creep. The subsequent creep damage leading to fracture could involve more influence of creep cavity growth. As the understanding of the microstructural evolution mechanisms went deeper, many cavity evolution-based computational models were developed to predict the creep lifetime [42, 43], some dedicated to 9-12Cr ferritic creep-resistant steels [27, 28, 44] and provided relative accurate results. The computational model predicting the cavity nucleation rate, number density, and size distribution was also developed [30]. The cavity growth mechanism can be divided into four categories, namely:

- Diffusion-controlled growth
  - Unconstrained diffusional growth
    - Grain boundary (GB) diffusion-controlled growth
    - Surface diffusion-controlled growth
  - Constrained diffusional growth
- Grain boundary sliding

- Plasticity-controlled growth
- Coupled diffusion and plastic growth

Unconstrained Diffusional Growth

Grain Boundary Diffusion-Controlled Growth The grain boundary diffusion-controlled growth theory was first proposed by Hull and Rimmer in 1959 [45]. It was believed that the cavity growth at the grain boundaries at elevated temperatures involves vacancy diffusion. The nucleated voids diffuse by surface migration and subsequent transport through GB with applied external stress, σ. The growth rate of a void is determined by the gradient of chemical potential, ∇f. The diffusion flux, J_{gb}, in the grain boundary is given in equation 2.9.

$$J_{gb} = -\frac{D_{gb}}{\Omega kT}\nabla f \tag{2.9}$$

In which D_{gb} is the grain boundary diffusion coefficient, Ω is the atomic volume, k is the Boltzmann's constant, T is the temperature. At the grain boundary, the potential is given by $f = -\sigma_n\Omega$. σ_n is the local normal-tension stress acting across the boundary. At a point far away from the void, it was estimated to have a maximum value of $(\sigma - P)$, in which P is the hydrostatic pressure. On the surface of a void, the potential is $f = -2\gamma\Omega/a$, in which a is the cavity radius, and γ is the surface free energy per unit area of the matrix material as mentioned before. Therefore, the approximation of ∇f can be given as

$$\nabla f \sim -\frac{\Omega}{\lambda_s}(\sigma - P - \frac{2\gamma}{a}), \tag{2.10}$$

in which λ_s is the cavity separation. The diffusion flux is then approximated as

$$J_{gb} \sim \frac{D_{gb}}{kT\lambda_s}(\sigma - P - \frac{2\gamma}{a}). \tag{2.11}$$

Notice that the a crtical stress $(\sigma_c = 2\gamma/a)$ is needed for the cavity to grow, which is consistent with the vacancy accumulation theory in the situation that hydrostatic pressure can be ignored. For a spherical cavity, the rate of growth is given as

$$\frac{da}{dt} \cong \frac{(D_{gb}\delta)(\sigma - P - \frac{2\gamma}{a})\Omega}{2kT\lambda_s a}, \tag{2.12}$$

in which δ is the width of the grain boundary. A schematic illustration of the basic concept in this theory is shown in Figure 2.5.

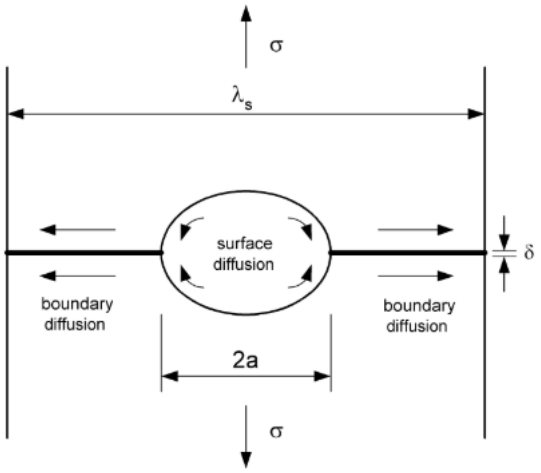

Figure 2.5: Cavity growth from vacancy diffusion across the cavity surface and through the grain boundaries due to a stress gradient. [31]

Surface Diffusion-Controlled Growth Unlike the GB diffusion-controlled growth theory, the surface diffusion-controlled growth suggests that the growth of cavity is actually controlled by surface diffusion, which leads to a 3-power stress relationship for cavity growth at low stresses, as shown in equation 2.13. [46].

$$\frac{da}{dt} \cong \frac{\Omega \delta D_s}{2kT\gamma_m^2}\sigma^3 \tag{2.13}$$

where D_s is the diffusion coefficient on the surface, and the rest symbols remain the same meaning as mentioned before. The exponent for stress will change to 1.5 at higher stresses. This theory is not widely accepted as the experimental evidence is not clear. In the observed 3-power stress-dependent cavity growth, the diffusion coefficient is higher than the surface diffusion coefficient [31]. It is necessary to note that the growth rate of the creep cavity presented by 2.12 and 2.13 are inconsistent with Monkman-Grant phenomenology, which suggests that the growth rate should be proportional to the stress with an exponent of five. The inconsistency suggests that these theories are more relevant to diffusional controlled creep. The applicability will probably decrease with the increase of plasticity involvement.

Constrained diffusional growth

For a metallic polycrystalline material, it is natural for it to present an anisotropic microscopic behavior due to the different orientations of the grains. Thus, some sites are more vulnerable to cavitation than others. The difference in cavitation vulnerability will lead to a heterogeneous cavity distribution, so the growth behavior is different from the unconstrained cavity growth. The growth theory for heterogeneous cavity distribution is constrained diffusional cavity growth. Considering

a scenario with heterogeneous cavity nucleation, the growth of these cavities by diffusion will cause the areas not affected by the cavity growth to constrain the "growing area" as the continuity of geometry and stress equilibrium must be satisfied. The constrain around the cavity-affected zones could lead to redistribution of stress among the "cavity-free" areas. Thus the fracture could also be controlled by the plasticity in those areas [31]. The schematic comparison of homogeneous and heterogeneous cavitation is shown in Figure 2.6. The constrained cavity growth rate is derived in [47].

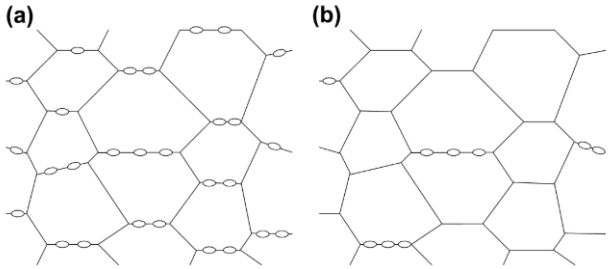

Figure 2.6: Homogeneous (a) and heterogeneous (b) cavitation at boundaries. The latter condition can particularly lead to constrained cavity growth. [31, 48]

Grain Boundary Sliding

While being unclear in cavity nucleation, grain boundary sliding has been considered a important aspect for cavity growth at the grain boundaries [31]. The sliding does not necessarily lead to significant volume change of the cavity, but it changes the cavity into a sharper geometry as shown in Figure 2.7. Because the tip sliding velocity is limited by surface diffusion, the third-power relation becomes reasonable in this situation [31].

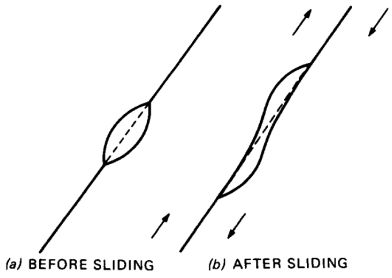

Figure 2.7: Schematic illustration of shapening a cavity by grain boundary sliding[48]

Plasticity Controlled Growth & Coupled diffusion and plastic growth

It is possible for a cavity to grow exclusively by plasticity under a high strain rate. Hancock [49] presented a model in which the cavity growth is irrelevant with vacancy flux. However, achieving a fully plasticity-controlled creep in most experiment cases is not realistic. A more reasonable model may actually be a coupled

diffusion and plastic growth. The GB diffusion only dominates the growth over a limited region around the cavity. The plasticity dominates the growth further away from the cavity, and interact with GB diffusion by controlling the diffusion length. A schematic illustration of the coupled growth is shown in Figure 2.8. The diffusion length is derived by Needleman and Rice as shown in equation 2.14.

$$\Lambda = \left(\frac{D_{gb}\Omega\delta\sigma}{kT\dot{\epsilon}}\right)^{1/3} \tag{2.14}$$

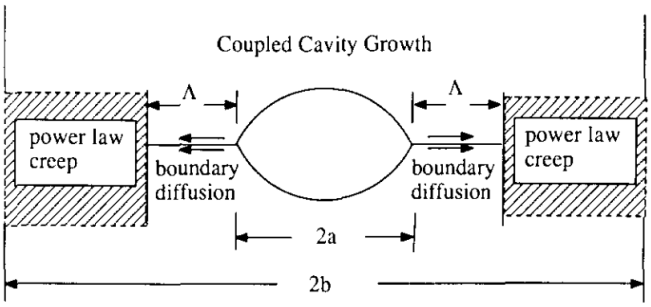

Figure 2.8: Schematic illustration of cavity growth by coupled diffusion and plasticity [50]

2.3. Creep-Resistant Strategies in Traditional Ferritic Creep-Resistant steels

Creep is one of the most significant challenges for steel to be used at elevated temperatures. The main drivers for developing long-life creep-resistant steels are the inconvenience and the costs involved in the frequent changing of the components in a thermal power plant (including coal-fired power plants and nuclear power plants). As a relatively cheap choice with decent properties, the development of ferritic creep-resistant steels drew great attention.

This section discusses the strengthening mechanisms used in traditional creep-resistant steels and gives a brief summary of the development of traditional creep-resistant steels.

2.3.1. Strengthening Mechanisms in Ferritic Creep-Resistant Steels

Traditionally designed creep-resistant steels under the guidance of the ”damage prevention” methodology mainly include four strengthening mechanisms: solid solution strengthening, precipitation strengthening, dislocation strengthening, and boundary/sub-boundary strengthening[9, 51]. Generally, these four mechanisms work collectively. The predominance of each mechanism usually depends on the condition, for example, temperature [14]. Besides, it is usually difficult to study the working of these mechanisms in an alloy separately.

Solid Solution Strengthening

Solid solution strengthening is the most direct and time-independent strengthening mechanism for alloys. The substitutional solute atoms, such as Mo and W, have a much bigger atomic radius than solvent iron atoms; they provide excellent impedance toward deformation. Although they also serve as essential constituents of some strengthening precipitates, as solid solutions alone, they provide a significant increase in creep-resistance properties. Maruyama et al. [52] compared the minimum creep rate between α iron (0.001wt.%C) and Fe-2.3wt.%W alloy. Neither of these two materials has precipitates or the subgrain structure with the free dislocations as strengthening effect. The result shows that with only solution strengthening in effect, the creep rate can be reduced by three orders of magnitude, as shown in Figure 2.9

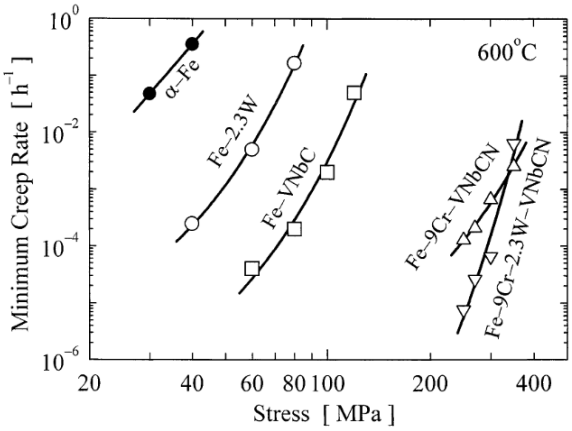

Figure 2.9: Minimum creep rates of ferritic steels at 600°C.[52]

Precipitation Strengthening

Precipitates usually form from the base alloy matrix during heat treatment. The passage of dislocation through a precipitate leads to the formation of a new dislocation. Finner dispersed precipitates can generate more dislocations during deformation. The precipitates also provide resistance to the dislocations. The resistance capability of the precipitates towards deformation is often characterized by the threshold stress needed for a dislocation to pass through precipitate particles. Several mechanisms are proposed to describe the threshold stress; one of the most widely known mechanisms is the Orowan mechanism. The Orowan stress can be calculated using the following equation [52],

$$\sigma_{or} = 0.8MGb/\lambda \tag{2.15}$$

in which M is the Taylor factor (= 3), G the shear modulus, b the magnitude of the Burgers vector, and λ is the mean inter-particle spacing, which can be derived from volume fraction [9]. The schematic drawing of a dislocation passing through a precipitate is shown in Figure 2.10.

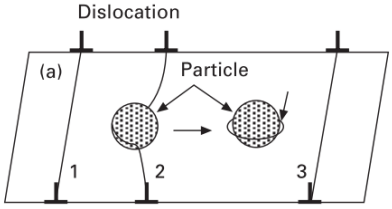

Figure 2.10: Schematic drawing of the Orowan mechanism [9]

Ferritic creep-resistant steel can include several kinds of carbides and carbonitrides within the matrix and grain boundaries, such as $M_{23}C_6$, M_6C, M_7C_3, MX, and M_2X, in which M denotes metallic elements, C the carbon atoms, and X the carbon and nitrogen. Intermetallic compounds like $Fe_2(Mo,W)$ Laves phase can also be found [51]. The critical feature in all these precipitates is the rate at which they coarsen (i.e., lose their strengthening contribution).

Dislocation Strengthening

Every dislocation is associated with a stress field around its core; when another dislocation moves through this stress field, it needs to overcome the force imposed by the stress field. This interaction is the origin of dislocation strengthening. The effectiveness of dislocation strengthening is demonstrated by Maruyama et al. [52] through comparing the minimum creep rate between bainitic (B) steel with the dislocation substructure and ferritic (F) steel without the dislocation substructure, as shown in Figure 2.11. With solid solution strengthening and precipitation strengthening also present, the dislocation substructure lowered the minimum creep rate to 1/70. The strengthening effect is also evident in Figure 2.9 by comparing the minimum creep rate between Fe–9Cr–VNbCN and Fe–VNbC, in which the former one has the dislocation substructure, and the latter one does not. The effect of dislocation strengthening is given in the following equation [52]:

$$\sigma_\rho = 0.5MGb(\rho_f)^{1/2} \tag{2.16}$$

in which ρ_f is the free dislocation density in the matrix.

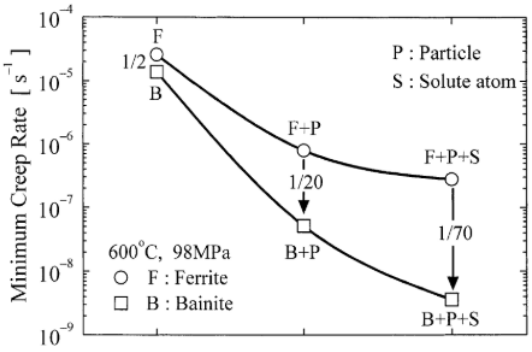

Figure 2.11: Minimum creep rates of ferritic (F) and bainitic (B) steels at 600°C and 98MPa. +P and +S mean that MX particles and solute atoms (0.6W+0.15Mo) were added to the steels.[52]

However, there are two limitations for dislocation strengthening:

- At elevated temperatures, the recovery of excessive dislocations and recrystallization of the deformed microstructure will erode the creep strength in long-term use.[9]

- It depends strongly on precipitation and solid solution strengthening since the dislocation substructures are not stable during creep without these obstacles. [52] As the precipitates coarsen during the creep and the pinning effect weakens, the dislocation strengthening effect would also vanish.

Boundary/sub-boundary Strengthening

Boundary/sub-boundary strengthening is technically a form of precipitation strengthening. It is specified because the boundaries (including grain boundaries and sub-boundaries hereafter) are relatively unstable under elevated temperatures, where creep cavities nucleate and grow. Creep cavities at the grain boundaries were found by scanning electron microscopy (SEM) [29] and transmission electron microscopy (TEM) [34] in the 1970s, as shown in Figure 2.12a and Figure 2.12b. A schematic structure of a tempered 9Cr to 12Cr martensitic steel provided by Abe [51] is shown in Figure 2.13. It consists of laths, blocks, and packets in a prior austenite grain (PAG). After appropriate normalizing and tempering heat treatment, the dislocation density within the laths is relatively high, the $M_{23}C_6$ precipitates are mainly distributed along the boundaries while the MX precipitates are mainly located in the matrix. The effect of sub-boundary strengthening due to the presence of laths and blocks can be calculated by

$$\sigma_{sg} = 10Gb/\lambda_{sg} \tag{2.17}$$

in which λ_{sg} is the short width of elongated sub-grains [52], and it is enhanced by a fine dispersion of precipitates along boundaries.

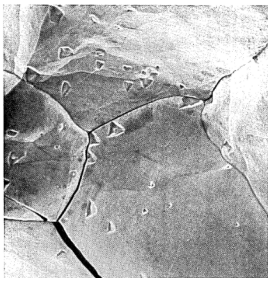

(a) SEM photo of the grain boundary cavities. [29]

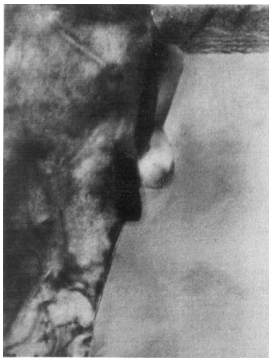

(b) TEM photo of a polyhedral shaped cavity associated with grain boundary particles. [34]

Figure 2.12: Cavities found by electron microscopy techniques

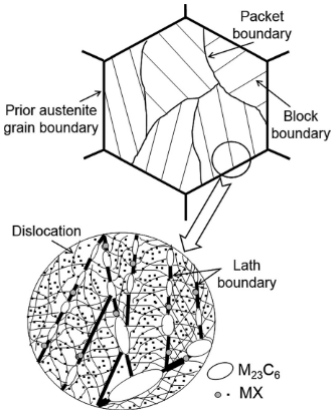

Figure 2.13: Schematic illustration of tempered martensitic microstructure [51]

As a result, the importance of reinforcing those boundaries became evident, and many studies were dedicated to optimizing the size, distribution, and composition of the boundary precipitates [53–55].

2.3.2. Compositional and Microstructural Effect in Ferritic Creep-resistant steels

Cr-containing (9wt.%-12wt.%) ferritic steels form a relatively mature and widely studied creep-resistant steel family among traditionally designed creep-resistant steels. Creep behavior and microstructural strengthening mechanisms are studied to a great extent. Some of the commercial creep-resistant steels like P91 and P92 also belong to this category [56].

In order to enhance the performance of the Cr-containing ferritic steels, many studies aimed at optimising the alloying elements. The development of the compositional optimisation of creep-resistant ferritic steels could be divided into four phases [6]. The first phase happened in the 1960s; the major improvement strategy was the addition of Mo, V, and Nb. The second phase happened between 1970-1985 when Oak Ridge National Laboratory optimized the content of C, V, and Nb and designed a commercially successful T/P91 creep-resistant steel grade.

The third phase happened between 1985-1995. Tungsten was found to be one of the potential components on delaying softening and hindering self-diffusion rates of iron, thus improving the stability of $M_{23}C_6$ precipitates [57]. Fine Fe_2W precipitates could impede creep in the transient creep region as well [58]. Furthermore, a meager amount of boron (B) (about 0.002wt.%) was found to help to delay the coarsening of $M_{23}C_6$ just like W, and keep fine sub-grains, concluded later by Maruyama et al. [52]. Based on the findings at that time, Nippon Steel Corporation carried out further development based on T/P91, the content of W and Mo was adjusted, and a tiny amount of boron (B) was added. Such modification increased creep strength by 25%. Later in 1994, the newly developed creep-resistant steel was registered into ASME standard as the P92 grade.

The fourth phase happened after 1995, the added components became more diverse, but the underlying aim of improving the performance of the boundary precipitates and maintaining long-term stability of the precipitates and sub-grains remained. Tantalum was found to have a significant strengthening effect on 9Cr steels with a constant 1.1wt.% of tungsten [59]. Later research revealed that creep rupture strength increases with the content of tungsten within 1-2wt.% and decreases with the content of tantalum within 0.06-0.14wt.% [60]. Furthermore, research was done on the effect of W and Co on creep deformation of fully annealed and precipitation strengthened 15Cr-3W ferritic steels [61]. The result showed that the combined effect of W and Co increases the creep-resistant performance significantly, and W surpasses Co in the effectiveness of promoting long-term creep regime. The research on the tantalum-tungsten and the cobalt-tungsten system became the basics of developing creep-resistant steels in Europe and Japan, respectively.

In some more recent researches, yttrium [62] and hafnium [63] were both found to have a positive effect on extending the creep lifetime. It is also fascinating to note that in some of the strengthened creep-resistant steels, samples showed an extensive tertiary creep regime due to a high creep damage tolerance factor [60, 64]. While in other samples, the extended lifetime was mainly due to the delayed onset of the tertiary regime. Chen et al. [62] found that yttrium containing

nano-particles formed during the creep test could compensate for the softening effect during creep, resulting in longer steady-state creep. Kobayashi and Hara [63] found that the conventional precipitation of Fe_2Hf could reduce the creep rate in the transient creep regime and interphase precipitation of Fe_2Hf showed a higher stability against coarsening. The combined effect delayed the tertiary creep. Furthermore, Cao et al. [65] investigated a high entropy alloy that showed dynamic recrystallization and precipitation, dislocation jogging, and tangling, which also extended the creep lifetime by delaying tertiary creep onset.

2.3.3. Creep-Resistant Properties and Relevant Microstructural Aspects

Precipitates

Current commercial creep-resistant steels are generally designed in 1970s-1990s, in response to the increasing steam temperature used in thermal power plants. A significant increase in creep lifetime was achieved by optimizing the precipitates. The Orowan stress of three most commonly used strengthening precipitates in ferritic creep-resistant steels, together with the sub-boundary strengthening effect calculated using $G = 64$ GPa, $b = 0.25$ mm, and $\lambda_{sg} = 0.3 - 0.5$ μm are listed in Table 2.1 [51]. Note that the calculated strengthening stress may differ from value of the actual resistance when deforming the material but serves as a relative comparison.

Particle	Volume fraction, V(%)	Diameter, d_p(nm)	Spacing, λ_p(nm)	Strengthening stress,σ(MPa)
$Fe_2(W,Mo)$	1.5	70	410	95
$M_{23}C_6$	2	50	260	150
MX	0.2	20	320	120
Sub-boundary	N/A	N/A	N/A	320-530

Table 2.1: Volume fraction, diameter, and spacing of each kind of precipitates in high Cr ferritic steel, together with Orowan stress estimated from the values of interparticle spacing, and sub-boundary strengthening effect[51]

All precipitates mentioned above were found to strengthen the material at elevated temperatures by pinning boundaries or blocking dislocations within the matrix. The $M_{23}C_6$ was the earliest precipitate that caught researchers' attention in the 1990s. $M_{23}C_6$ were mainly found to precipitate along PAG boundaries (PAGB) and micro-grain boundaries [58]. However, they only presented a reliable pinning effect at an early stage because $M_{23}C_6$ coarsened relatively fast owing to the solubility of Fe and Cr [54]. As mentioned in section 2.3.2, W maintains the stability of $M_{23}C_6$ by hindering the self-diffusion of Fe atoms, and the creep lifetime is prolonged [24, 66]. B presents a similar strengthening mechanism by stabilizing $M_{23}C_6$ and maintaining fine subgrains [52].

Unlike $M_{23}C_6$, MX was mainly found to precipitate within the martensitic matrix along dislocations. Several groups of stress-time to rupture data tested at 550°C

from NIMS datasheet [67–74] for different 9Cr to 12Cr ferritic creep-resistant steels are re-plotted in Figure 2.14 using a common stress and time scale. In Figure 2.14, the ferritic steels are marked by two different types of symbols. The data denoted by circles are the steels with V, the data points denoted by squares are the steels without V. It is clear from the graph that the ferritic steels with V surpass the ferritic steels without V in terms of creep rupture stress for long-life service.

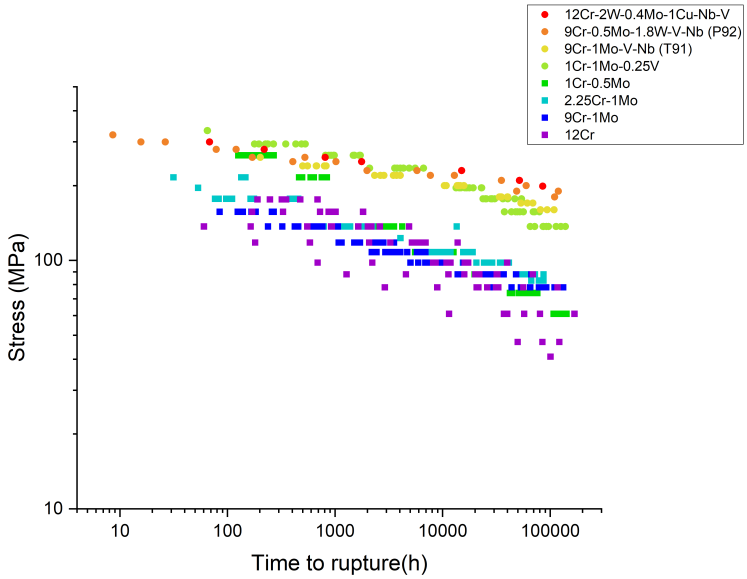

Figure 2.14: Stress-time to rupture for different 9-12Cr steels tested at 550°C [67–74]

One of the most widely accepted microstructural explanations for such superiority in creep lifetime is due to the addition of V or Nb, which promotes the precipitation of MX during tempering. The MX carbonitrides consist mainly of vanadium nitrides and a tiny amount of niobium carbides[51], Agamennone et al. [25] investigated the composition of the precipitates of the martensitic 9–12%Cr–2%W–5%Co steels, the mean atomic fractions of Si, V, Cr, Fe, W, and Nb are shown in Figure 2.15 also proved the constitution of MX.

While the tendency of precipitation gives $M_{23}C_6$ and MX different strengthening roles naturally, MX outperforms $M_{23}C_6$ in terms of precipitation strengthening, because of its fine size (typical size of MX is about 2 to 20 nm, while $M_{23}C_6$ is about 200 to 300 nm) and the uniform distribution. Many studies also pointed out that the long-term stability under the elevated temperatures of MX precipitates surpass $Fe_2(W, Mo)$ and $M_{23}C_6$ [25, 52, 55, 75, 76], due to the low solubility of V in the Fe matrix and the low driving force of the growth for MX. The comparison was made by Hald [76] and Maruyama [52] as shown in Figure 2.16 and Figure 2.17, respectively.

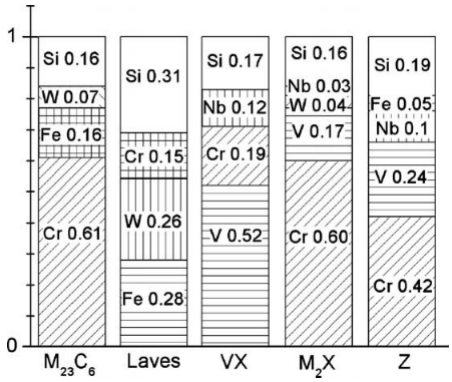

Figure 2.15: Mean atomic fractions of investigated elements Si, V, Cr, Fe, W, Nb in precipitates. [25]

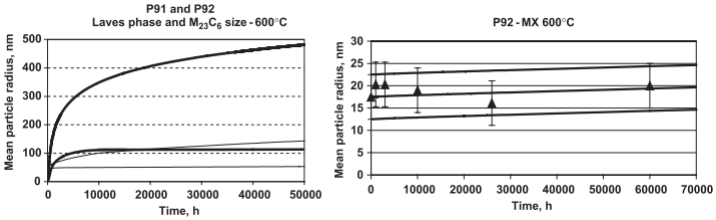

Figure 2.16: Left: Particle sizes of $M_{23}C_6$ (thin lines) and Laves phase (thick lines) in steels P91 and P92. Right: Size evolution of MX particles in steel P92. A similar MX evolution is observed in P91.[76]

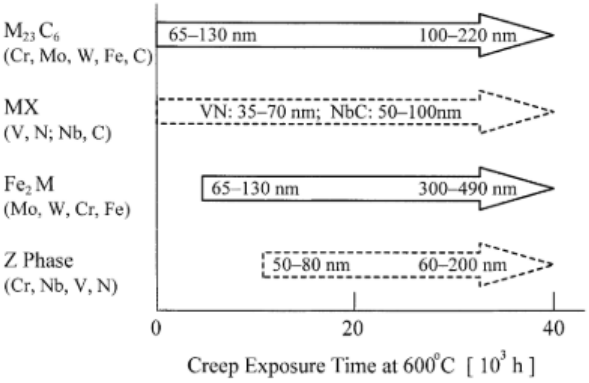

Figure 2.17: Precipitation sequence and particle diameter in 10Cr– 1W–1Mo–VNb steel.[52]

Based on the characteristics of the precipitates, Abe [55] proposed three precipitate design strategies:

- Reduce the unstable $M_{23}C_6$ through suppressing the C content, and only keep the finely dispersed MX as strengthening precipitates.

- Utilize B as a stabilizer for the $M_{23}C_6$ to further reduce their coarsening rate.

- Use a combination of nanosized MX and coarsening-resistant $M_{23}C_6$

Taneike et al. [53, 54] tried to alter the precipitation tendency of MX so that they could also contribute greatly to the boundary strengthening while eliminating big $M_{23}C_6$ precipitates along the boundaries. The strategy was to suppress carbon (C) concentration to 0.002wt.%. The time to rupture tested at 650°C and 140 MPa increased drastically compared to their base composition (9Cr-0.3Si-0.5Mn-3W-0.2V0.06Nb-3Co-0.05N-0.007B-C) when C concentration dropped below 0.05wt.%, as shown in Figure 2.18. Note that the base composition is taken from [54] because the composition shown in [53] has an obvious typo. Two TEM observations on the boundary precipitates from samples with different C concentrations clearly showed the variations, as shown in Figure 2.19.

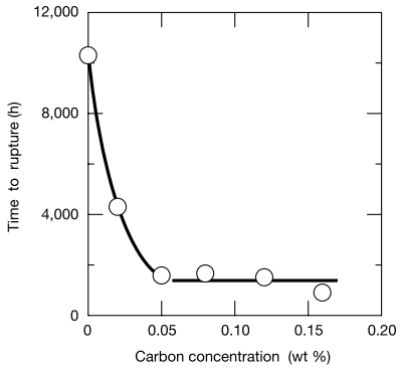

Figure 2.18: Time to rupture of the 9Cr steels at 923 K and 140 MPa, as a function of carbon concentration.[53]

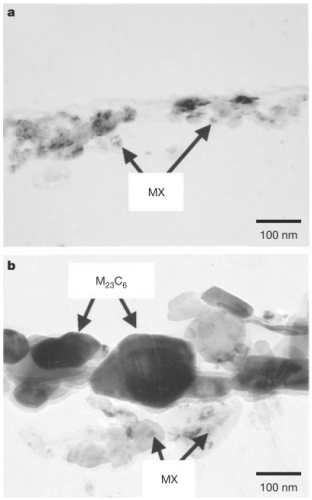

Figure 2.19: MX and $M_{23}C_6$ along grain boundaries in the specimens after heat treatment. a, 0.002% C steel and b, 0.078 % C steel. Both steels were normalized at 1,373 K for 0.5 h, cooled in air and then tempered at 1,073 K for 1 h. [53]

As a result, the prolonged lifetime was mainly attributed to the addition of V or Nb and the forming of fine MX during the tempering process, which delays the process of recrystallization. Abe [51] also concluded that the boundary and sub-boundary strengthening are the most crucial strengthening mechanism in creep-resistant steels and is enhanced by fine dispersion of precipitates along the boundaries, such as MX as mentioned above. It is worth to note that the most detrimental degradation related to MX is the formation of notorious Z-phase [23, 25, 76]. It is a complex nitride (Cr(V,Nb)N), and its composition is shown in Figure 2.15. It is evident from the graph that Z-phase is exceptionally rich in V. As mentioned before, V has low solubility in the iron matrix, so the growth of the Z-phase naturally consumes the V within MX, leaving a V-free zone. The depletion of V and precipitation of coarse Z-phase significantly reduce the overall pinning effect, making it easier for creep cavities to grow. Abe [51] concluded a few more microstructure degradation mechanisms in one of his reviews:

- Precipitation of thermally stable phases and dissolution of fine carbonitrides
- Preferential recovery of microstructure near PAGBs
- Combined coarsening of precipitates and laths
- Recovery of excess dislocations resulting from low-temperature tempering
- Static recovery
- Adverse effect of δ-ferrite
- Loss of creep ductility

Similar to the mechanisms of creep degradation, the improvement of creep performance is not a single factor problem as well. Nevertheless, the studies on the MX strengthening mechanism and optimization are of monumental significance, so they are introduced in great detail in this section.

Grain/Subgrain Size

For most 9-12Cr ferritic/martensitic creep-resistant steels, a complex but hierarchical microstructure is often observed; a schematic illustration is previously shown in Figure 2.13. In a prior austenite grain (PAG), several packets with parallel aligned blocks can be found. The orientation of the blocks between different packets can be different. The martensitic laths, also referred to as subgrains, are located within the blocks. The governing status of PAGs and inside packets of former martensite laths ultrafine subgrains to the strength of this material class [77] draws significant attention to finding and optimizing boundary-strengthening (including grain boundary and subgrain boundary hereafter) precipitates that maintain the desired microstructure. The grain/subgrain size, closely related to the boundary density, also plays a role in creep-resistance properties.

Nevertheless, creep is a process that is widely considered a diffusion-related process as introduced in previous section. Since the boundaries serve as "shortcuts" for atom diffusion [78], a low density of the boundaries is generally beneficial for creep-resistants properties. One of the extreme examples is the Nickel-based single-crystal superalloy [79] that is widely used on turbine blades in turbojet engines. It is not suitable for large creep-resistant structural components due to its high cost. Therefore, the change of grain/subgrain size of the polycrystalline ferritic steels during heat treatment and creep process and the effect of size change to creep-resistant properties are mainly discussed.

Heat treatment for 9-12Cr ferritic/martensitic creep-resistant steel generally includes austenitizing and subsequent tempering. Kim and Kim [80] studied the effect of austenitizing temperature on 12Cr steel. The as-received samples were austenitized at different temperatures for one hour and air-cooled. It was found that the PAG size increased with increased austenitizing temperature, as shown in Figure 2.20. A similar trend was also found by Chandravathi et al. in 9Cr–1.0W–0.06Ta RAFM steel [81], but with a small drop in PAG size around intercritical heating temperature (around 1125K), as shown in Figure 2.21.

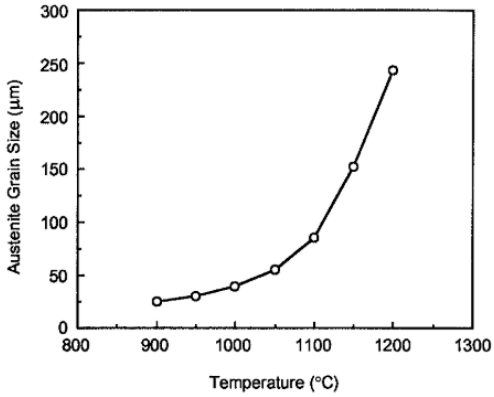

Figure 2.20: Effect of austenitizing temperature on PAG size [80]

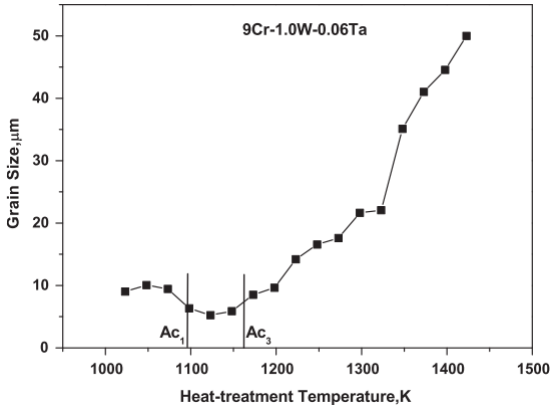

Figure 2.21: Variation of PAG size of 9Cr–1.0W–0.06Ta RAFM steel with heat treatment temperature in the as-quenched condition [81]

An exhaustive and quantitative study on PAG size and martensitic lath width during different heat phases (e.g., austenitizing, tempering, and creep) was conducted by Dronhofer et al. [82] using a 12Cr steel. The results are presented as probability nets (linearized Gauss distributions), the cumulative normalized frequencies are plotted against logarithmic microstructural sizes, as shown in Figure 2.22, Figure 2.23, and Figure 2.24. In Figure 2.22, statistical data of the PAG sizes from samples that underwent different austenitizing times are plotted. Differences in grain size are relatively small up to 4h of austenitizing time, but significantly bigger grain sizes are observed after 9h. However, the martensitic lath width is not sensitive to austenitizing time as shown in Figure 2.23, in which three samples were directly air-cooled after austenitizing. The effect of tempering and creep on subgrains are shown in Figure 2.24, the subgrains coarsened into bigger sizes as the

tempering time increased from 1h to 100h, and the subgrains further coarsened as they underwent the creep process.

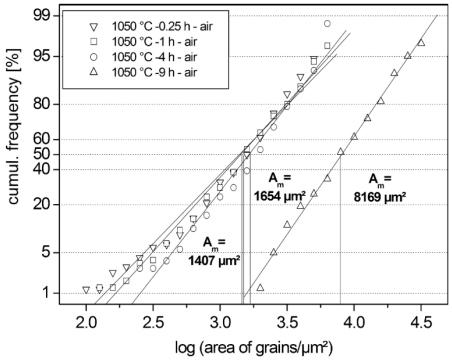

Figure 2.22: Probability net (numerically linearized error function) where the cumulative frequency of PAGs is plotted against the logarithm of the corresponding grain areas (x-axis) for increasing annealing times (T= 1050 °C, t = 0.25, 1, 4 and 9 h). Am-values (representing grain areas at a cumulative frequency of 50%) are given in the diagram. [82]

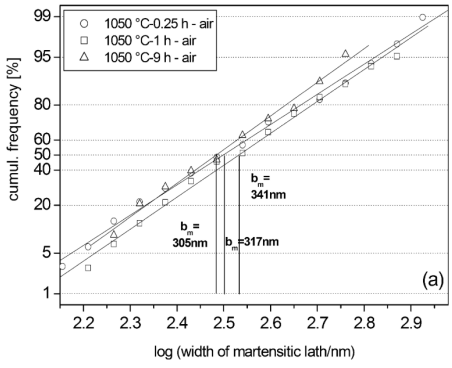

Figure 2.23: Probability net (numerically linearized error function) where the cumulative frequency of martensitic laths is plotted against the logarithm of the corresponding lath widths for increasing annealing times (T= 1050 °C; t = 0.25, 1 and 9 h; air cooling). [82]

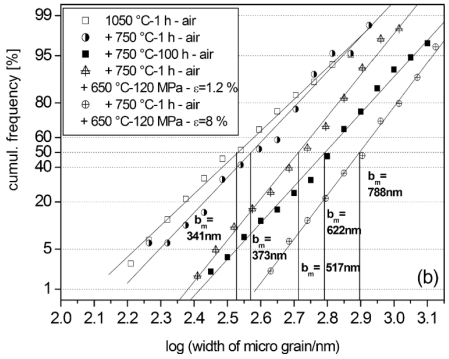

Figure 2.24: Probability net (numerically linearized error function) showing the influence of tempering time on the widths of micro grains (first: T= 1050 °C; t = 1 h; air cooling. then: tempering at 750 °C for 1 and 100 h and tempering for 1 hour followed by 650 °C creep at 120 MPa to 1.2 and 8% strain). Am-values (representing grain areas at a cumulative frequency of 50%) are given in the diagram. [82]

Similar coarsen of subgrains was also observed in a creep-fatigued ferritic 12Cr-2W steel by Hayakawa et al. [83]. The sample underwent creep-fatigue tests at 923K (650°C), trapezoidal waves with the peak value of 1.0% were applied, the sample was kept at peak strain for 10.8ks in each cycle, and the transition strain rate was $5 \times 10^{-4}/s$. The creep-fatigue life was 309 cycles. The block size and subgrain size were measured by field emission-type scanning electron microscope (FE-SEM) before and after creep-fatigue tests. The results were shown in size distribution histograms in Figure 2.25 and Figure 2.26 respectively. Comparing the size distribution of blocks and subgrains, it is not difficult to observe that subgrains coarsen much more than blocks. The average subgrain width changed from 0.45μm to 0.93μm, with about 106.7% coarsen ratio, while average block width changed from 1.58μm to 1.62μm, with only 2.5% coarsen ratio. With coarse subgrain near PAG boundaries, the local deformations were concentrated. The recovery near PAG boundaries also progressed faster than in other regions. Coarse subgrains were found to frequently form near PAG boundaries during the creep-fatigue tests, and they were likely to be implicated in grain boundary fractures. Non-uniform changes in the distribution of precipitates on the boundaries were also reported and suggested to be related to fractures that originate at grain boundaries. Note that such non-uniform distribution of precipitates along the subgrain boundaries was also observed and reported in [77]. It is interesting to note that in the study conducted by Wang et al. [84], fine MX failed to maintain the substructure of NS1 and NS2 samples during aging, they all recrystallized during aging and their tempered martensitic microstructures evolved into a ferritic microstructure with low dislocation density, while still presented superior creep-resistant properties in the creep tests. On the other hand, Wang et al. [84] also pointed out that NS1 normalized at 980°C (should have smaller PAG) had superior creep-resistant properties than CS normalized at 1050°C, while NS2 surpassed CNS even though they were both austenitized at 1210°C (should have similar PAG size). It indicated that the PAG sizes did not play a critical role in these tested alloys. It is possible to infer that

the coarsening of subgrains in Hayakawa's study does not necessarily lead to the degradation of the sample.

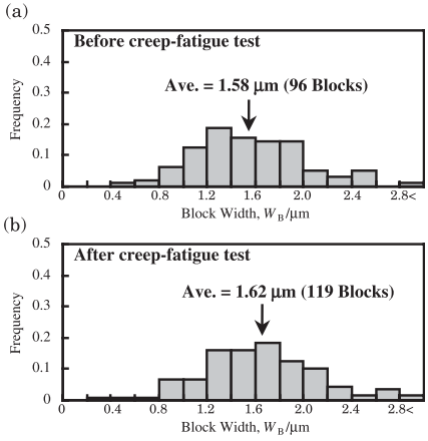

Figure 2.25: The frequency of the block size is shown as the function of width. Width were measured in several FE-scanning electron images before and after the creep-fatigue testing in (a) and (b), respectively. [83]

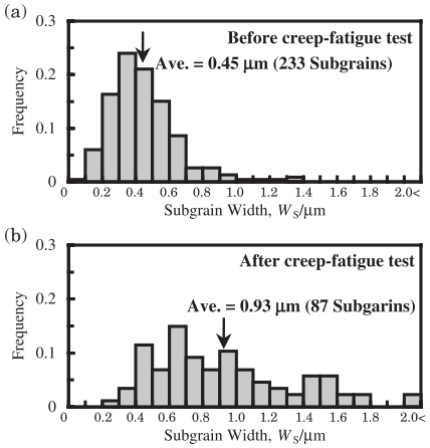

Figure 2.26: The frequency of the subgrain size is shown as the function of width. Width were measured in four transmission electron images before and after the creep-fatigue testing in (a) and (b), respectively. [83]

However, the grain does not always coarsen in the process of creep. Mulyana et al. [85] analyzed the microstructure of ferritic SA-213 T22 and austenitic SA-213 TP301H during interrupted creep tests in different percentages of the fracture time. It was found that the grain diameter decreased with the increase of damage level. As a result, the relation between creep properties and grain/subgrain sizes

during the creep process remains unclear; there could be other relevant coaction parameters that affect the creep properties.

Some studies are also dedicated to the effect of initial grain/subgrain size on creep-resistant properties. The creep property of ultrafine-grained (UFG) P92 steel was studied by Karl et al. [86] by performing creep tensile tests under 873K (600°C) with applied stress between 50 and 160MPa. The UFG microstructure was obtained by severe plastic deformation (SPD), such as high-pressure torsion (HPT) used in this study. The researchers concluded that the UFG P92 steel exhibits significantly faster minimum creep rates, and there was a decrease in the value of the stress exponent in comparison with coarse-grained P92 steel, though no specific coarse-grained P92 data was provided. Interestingly, the UFG P92 has a shift in stress exponent of the minimum creep rate, implying a shift in the deformation mechanism. The relation is shown in Figure 2.27.

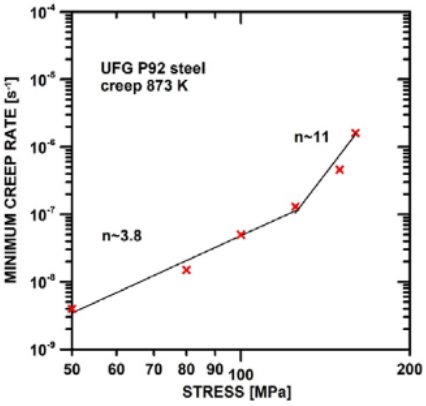

Figure 2.27: Stress dependence of the minimum creep rate measured for UFG P92 steel. [86]

Furthermore, another report on long-term creep behavior of welded joints of P91 steel by Abd El-Azim [87] suggested that the fine-grained heat-affected zone (FGHAZ) severely degraded the creep-resistant properties. The subgrain size of base metal (BM) and FGHAZ after post-weld heat treatment (PWHT) are listed in Table 2.2. The rupture strength is plotted against rupture time for both welded joint and base metal in Figure 2.28. The inferior creep-resistant property of the welded section is attributed to fine prior austenite grain size in FGHAZ as the recovery rate of dislocations and the coarsening rate of the subgrain are higher in this zone. However, in an oxide-dispersion-strengthened (ODS) ferritic steel studied by Hayashi et al. [88], ultra-fine initial grain size maintained stable after shortest annealing time and subsequent creep at 800°C. It is interesting to note that the longest creep lifetime was found in a sample annealed for a longer period with anomalous grain growth, the strengthening effect was attributed to Ti-rich nanoclusters in the anomalous coarse grains, and the creep-resistant performance is relatively insensitive to the grain size.

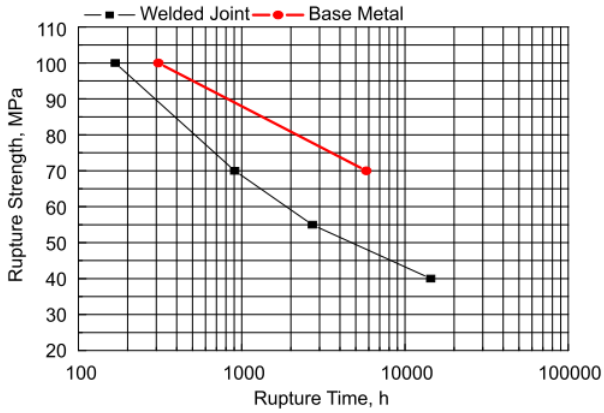

Figure 2.28: Creep rupture strength versus log rupture time plots of P91steel at 650°C. [87]

Condition	Subgrain size (μm)
BM of welded joint after PWHT	0.458
BM of welded joint after creep	0.597
FGHAZ after PWHT	0.718
FGHAZ after creep	1.230

Table 2.2: The Average subgrain size for P91 welded joint before and after creep at 650 °C/40 MPa. [87]

It can be concluded that the grain/subgrain size is relevant to creep-resistant properties, the specific effect strongly dependent on the constitution of alloy, precipitate types, heat treatment, and applied stresses. The desired grain size strongly depends on the application. For the applications in thermal power plants and nuclear facilities, the structures usually endure relatively low stress, while the required lifetime is usually quite long. Therefore, a longer austenitization time or higher austenitization temperature is needed to obtain a relatively larger grain size. However, the dynamic nature of creep and complexity of the alloy makes it difficult to relate the variation of grain size with the degradation of creep properties.

3

Development of Self-Healing Creep-Resistant Steels

The traditional ferritic/martensitic creep-resistant steels are more sensitive to pre-existed and creep-induced damage because there is almost no turning back once the damage happens. However, increasing the service life for current ferritic steels is still an attractive research field, and self-healing serves as an alternative strategy. Although the research is still preliminary, successful self-healing application in ferritic steels may lead to a breakthrough in this field.

This section includes a description of the early discovery of the self-healing phenomenon in creep-resistant steels, some general principles for designing self-healing creep-resistant steels, and the development of the theories and mechanisms based on model alloys.

3.1. Early Discovery of Self-Healing Phenomenon in Creep-Resistant Steels

In 2003, Kyono and Shinya [89] modified a 304 stainless steel by adding cerium (Ce), titanium (Ti), boron (B), and nitrogen (N). It was postulated that high-temperature stable boron nitride (BN) could form on the creep cavity surface and impede the growth of the cavity. The subsequent creep test confirmed the formation of BN on the cavity surface and was considered to suppress the growth of the cavities. The creep data also revealed an increase in creep rupture strength and creep rupture strain. Similar results were also observed in [90], a schematic graph showing the formation process of BN film is shown in Figure 3.1. Note that such healing is only possible when the precipitation of noxious sulfur (S) into the cavity surface is suppressed. Co-additions of Ce and Ti perform such suppression. The Shinya group also did the research on a modified 347 austenitic stainless steels [91, 92]. Film BN precipitates were found on the cavity surface, and a substantial improvement in the creep properties was reported.

3.2. Design Strategy

Though successfully implemented and even commercialized in numerous other engineering materials, the implementation of the self-healing strategy in steel has its difficulties. For structural materials, "local temporary mobility" suggests that the material maintains rigid when there is no damage; as the damage happens, the material at the damaged perimeter becomes mobile and shrinks or fills up the damage site. The criterion was proposed by van der Zwaag [10] as an essential consideration to realize self-healing. However, the rigid connection between atoms and the high melting point severely limits the realization of the required "local temporary mobility" criterion. The metal atoms are intrinsically small, thus unable to perform proper healing for damage that grows too big and requires a punctual design of self-healing mechanism [14]. The creep damage scenario provides an excellent application environment for self-healing steels [93]. The elevated temperature (usually $0.3T_m - 0.6T_m$) provides sufficient mobility for the healing agent.

Currently, the most developed self-healing strategy for creep-resistant steel is by bringing the healing agent into a supersaturated state so that the healing agent of

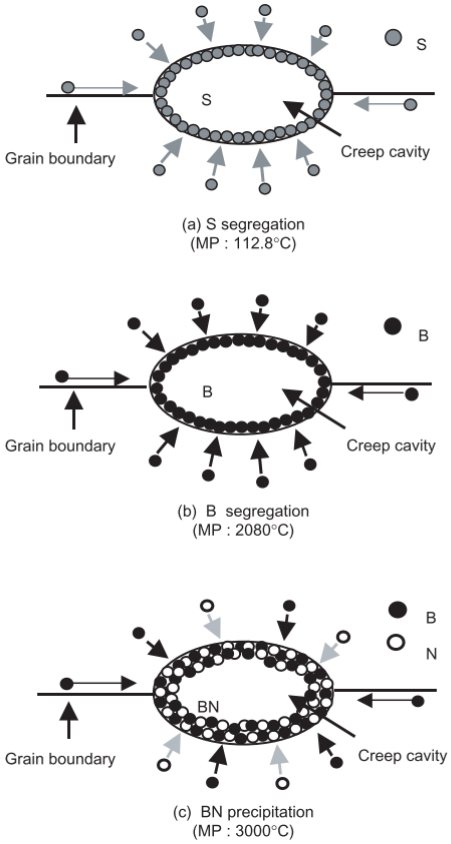

Figure 3.1: An illustration of S and B segregation and BN precipitation on creep cavity surface. [90]

the self-healing creep-resistant steels is stored as one or multiple alloying elements within the iron matrix. A few criteria for choosing the suitable alloying element to achieve successful self-healing was concluded by Van der Zwaag [94] in a review:

- The healing element can be brought into a supersaturated state with at least 1at.% excess level in the iron matrix.
- The healing atoms should have a larger atomic radius to ensure sufficient strain energy related to homogeneous precipitation so that the healing atoms will not precipitate randomly within the matrix.
- The healing atoms should have a faster diffusion rate than Fe atoms.
- The healing atoms should not interact with other atoms in their paths from the interior to the damage site.

Such a design implies that when a cavity is formed at the grain boundary during creep, a free surface is generated, and the energy barrier for nucleation of pre-

cipitates caused by the strain energy is reduced. The healing atoms will start to move towards the cavities and form precipitates to fill them. The combination of the thermodynamic driving force and energy barrier can drive the healing agents to the cavities while keeping the supersaturated solute atoms immobile and not consuming themselves by random precipitation when there is no damage. The careful control of the supersaturated percentage to get a good balance between the driving force and the energy barrier and sufficient high healing rate are vital in designing successful self-healing creep-resistant steels.

3.3. Model Alloys

Based on the design concept above, a few elements were chosen to set up multiple kinds of Fe-X binary systems dedicated to demonstrating self-healing behavior and revealing microstructural mechanisms. The chosen elements were copper (Cu), gold (Au), molybdnum (Mo) and tungsten (W). The early research on Cu with and without added B and N [95–98] showed that dislocations and free surfaces indeed accelerated the precipitation of supersaturated Cu. However, the precipitation did not show a strong preference for the free surface, thus leading to a significant amount of healing agents being wasted within the matrix and subsequently reducing the healing effect. The lack of selectivity was ascribed to the similar atomic radius of the precipitating Cu atom and the matrix Fe atom, which resulted in a limited strain energy for segregation of Cu-rich precipitates in the Fe-based matrix. Later research on the Fe-Au binary system [99–104] showed that Au indeed performs better than Cu in prolonging creep lifetime, as shown in Figure 3.2. Various microscopy techniques, includeing scanning electron microscopy

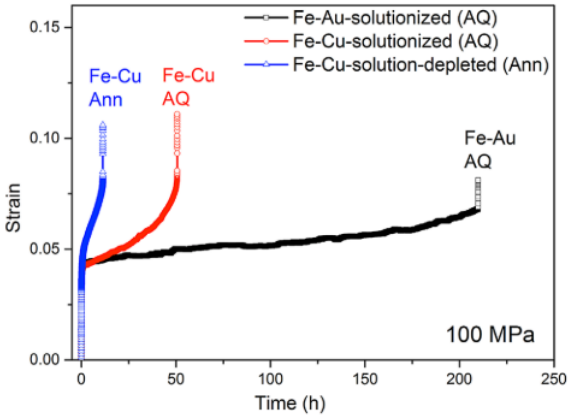

Figure 3.2: Comparison of the creep curves for the Fe–Au (solutionized) and Fe–Cu (solutionized and solution-depleted) alloys at an applied stress of 100 MPa and a temperature of 550 °C. The creep time has been compensated for variations in grain size. [99]

(SEM), transmit electron microscopy (TEM), electron probe microanalyzer (EPMA), electron backscatter diffraction (EBSD), synchrotron X-ray nano-tomography and

atom probe tomography (APT) were used to observe the samples. It was concluded that the supersaturated solute Au shows a strong tendency to precipitate on the surface of the creep cavities. Although some nano-sized gold precipitates can be found within the matrix, their contribution to the consumption of the Au atoms was negligible. A relatively significant difference in size between Au and Fe atoms ensured that considerable strain energy was involved in the heterogeneous nucleation, which helped to suppress random precipitate nucleation within the matrix. To achieve a more applicable self-healing creep-resistant design, Fe-Mo [105] and Fe-W [106] binary systems were studied. Due to the fact that nuclear application expects the reduction in Mo use [3], Fe-Mo binary system was not further studied by the Van der Zwaag group. Fe-W binary system was studied using synchrotron X-ray nano-tomography, which showed 3D images of the creep cavities and filling situation. The segregation of supersaturated W from the matrix and the precipitation of Fe_2W Laves phase in the creep cavities are the basis of self-healing in the Fe-W system. In this research, most isolated cavities were completely filled, while linked cavities were mostly partially filled, indicating a sufficient healing rate for isolated cavities until coalescence of the cavities. The self-healing potential of supersaturated W atoms in iron-based alloys provides new perspectives on the role of W for high-temperature creep-resistant steels. Subsequently, the study on the interplay between two separate healing agents was conducted by Fu. et al [107].

3.4. Design of the Novel Ferritic Creep-Resistat Steel

With previous studies on binary Fe-X and Fe-X-Y ternary systems, the W-rich Laves phase, was selected as a promising healing agent in the newly designed self-healing ferritic creep-resistant steel due to its decent healing rate and acceptable cost. The ferritic steel, which contains 9-12wt.% of chromium, was selected as the matrix to implement self-healing. To find optimal designs for multiple-component ferritic creep resistant steels with kinetically tuned self-healing behaviour, Yu et al. [14] proposed a computational model. The design of subsequently studied alloy was based on this computational model.

In this computational model, a generic algorithm is combined with a conventional alloy-design method to efficiently filtrate potential candidate alloys based on physical mechanisms. The design methodology follows that a requirement is first analyzed and translated into corresponding properties. In order to obtain these properties, the desired microstructure is then found and converted into quantifiable criteria. Finally, the criteria are associated with the composition and related heat treatment derived from physical metallurgy models.

The composition and homogenising temperature of the alloy candidates were generated via the genetic algorithm (GA). The alloys are designed to show a nearly fully ferritic matrix with a limited amount of primary carbides at the stage of annealing, decent corrosion-resistant properties, and desirable mechanical properties due to precipitation strengthening of $M_{23}C_6$ and solid solution strengthening of the alloying elements at the service temperature. The candidates should also be able to precipitate a sufficient healing phase during service to perform an effective cavity filling. The volume criterion of the healing agent was set based on the previous

experimental observation of cavity volume fraction in a Fe-W self-healing system [106]. The following go/no-go criteria were set in the algorithm:

- At homogenising temperature, the equilibrium volume fraction of ferrite should be larger than 99%.
- At homogenising temperature, the maximum level of primary carbides should be limited to 0.5% in vol.%
- At homogenising temperature, the maximum amount for all undesirable phases (which leads to early component failure excluding M23C6 carbide and Laves phase) should be no more than 1 vol.%
- At service temperature, a minimum chromium concentration of 8 wt. % should remain in solid solution in the matrix to yield adequate corrosion and oxidation resistance.
- At service temperature, the volume fraction of Laves phase at equilibrium should be higher than 1%

A relatively simple alloying system containing C, Cr, Mn, Si, and W was selected as alloying elements. The algorithm was set to generate and filtrate candidates within the range listed in Table 3.1, in which T_{homog} stands for homogenize temperature. At the beginning of the calculation, a random combination of composition and annealing temperature was generated, the thermodynamic equilibrium of this specific combination was then calculated at the annealing process and in the service stage. The result should fulfill the aforementioned go/no-go criteria. For the candidates that passed the go/no-go criteria, their solid solution strengthening factor (SSS) and precipitation hardening contribution (PH) were calculated and stored. The flow chart of this design strategy is shown in Figure 3.3, and the calculation method for strengthening factors can be found in [14]. A selection pool with different mechanical properties and healing potential is fully established up to this stage.

	C	Cr	Mn	Si	W	Fe	T_{homog}
Min.	0	8	0	0	0	Balance	800
Max.	0.1	20	5	5	3		1200

Table 3.1: Search range (in wt.%) for alloying elements and the homogenisation temperatures (in °C).[14]

In order to achieve timely and effective healing, the time of Laves phase precipitation and the time of creep cavities growing into a considerable size should correlate with each other. While the nucleation and growth of the cavity include complicated calculations, the Laves phase driving force was chosen as the decision parameter. Such simplification required linkage between the calculated driving force with the direct formation behavior of the Laves phase. The incubation time obtained from the experimental data of several commercial W-containing creep-resistant steels was chosen as the parameter describing the formation behavior in

this case. A relationship between the calculated thermodynamic driving force (DF) and the incubation time for Laves phase precipitation was established. A relatively linear relation was found between the logarithm incubation time and thermodynamic driving force at different temperatures, as shown in Figure 3.4.

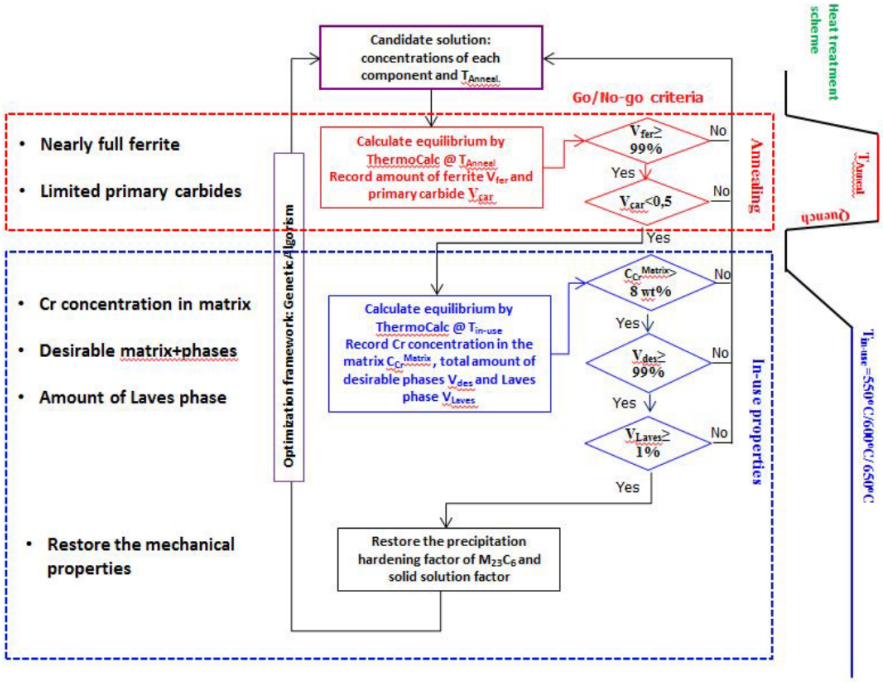

Figure 3.3: Alloy design strategy and criteria evaluation [108]

As a result, the strengthening factors of the candidate alloys were then linked with driving force (DF) at different service temperatures, which created a selection pool of self-healing creep-resistant steels with decent mechanical properties and different initiation times of self-healing. Two candidates with similar precipitation hardening factor at around 28 h and solid solution strengthening factor but with a varying driving force of Laves phase precipitation were selected under the use temperature of 550°C and subsequently studied. The compositions are listed in Table 3.2, in which FSHS stands for fast self-healing steel, SSHS stands for slow self-healing steel, and t_{init} stands for estimated healing initiation time at 550°C. The DF of Laves phase and corresponding incubation time of FSHS and SSHS are also marked in Figure 3.4. Both of these alloys were designed to homogenize at 1200°C.

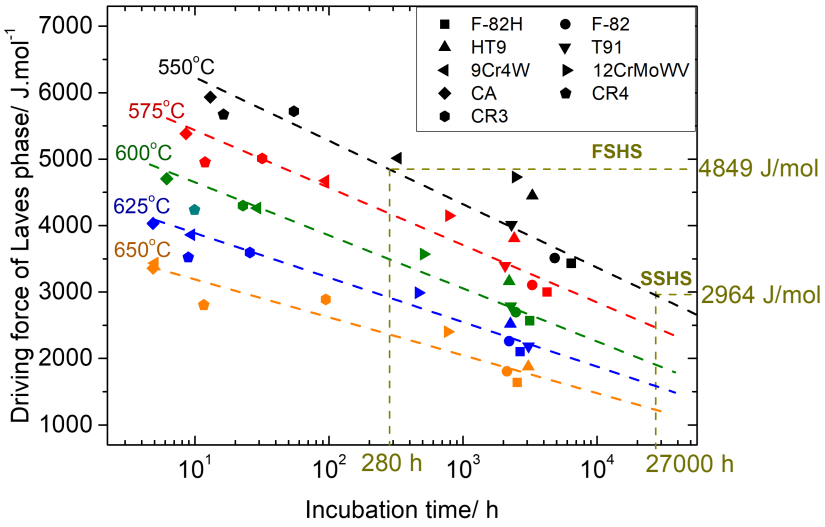

Figure 3.4: Experimentally observed incubation times for Laves phase precipitation against DF at several temperatures as reported for nine commercial steels, together with designed Laves phase DF and corresponding incubation time of FSHS and SSHS. [108]

	C	Cr	Mn	Si	W	Fe	DF of Laves $/J.mol^{-1}$	t_{init} $/h$
FSHS	0.023	13.03	0.01	0.97	3.0	Balance	4848.8	280
SSHS	0.026	12	0.81	0.32	1.45	Balance	2964.2	27000

Table 3.2: Designed compostion of the self-healing steels (in wt.%).[14]

4

Experimental

4.1. Sample preparation

4.1.1. Pre-treatment for as received sample

The samples were ingots with a thickness of 15mm as received. The ingots were firstly heat-treated at 1200°C for 5 hours before being hot-rolled into sheets of 5mm thickness. The finishing temperature of hot-rolling was around 800°C, and the hot-rolled sheets were water quenched. The thickness of samples was then reduced to 1.5mm by cold rolling and was further reduced to 0.5mm by milling. The dog-bone shaped samples with a gauge length of 12.5mm, a width of 6mm, and a thickness of 0.5mm (crosssection of 3 mm^2) were machined from the milled sheets with spark erosion. The shape and dimension of the creep samples are shown in Figure 4.1.

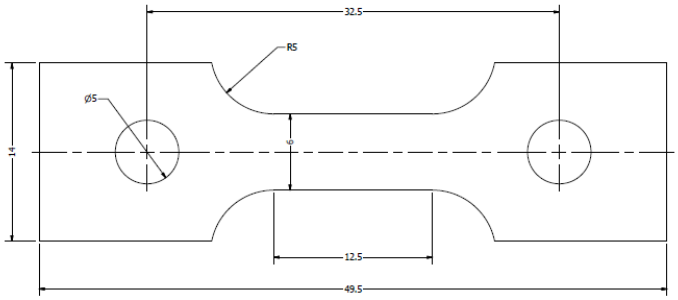

Figure 4.1: Shape and dimensions of the creep test sample[mm]

4.1.2. Heat treatment

The composition of the received samples have slightly different composition than the designed composition due to the manufacturing errors. The actual compositions are listed in Table 4.1.

	C	Cr	Mn	Si	W	Al	Fe
FSHS	0.022	12.6	0.023	0.807	2.23	0.019	Balance
SSHS	0.0226	12	0.806	0.181	1.14	0.046	Balance

Table 4.1: As received compostion of the self-healing steels (in wt.%).

To fully dissolve the tungsten atoms into bcc ferritic matrix and maintain super-saturation state at room temperature, samples need to be annealed and quenched before the creep test. Besides, the ideal microstructure after annealing should stay in the single-phase region while having a comparable grain size for both samples to minimize the grain size effect towards the creep tests. Furthermore, the grain size should be reasonably small for easier observation of the grain boundary phenomena. Some preliminary calculations and experiments were conducted to obtain the ideal annealing parameters. Calculations were made based on the measured composition of as-received samples using Thermo-Calc software TCFE9 Steels/Fe-Alloys

version 9.1. The equilibrium phase composition under different temperatures were plotted in Figure 4.2. The calculation showed two bcc regions for both FSHS and SSHS, as listed in Table 4.2.

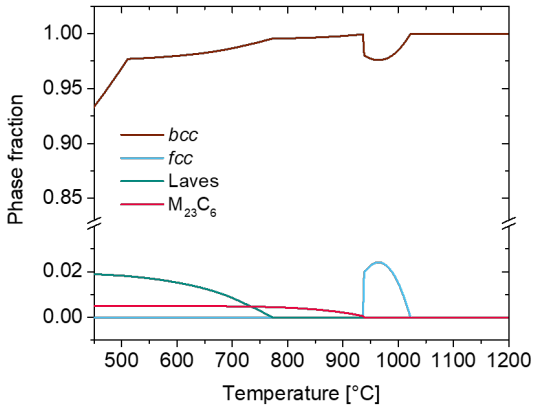

(a) FSHS

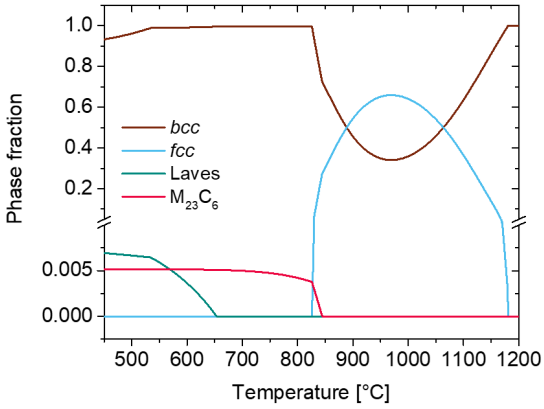

(b) SSHS

Figure 4.2: The amount of phases for two self-healing steels under different temperatures

	bcc region-1	bcc region-2
FSHS	770-920°C	Above 1030°C
SSHS	650-820°C	Above 1180°C

Table 4.2: As received compostion of the self-healing steels (in wt.%).

Heat treatment tests were conducted using different temperatures in two bcc regions with different annealing times. The heat treatment tests and subsequent heat treatment before creep tests were conducted using an electric high-temperature vertical tube furnace. During homogenising, the samples were sealed in quartz tubes filled with 200 mbar ultra-high purity argon to prevent oxidation. The samples which underwent different annealing statuses were water quenched to maintain the microstructure obtained at higher temperatures and subsequently observed by optical microscopy. Before the observation, samples were pre-treated by grinding, polishing, and etching in ferric chloride solution (0.08 g/mL FeCl3 in 8 vol.% HCl solution). The results, together with the heat treatment parameters are listed inTable 4.3. In which DP stands for dual phase region, and SP stands for single phase region, the number marked after DP or NP is the average grain size in micrometers.

	10min@780°C	30min@780°C	60min@780°C
FSHS	DP 14.8	DP 16.6	DP 20.0
SSHS	DP N/A	DP 21.7	DP 26.8
	1min@1100°C	1min@1150°C	1min@1200°C
FSHS	DP 36.3	SP 187.3	SP 256.0
SSHS	DP 15.0	DP 29.1	SP 243.2

Table 4.3: Heat treatment parameters and corresponding result.

The results showed that after annealing for 1 min at temperatures higher than 1200°C, a single phase can be obtained for both FSHS and SSHS. However, the grain size for both samples started to grow rapidly when the annealing temperature reached beyond this point. The grain size could typically reach $200\mu m$ after annealing for 1 min at 1200°C. Furthermore, all of the samples annealed at 780°C had undissolved $M_{23}C_6$ particles in the matrix.

In order to keep the growth of grain size under control and fully dissolve the $M_{23}C_6$ particles, annealing tests were conducted for FSHS and SSHS in bcc region-1 at 750°C and 810°C, respectively. The annealing time were set to 15 minutes, 4 hours, and 16 hours. The optical microscope photos of the samples are shown in Figure 4.3. The particle size and the grain size to annealing time are plotted in Figure 4.4. The growth of the grain size was relatively slow, the grain sizes were still below $30\mu m$ even after 16 hours of annealing. Moreover, the grains show an equiaxed structure after 30 minutes' annealing. However, some $M_{23}C_6$ particles remain undissolved in the matrix after 16 hours of annealing.

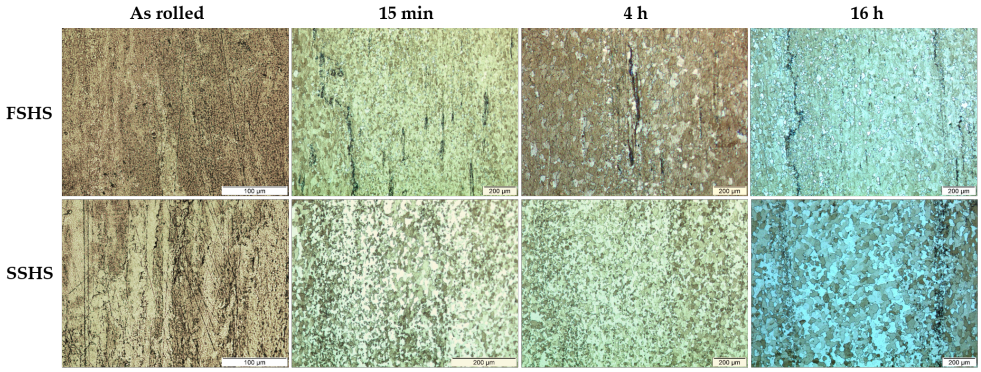

Figure 4.3: Optical microscope photos for FSHS and SSHS underwent different annealing time.

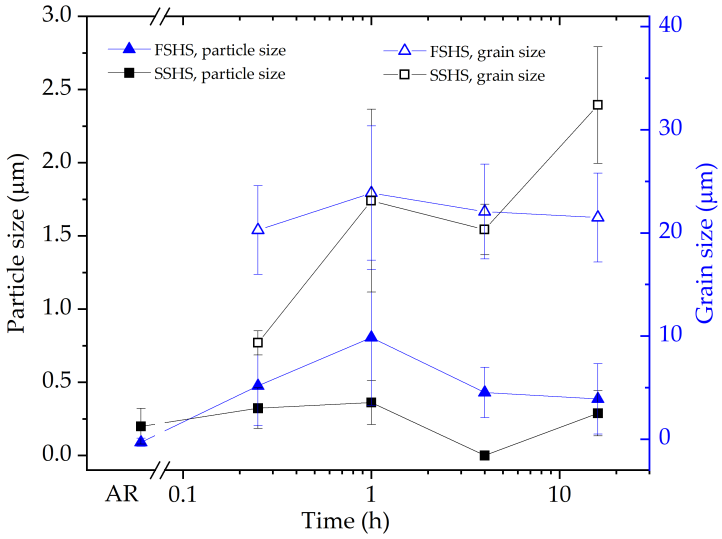

Figure 4.4: Undissolved $M_{23}C_6$ particle size and grain size with respect to annealing time.

Compromise is needed for a time and energy economical experiment. As a result, the annealing time was set to four hours and the temperatures for FSHS and SSHS was set to 810°C and 750°C, respectively. The average grain sizes of FSHS and SSHS are 20.3 μm and 22.1 μm, respectively.

4.2. Creep Tests

The creep tests were performed using a home-build creep tester which mainly consists of an Instron 5567 model loading frame, a computer, an upper connection structure with three thermocouple connection ports on it, a vacuum chamber with a heating component attached to the lower part of the chamber, a digital power supply of the heating component, a pre-stage pump, and a turbo-pump as shown in Figure 4.5. When mounting the sample, the upper connection structure, the upper

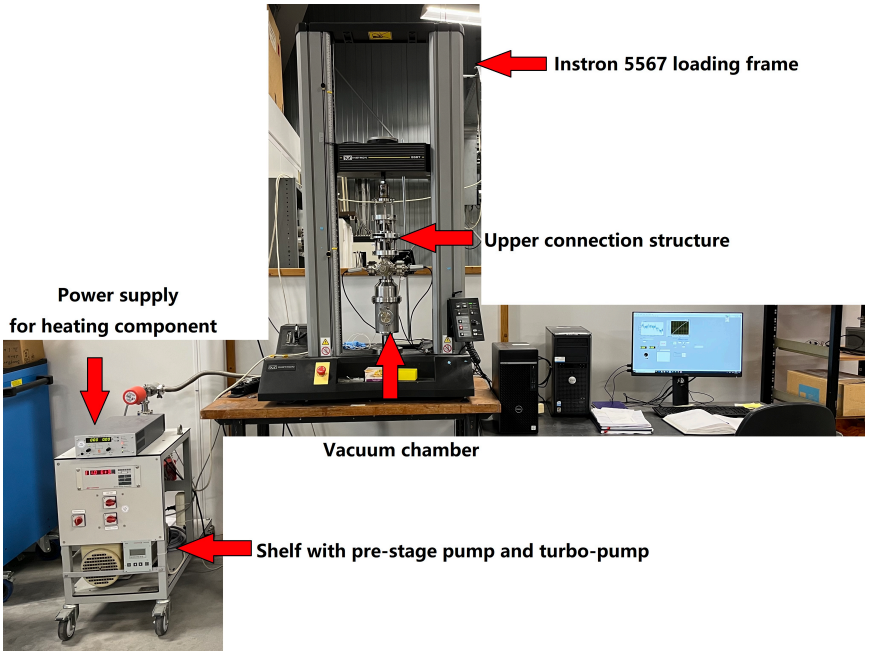

Figure 4.5: Experimental setup.

part of the vacuum chamber, and the lower part of the vacuum chamber can be disassembled from each other by following a sophisticated procedure. The samples are ground using sandpaper before being mounted to the upper sample clamping site located on the upper connection structure. Two thermocouples monitoring the temperature of the sample are spark welded onto the sample and one thermocouple monitoring the chamber temperature is free-hanged in the chamber. The whole testing setup can then be assembled following the reversed disassembling procedure.

A vacuum testing environment was needed to prevent the oxidation of the sample and obtain a clearer view of self-healing phenomena. After the sample is mounted properly, the pre-stage pump is started first to obtain a certain degree of vacuum ($< 1 \times 10^{-2}$mbar), the turbopump is then started to obtain a higher degree of vacuum. The vacuum can typically reach $< 4 \times 10^{-7}$mbar after 24 hours of pumping. A constant temperature and load can be applied to the sample when the

vacuum is ready. The temperature is controlled by a LabView program using PID control in this experimental setup. The temperature data used to control the heater comes from one of the thermocouples attached to the sample; the data source is selectable on the program interface in case one of the thermocouples stops working during the test. The load applied on the sample is controlled by Instron Bluehill, a bundled loading frame software. This software can select the desired load applied to the sample and other creep-related parameters. The load on the sample is calculated based on desired stress and gauge length cross-section and set prior to the test. The Instron Bluehill also records the load and displacement data periodically according to the preset interval.

Every creep test is performed in the same manner. After mounting the sample and getting the vacuum ready, find zero programs in the Instron Bluehill software is run to find the exact point that the sample is pulled straight but without any load. Then the tensile relaxation program is run to adapt the thermal expansion of the sample during heat up. A relatively low load (50N) is applied to the sample; then the heat up is started by setting the desired temperature to 550°C in the LabView interface. The heating procedure takes 90 minutes so that the heating and thermal expansion could reach a stable state. Finally, the creep program is run to conduct either creep deformed or failed tests.

4.3. Microstructure Observations

Scanning electron microscopy (SEM), energy dispersive X-ray (EDX) analysis, and transmitting electron microscopy (TEM) were used to examine the creep-failed samples. SEM observations were conducted on the rupture surface and polished surface. The rupture surface observation does not need pre-treatment, while the sample preparation for the polished surface is similar to the preparation for optical microscope observations mentioned before. Some samples are not etched for SEM observation to prevent etching from interfering with cavity observation. The equipment used in SEM observation was JEOL JSM-6500F Scanning Electron Microscope equipped with a field-emission electron gun. To identify the observed precipitates, EDX analysis was also conducted using the Oxford Instrument Ultim® Max 170 integrated with the scanning electron microscope.

TEM observation was conducted on the FSHS sample tested with a lifetime of 2487.2 hours by the Quantum Nanoscience department from the faculty of Applied Science. The elemental mapping in STEM mode was done using the Super-X in the ChemiSTEM™configuration. In scanning mode (STEM), annular dark field (ADF) images were collected. In this mode, a sub-nanometer beam is scanned on the electron transparent sample, and for each beam position, the diffracted electrons are collected on a ring shape detector. On heavy/thicker parts of the sample, more diffracted electrons are collected, showing bright in the image. EDX spectrum is also collected for each beam position in a STEM image to generate the elemental map. The sample was mechanically polished to about 20 μm thickness. Then, 2.3 mm discs were punched from the alloy at the neck of the plate and glued on a 3 mm (outer diameter) copper ring. The sample was Ar ion milled to electron transparency.

5

Results

5.1. Creep Data

The creep tests were conducted following the procedure mentioned in the previous chapter for FSHS samples and SSHS samples under different constant stresses. One of the fractured samples is shown in Figure 5.1. The strain (ϵ)-time (h) curves at 550 °C are shown in Figure 5.2. At all tested stresses, the creep deformation of FSHS and SSHS is characterized by a relatively short primary creep stage, a prolonged secondary creep stage, followed by a short tertiary creep stage. The transition between the stages is relatively fast. Most of the creep strain was accumulated during the tertiary stage, but the necking is not obvious from direct observation, possibly due to the relatively thin sample used in the test. The tilted fracture site indicate shear invlovement in the final fracture. The variation of creep rate ($\dot{\epsilon}$) with respect to time and strain are shown in double logarithmic plots in Figure 5.3 and Figure 5.4, respectively. The double logarithmic strain rate-time plot for FSHS and SSHS at all tested stresses shows a general drop in strain rate with time at an eraly stage of the creep and a rapid rise in strain rate by the end of creep lifetime. The double logarithmic strain rate-strain plots show a similar trend. The minimum creep rate ($\dot{\epsilon}_{min}$) is used to characterize the material behavior in the secondary creep stage.

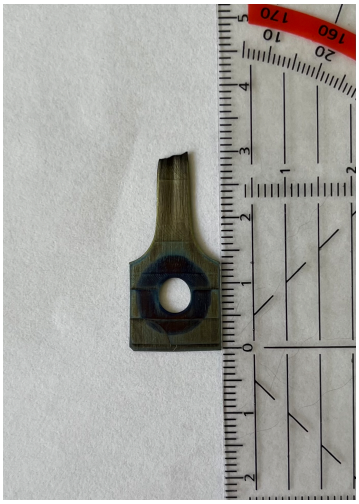

Figure 5.1: Creep failed SSHS sample tested under 140 MPa (Lifetime 33.6 h).

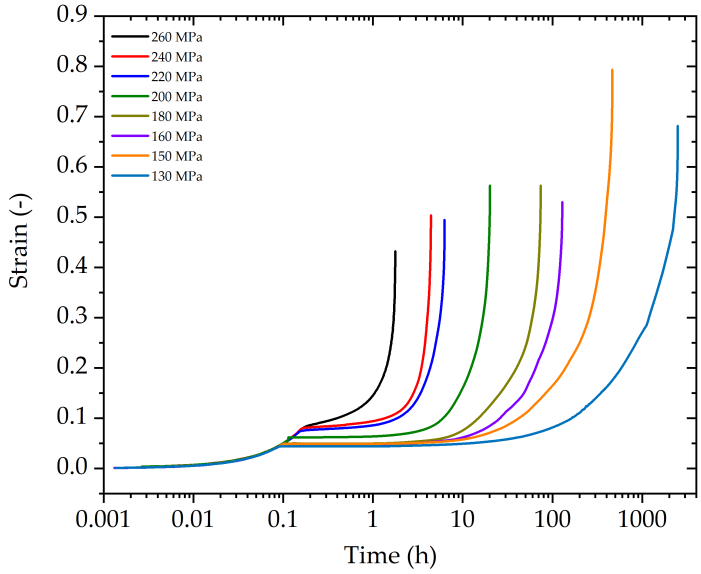

(a) FSHS

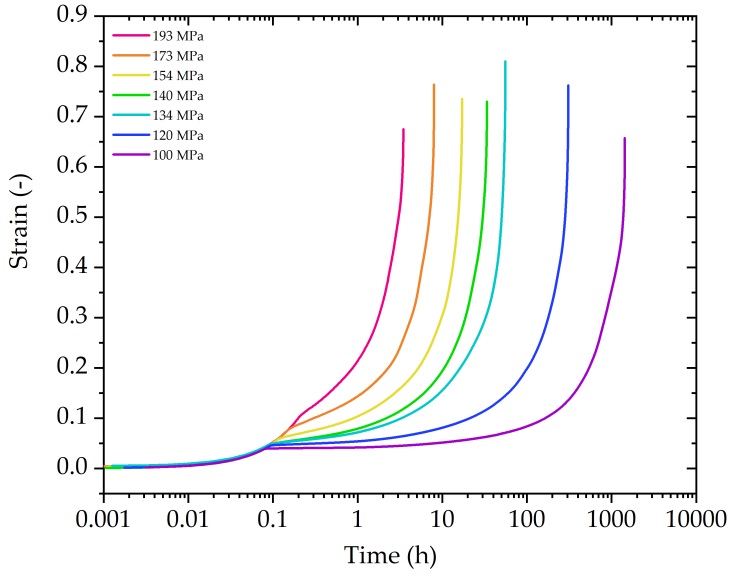

(b) SSHS

Figure 5.2: Strain-time curve for samples under different constant load.

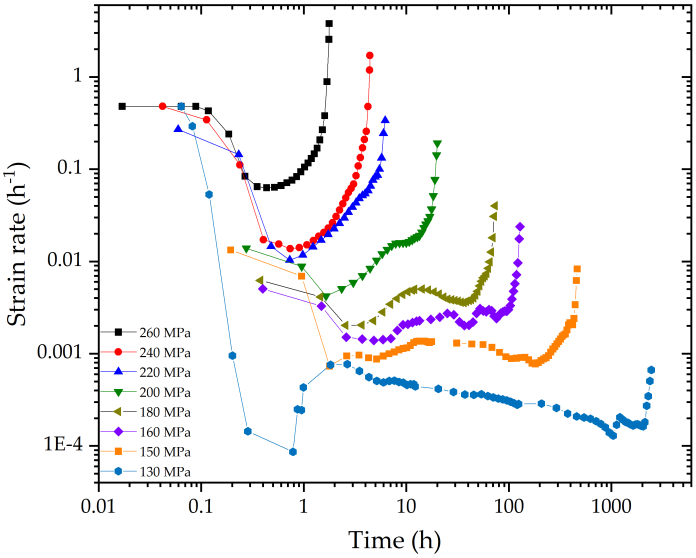

(a) FSHS

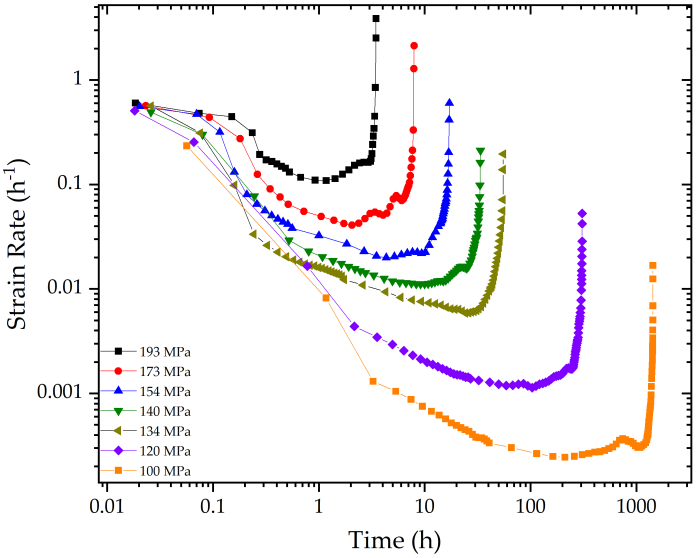

(b) SSHS

Figure 5.3: Strain rate-time curve for samples under different constant load.

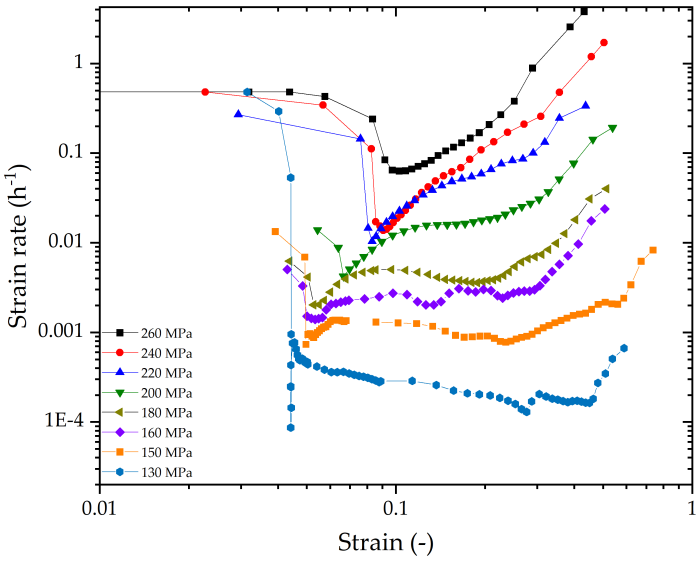

(a) FSHS

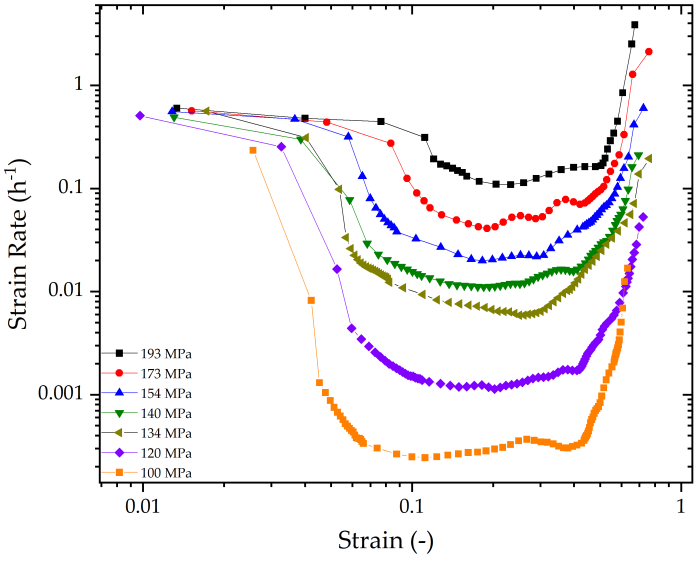

(b) SSHS

Figure 5.4: Strain rate-strain curve for samples under different constant load.

The minimum creep rate and lifetime is plotted against stress for FSHS and SSHS in double logarithmic scale, as shown in Figure 5.5 and Figure 5.6, respectively. The stress dependence of minimum creep rate obeys the Norton's power law for both FSHS and SSHS. As introduced in chapter two, the compact form of Norton's power law is $\dot{\epsilon}_{min} = A\sigma^{n}$. The stess dependence of lifetime also obeys power law as $t_R = A'\sigma^{-n'}$. The power law coefficients and stress exponents are given in the Table 5.1.

Alloy Type	$\dot{\epsilon}_{min} = A\sigma^{n}$		$t_R = A'\sigma^{-n'}$	
	A ($\mathrm{MPa^{-n}h^{-1}}$)	n	A' ($\mathrm{MPa^{n}h}$)	n'
FSHS	$10^{-20\pm1}$	7.8 ± 0.6	$10^{25\pm1}$	10.2 ± 0.5
SSHS	$10^{-22\pm1}$	9.4 ± 0.6	$10^{22\pm1}$	9.4 ± 0.6

Table 5.1: Values of power law coefficients and stress exponents for the stress dependence of minimum creep rate and lifetime for FSHS and SSHS.

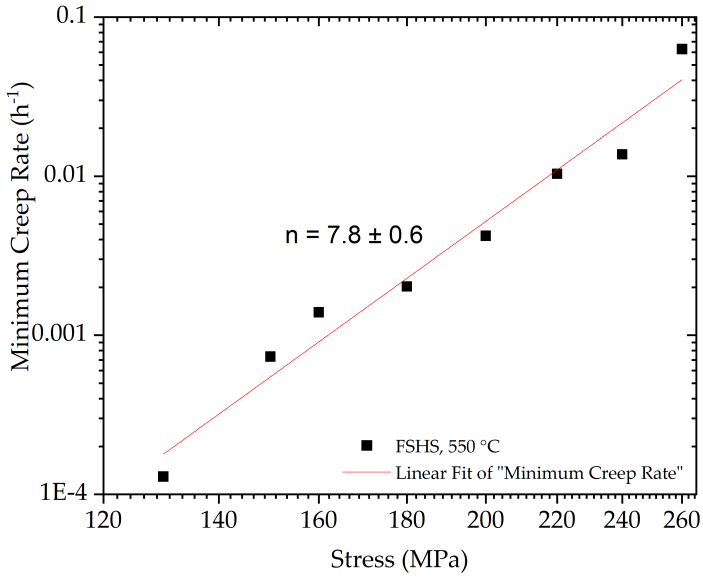

(a) Stress dependence of minimum creep rate.

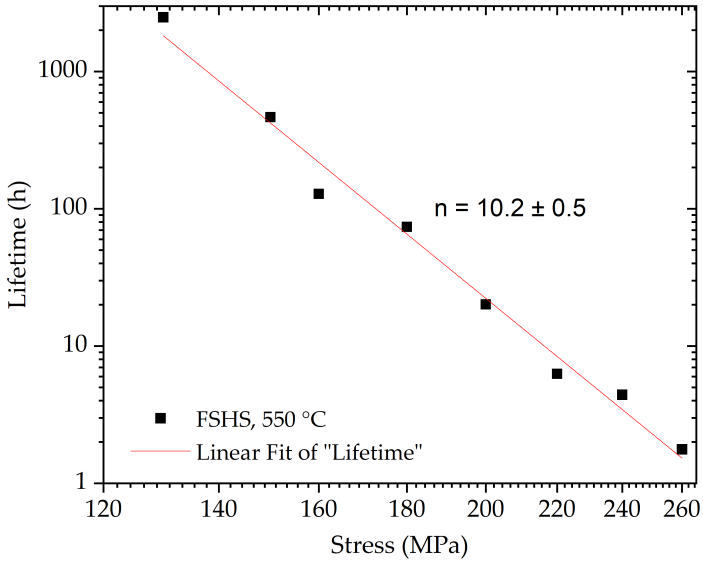

(b) Stress dependence of lifetime.

Figure 5.5: Stress dependence of minimum creep rate and lifetime for FSHS.

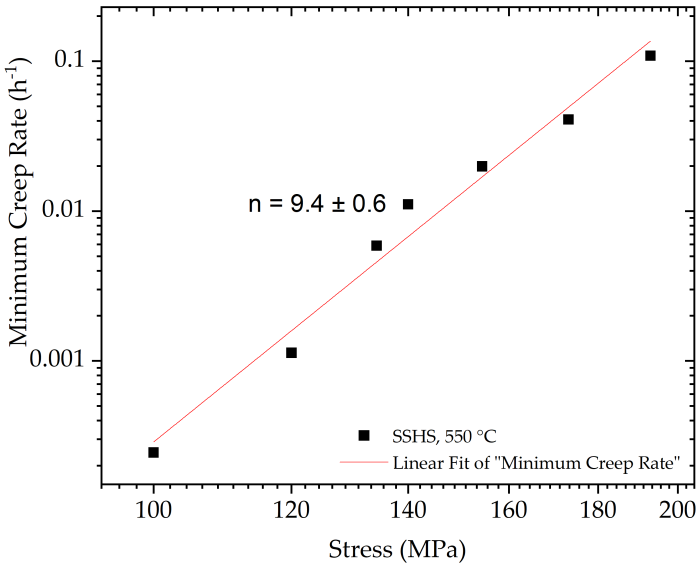

(a) Stress dependence of minimum creep rate.

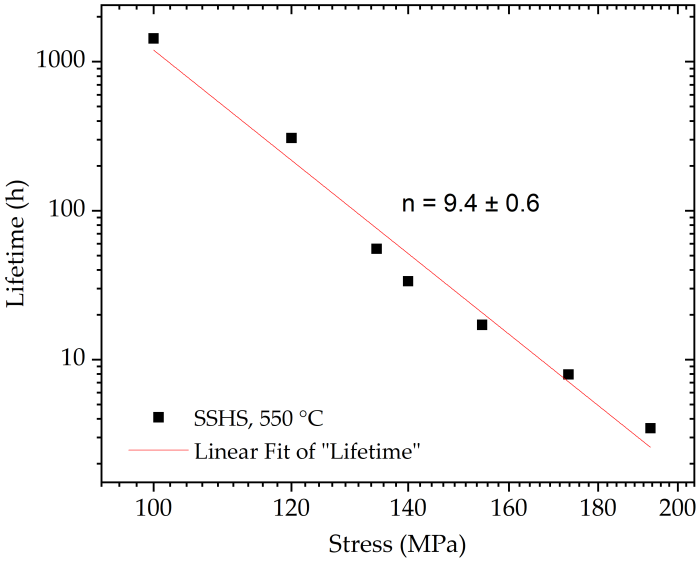

(b) Stress dependence of lifetime.

Figure 5.6: Stress dependence of minimum creep rate and lifetime for SSHS.

5.2. Microstructure of Creep Failed Samples

5.2.1. Fracture Surface

The genaral fracture surface features of the creep failed SSHS and FSHS samples are similar to each other, independent of lifetime. The backscattered electron (BSE) image of fracture surface taken from the FSHS sample with longer lifetime (130 MPa, 2487.2 h) and shorter lifetime (180 MPa, 73.9 h) are shown in Figure 5.7 and Figure 5.8, respectively. Besides, the BSE image of fracture surface taken from SSHS sample with longer lifetime (100 MPa, 1433.3 h) and shorther lifetime (140MPa, 33.6 h) are shown in Figure 5.9 and Figure 5.10, respectively , respectively. The fracture mechanism is studied based on SEM observation of these samples.

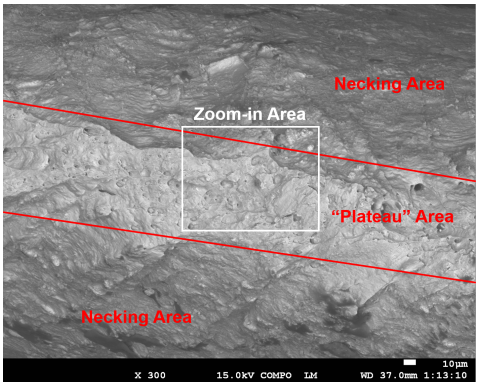

(a) Low magnification.

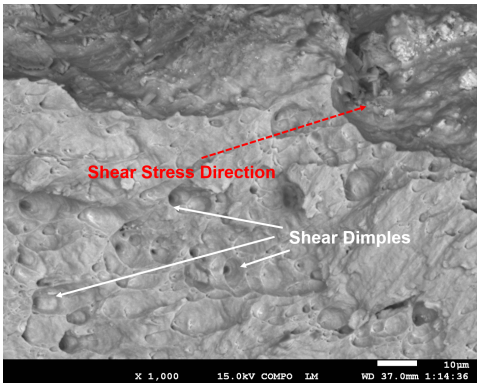

(b) High magnification.

Figure 5.7: Fracture surface of FSHS tested under 130 MPa (Lifetime 2487.2 h).

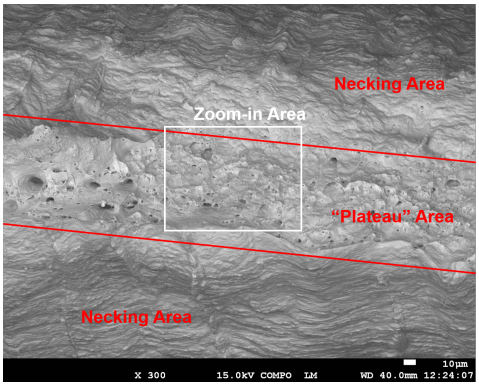

(a) Low magnification.

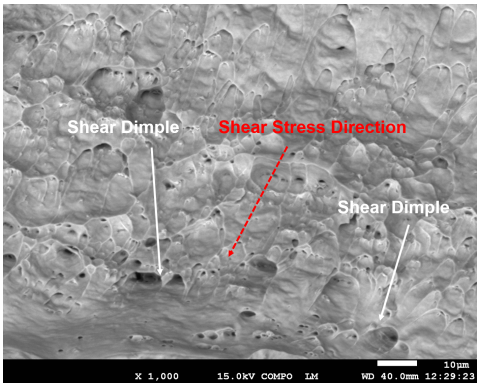

(b) High magnification.

Figure 5.8: Fracture surface of FSHS tested under 180 MPa (Lifetime 73.9 h).

All the SEM figures show that the fracture surfaces show a "tip" like feature, where the feature consists of steep necking areas on two sides and a small "plateau"

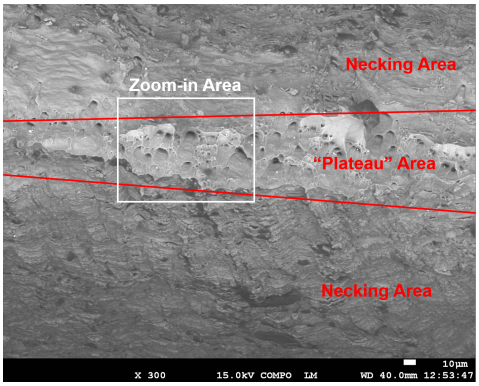

(a) Low magnification.

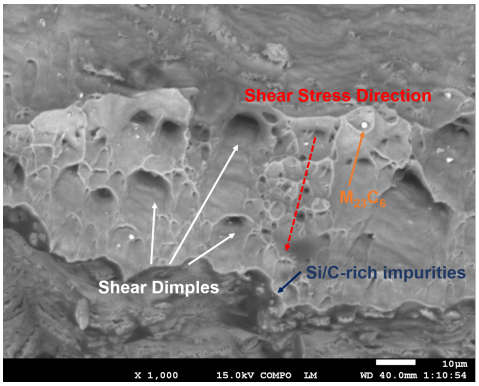

(b) High magnification.

Figure 5.9: Fracture surface of SSHS tested under 100 MPa (Lifetime 1433.3 h)

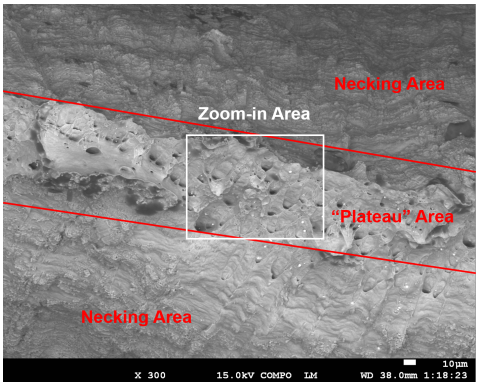

(a) Low magnification.

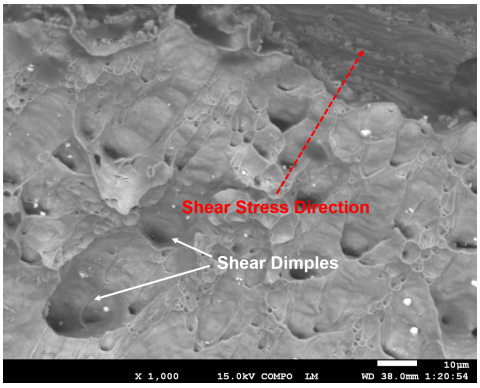

(b) High magnification.

Figure 5.10: Fracture surface of SSHS tested under 140 MPa (Lifetime 33.6 h).

in the middle with dimples on it. The necking areas are relatively large compared to the "plateau" area, indicating significant strain before fracture and a ductile fracture mode. In the zoom-in views, dimples with a parabolic outline are known as shear dimples caused by shear stresses [109], which indicates extensive shear involved in the creep fracture. The relatively large dark precipitates are silicon-rich or carbon-rich impurities, marked by a blue arrow in Figure 5.9b. The bright spots are chromium-rich $M_{23}C_6$ precipitates, marked by an orange arrow in the same graph. The precipitates mentioned above will be further discussed later.

The short-term creep fracture surface of a 9Cr tempered martensite ferric steel is observed by Xiao [110] et al. The fracture surface of a rod-shaped sample tested at 625 °C under 220 MPa is shown in Figure 5.11, which was identified as a typical ductile fracture. Comparing the fracture surface of the 9Cr steel with SSHS and FSHS, there are some similar features, such as distinct necking areas and shear

dimples, confirming the ductile fracture behavior of SSHS and FSHS. The ”plateau” area on the fracture surface of SSHS and FSHS is mainly occupied by shear dimples, showing similar characteristics to the radiation zone or shear-lip zone on the 9Cr steel, which correspond to the previous judgment on extensive shear involvement in creep fracture. However, the fiber zone with equiaxed dimples is almost absent in the SSHS and FSHS samples, possibly due to different specimen geometry. Besides, fractures surface showing dimple/foam like feature could also indicate transgranular fracture [22], as shown in Figure 5.12.

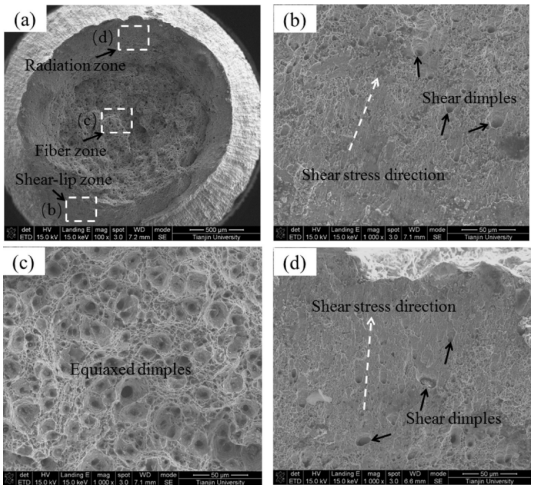

Figure 5.11: SEM fracture surface images of the ruptured specimen at 625 °C under 220 MPa: (a) macro view exhibiting elliptical necking, (b) magnified image showing shear dimples characteristic on the shear-lip zone, (c) magnified view of the fiber zone showing equiaxed dimples, and (d) magnified view of the radiation zone [110].

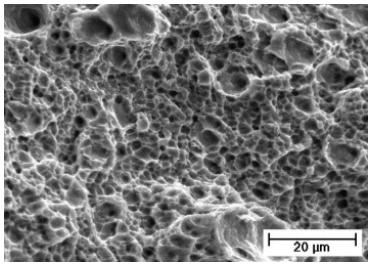

Figure 5.12: SEM fractograph showing transgranular fracture in specimen creep tested at 550 °C/200 MPa for 8098 h [22].

The comparison suggests that a ductile and transgranular fracture is the dominant fracture mechanism for the self-healing ferritic steel under the the tested conditions.

5.2.2. Stress-Affected Region

FSHS

The overview BSE images of FSHS were taken at the polished stress-affected region as shown in Figure 5.13. The tensile direction is marked in Figure 5.13a using a black arrow. The image of the as-quenched FSHS sample is also provided as a reference. In the overviews of FSHS, $M_{23}C_6$ precipitates can be observed in all samples, irrespective of the lifetime. Note that some $M_{23}C_6$ precipitates are found undissolved during sample pre-treatment and correspond with the phase fraction diagram shown in the previous chapter. The $M_{23}C_6$ in FSHS show a band-like distribution. Some dark spots are also observed in all samples and will be discussed later in this chapter. As mentioned previously, FSHS is expected to show self-healing behavior after approximately 280 hours in service. Zoom-in investigations are conducted on FSHS to find the W-rich Laves phase, which is the most crucial kind of precipitate as it is designed to be the healing agent in the newly designed self-healing ferritic steels. The zoom-in BSE images of the stress-affected regions taken from FSHS are shown in Figure 5.14. In the FSHS sample with a lifetime of 465.3 hours (Figure 5.14b) and 2487.2 hours (Figure 5.14c), another kind of bright and starry-like precipitates, different from $M_{23}C_6$, are found and could possibly be W-rich Laves phase.

To confirm the composition of the starry-like precipitates found in SEM observations. A detailed investigation was conducted on the FSHS sample with a lifetime of 2487.2 hours using TEM. The images of the electron transparent area are shown in Figure 5.15. Initial investigated area (a) shows the same orientation everywhere within 10-20° around the [111] surface normal. Only low angle boundaries are seen, decorated with precipitates, and no cavities are found at these boundaries. The precipitates in the matrix are almost more or less aligned in the same direction, and dislocation lines can be seen between the precipitates as marked in Figure 5.15a. EDX elemental maps show the same composition in low-angle grain boundary precipitates and matrix precipitates. A TEM image showing low angle grain boundary precipitates and matrix precipitates, together with relevant elemental maps in the corresponding area, is shown in Figure 5.16. A matrix precipitate with its relevant elemental maps is shown in Figure 5.17. The detailed composition of the precipitate and matrix measured by EDX in atom percent and the equilibrium composition of the W-rich Laves phase and matrix of FSHS calculated by Thermo-Calc software TCFE9 Steels/Fe-Alloys version 9.1 are listed in Table 5.2. These precipitates are identified as W-rich Laves phase precipitates because they are indeed richer in tungsten than the matrix. A $M_{23}C_6$ precipitate with its relevant elemental maps are also shown in Figure 5.18, and the measured composition (in at. %) is listed in Table 5.3. Note the scale bar shown below; the $M_{23}C_6$ precipitates are much larger compared to W-rich Laves phase precipitates.

The presence of Laves phase precipitates is confirmed in the FSHS with a lifetime of 465.3 hours (Figure 5.14b) and 2487.2 hours (Figure 5.14c). Comparing two FSHS images tested under different stresses shows that the Laves phase precipitates are denser and larger in the sample with a longer lifetime (2487.2 h) than in the sample with a shorter lifetime (465.3 h). The sheer difference in size be-

tween $M_{23}C_6$ precipitates and W-rich Laves phase precipitates, as shown in TEM observations, could help differentiate them effectively in other SEM observations.

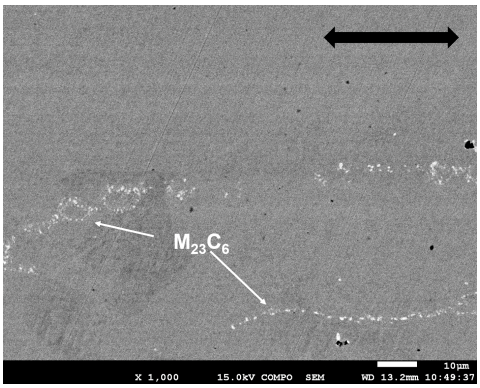

(a) Tested under 180 MPa (Lifetime 73.9 h).

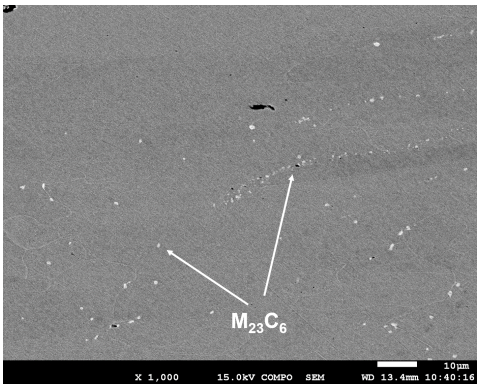

(b) Tested under 150 MPa (Lifetime 465.3 h).

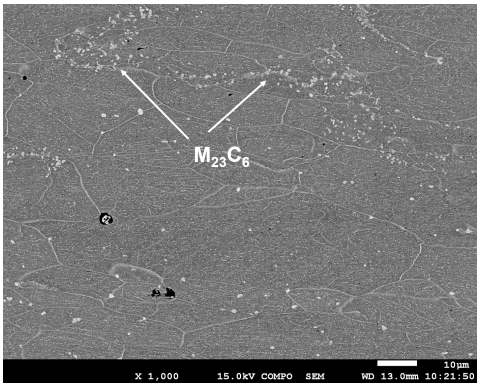

(c) Tested under 130 MPa (Lifetime 2487.2 h).

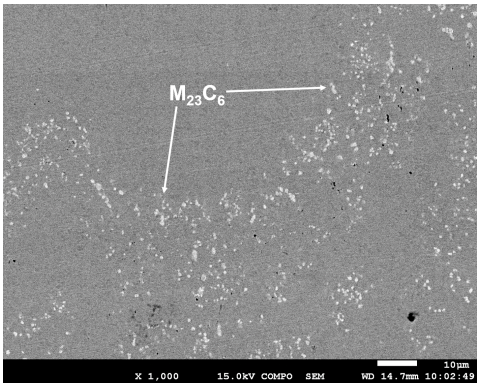

(d) As-quenched

Figure 5.13: BSE image of stress-affected region taken from FSHS creep-failed samples and as-quenched sample.

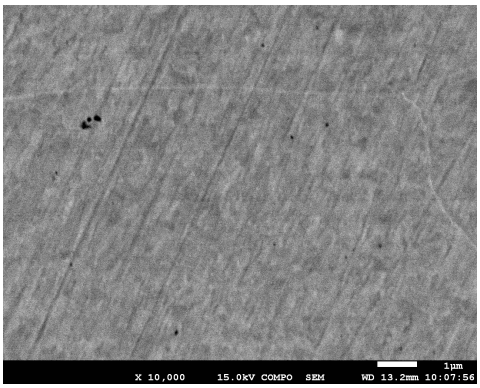

(a) Tested under 180 MPa (Lifetime 73.9 h).

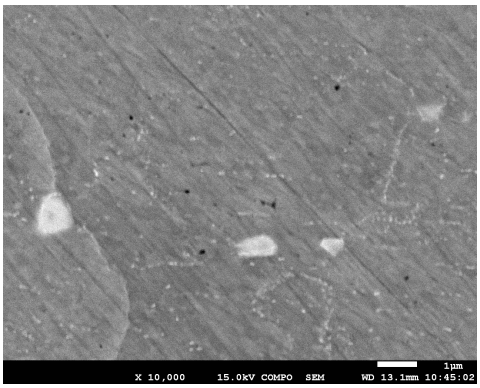

(b) Tested under 150 MPa (Lifetime 465.3 h).

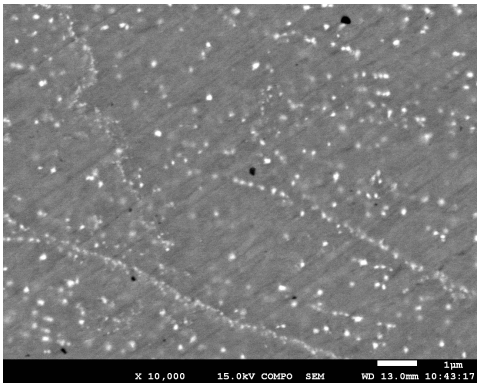

(c) Tested under 130 MPa (Lifetime 2487.2 h).

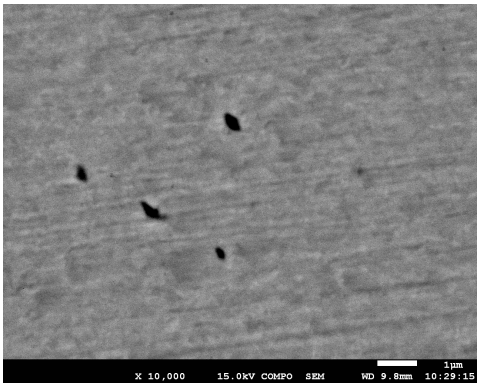

(d) As-quenched.

Figure 5.14: BSE image of stress-affected region taken from FSHS creep-failed samples and as-quenched sample with higher magnification.

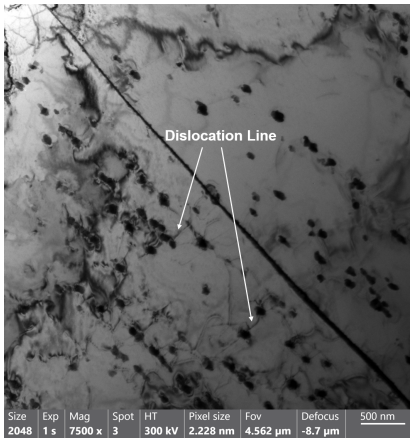

(a) TEM image showing low angle grain boundary with precipiates and dislocation lines.

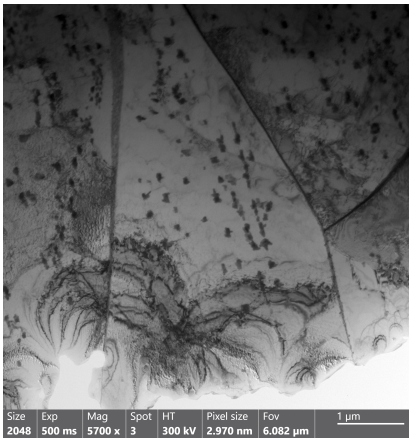

(b) TEM image showing larger electron transparent area.

Figure 5.15: TEM image of the stress-affected region taken from FSHS tested under 130 MPa (Lifetime 2487.2 h).

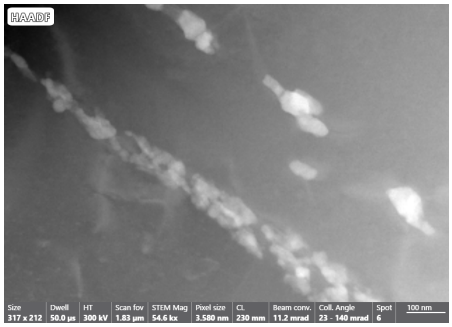

(a) TEM image.

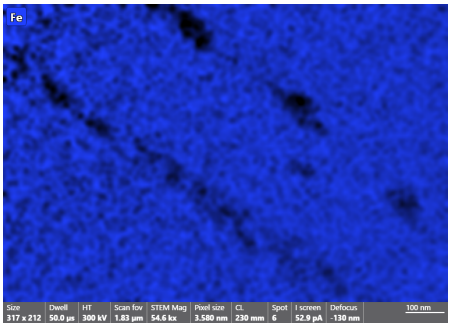

(b) Elemental map of Fe.

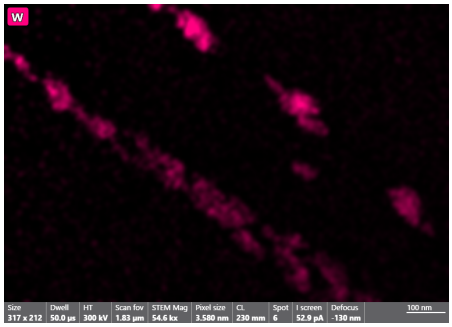

(c) Elemental map of W.

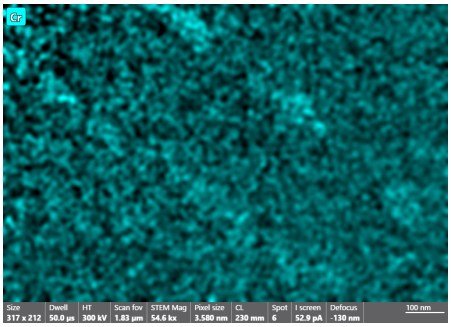

(d) Elemental map of Cr.

Figure 5.16: TEM image and elemental maps showing both low angle grain boundary precipitates and matrix precipitates in FSHS tested under 130 MPa (Lifetime 2487.2 h).

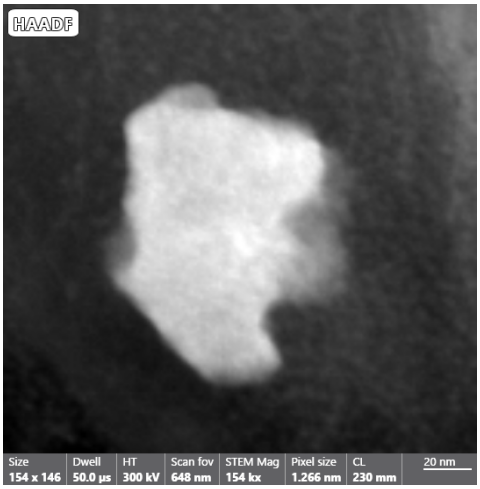

(a) TEM image.

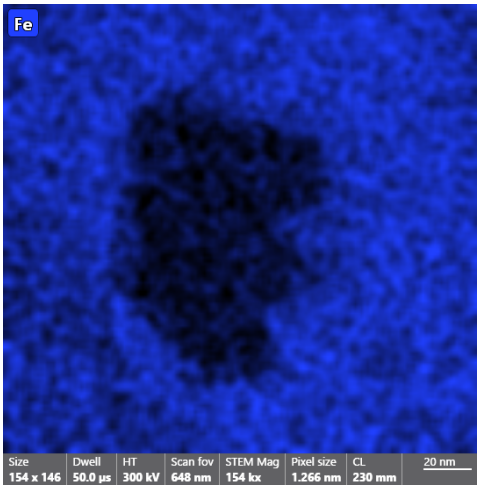

(b) Elemental map of Fe.

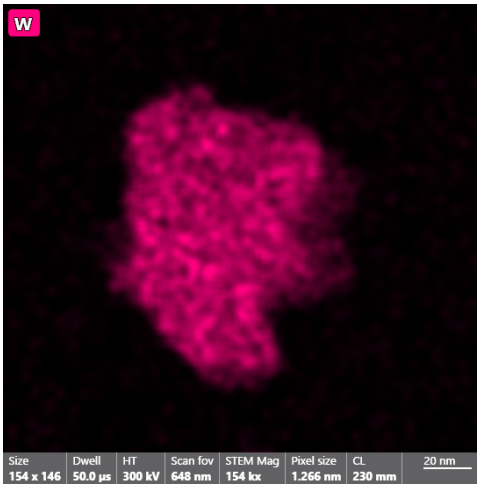

(c) Elemental map of W.

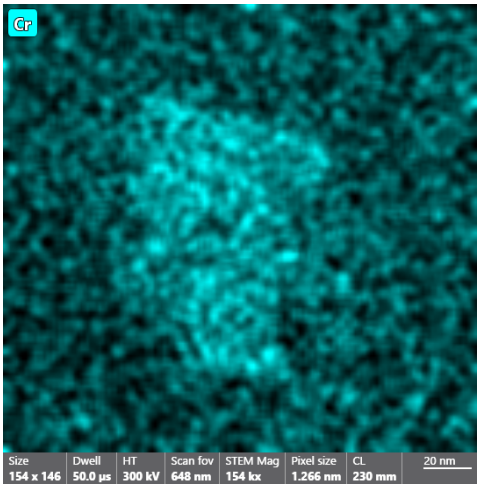

(d) Elemental map of Cr.

Figure 5.17: TEM image and elemental maps showing single matrix precipitate in FSHS tested under 130 MPa (Lifetime 2487.2 h).

(a) TEM image.

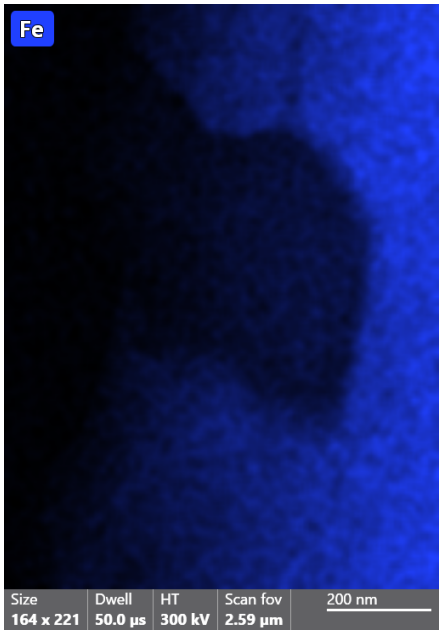

(b) Elemental map of Fe.

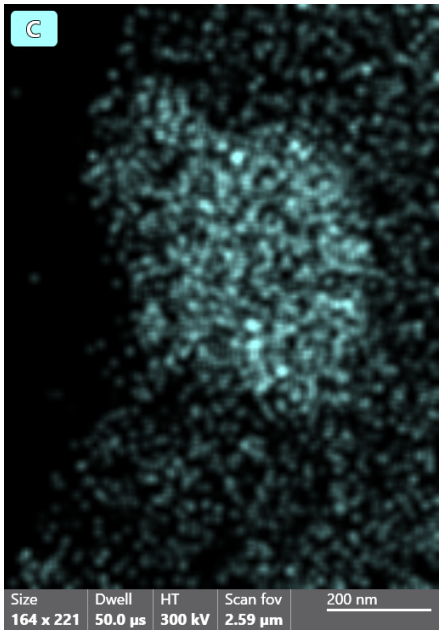

(c) Elemental map of C.

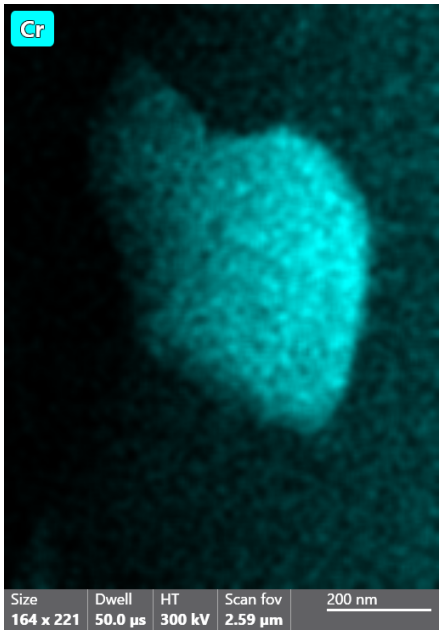

(d) Elemental map of Cr.

Figure 5.18: TEM image and elemental maps showing $M_{23}C_6$ precipitate in FSHS tested under 130 MPa (Lifetime 2487.2 h).

	C	Si	Cr	Mn	Fe	W
EDX result						
Laves phase	~0	7	20	0.4	55	18
Matrix	~0	2	13	1.2	84	0.3
Thermo-calc result (Equilbrium Status)						
Laves phase	0	0.6	18	~0	48	33
Matrix	~0	1.6	13	0.02	85	0.09

Table 5.2: EDX measured and Thermo-calc calculated Laves phase and matrix composition in FSHS sample with a lifetime of 2487.2 hours (in at.%).

	C	Si	Cr	Mn	Fe	W
EDX result						
$M_{23}C_6$	11	0	55	0.4	30	4

Table 5.3: EDX measured $M_{23}C_6$ composition in FSHS sample with a lifetime of 2487.2 hours (in at.%).

SSHS

The overview BSE images of SSHS were taken at the polished stress-affected region as shown in Figure 5.19. The tensile direction is marked in Figure 5.19a using a black arrow. The image of the as-quenched SSHS sample is also provided as a reference. Similar to FSHS, $M_{23}C_6$ were also observed in creep-failed SSHS samples with different lifetime and as-quenched SSHS samples. However, the number density of $M_{23}C_6$ in SSHS is lower than in FSHS, and the $M_{23}C_6$ precipitates SSHS show a more dispersed distribution according to direct observation. The healing in SSHS is designed to initiate after approximately 27000 hours in service. Given that the most extended lifetime of SSHS obtained in this research is 1433.3 hours, none of the tested SSHS samples should present W-rich Laves phase precipitates. Zoom-in investigations are conducted on SSHS samples to verify this assumption. The zoom-in BSE images of the stress-affected regions taken from creep-failed SSHS samples are shown in Figure 5.20. Some bright precipitates are observed at the grain boundaries in the stress-affected regions taken from creep-failed SSHS samples with a lifetime of 307.5 hours (Figure 5.20b) and 1433.3 hours (Figure 5.20b). These grain boundary precipitates could be W-rich Laves phase precipitates. To verify the identification of W-rich Laves phase shown in Figure 5.20, EDX scanning was conducted on the etched stress-affected region of the SSHS sample with a lifetime of 1433.3 hours. The scanned area, together with the tungsten map (at.%), are shown in Figure 5.21. The contour of the tungsten map matches the bright areas in the BSE image, indicating the bright areas are indeed W-rich Laves phase. Besides, the W-rich Laves phase precipitates show obvious grain boundary preference in SSHS.

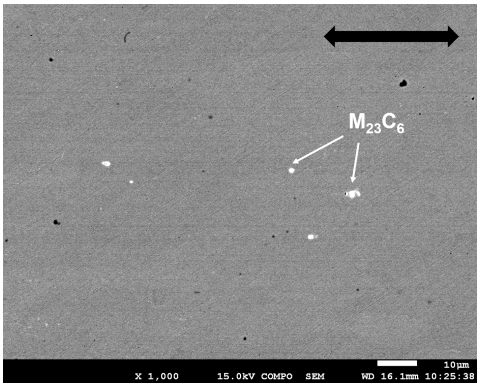

(a) Tested under 140 MPa (Lifetime 33.6 h).

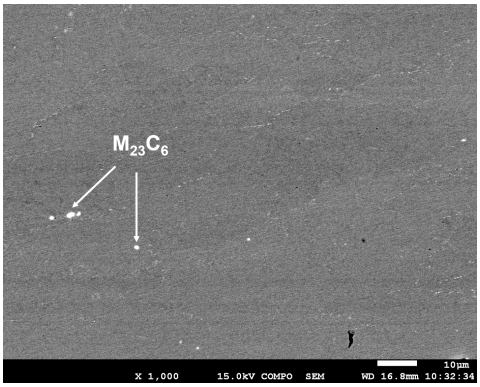

(b) Tested under 120 MPa (Lifetime 307.5 h).

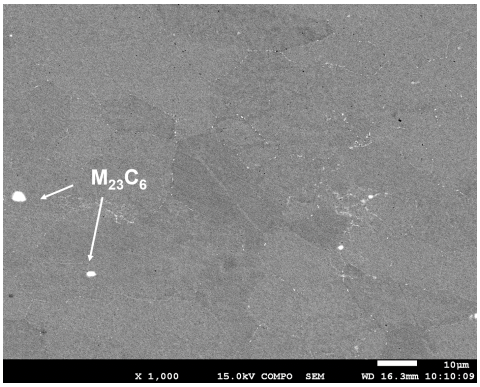

(c) Tested under 100 MPa (Lifetime 1433.3 h).

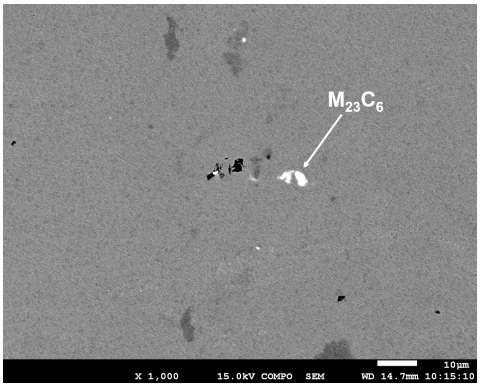

(d) As-quenched.

Figure 5.19: BSE image of stress-affected region taken from SSHS creep-failed samples and as-quenched sample.

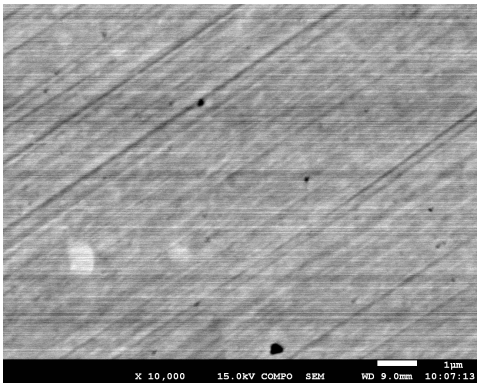

(a) Tested under 140 MPa (Lifetime 33.6 h).

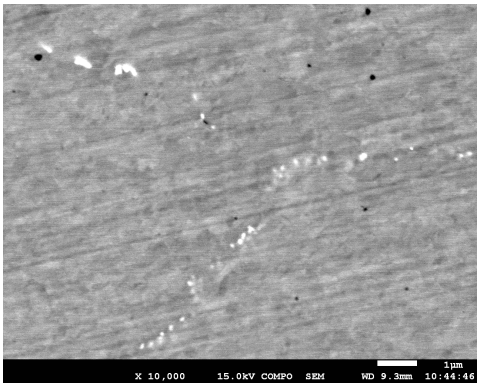

(b) Tested under 120 MPa (Lifetime 307.5 h).

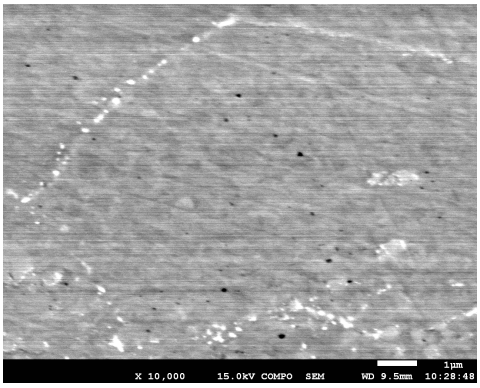

(c) Tested under 100 MPa (Lifetime 1433.3 h).

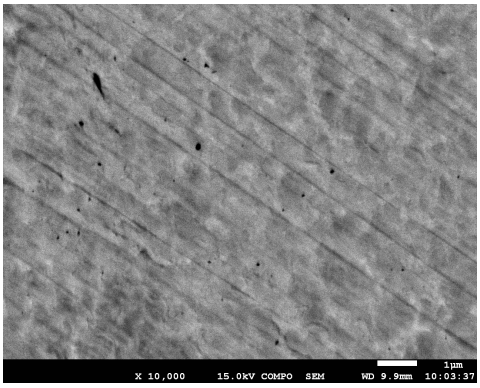

(d) As-quenched.

Figure 5.20: BSE image of stress-affected region taken from SSHS creep-failed samples and as-quenched sample with higher magnification.

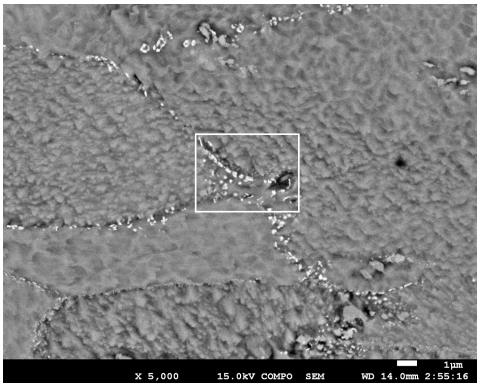

(a) BSE image of the stress-affected region from SSHS sample tested under 100 MPa (lifetime 1433.3 h).

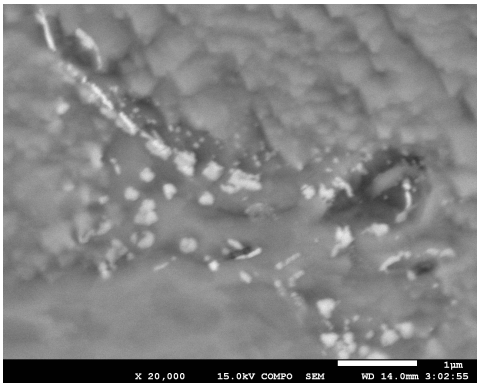

(b) Zoom-in image (marked by white square) showing W-rich Laves phase.

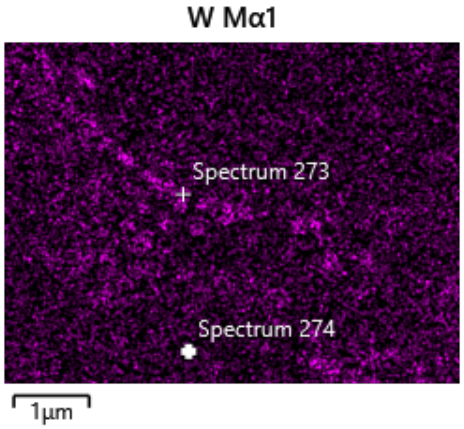

(c) EDX atom percent map of tungsten.

Figure 5.21: W-rich Laves phase in SSHS tested under 100 MPa (lifetime 1433.3 h) and EDX map of tungsten.

5.2.3. Stress-Free Region

FSHS

The primary purpose of self-healing in creep-resistant steel is to fill the creep-induced damage autonomously, and one of the most crucial criteria is that the healing agent should not be wasted in the matrix when there is no damage. The investigation on microstructure evolution for unstressed but thermally exposed materials were also conducted. The SEM images of the stress-free regions in each samples were taken from the clamping area as illustrated by red region in Figure 5.22.

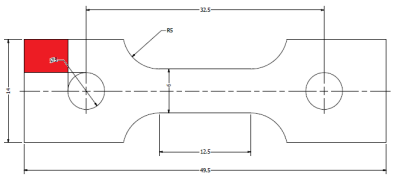

Figure 5.22: Schematic illustration the stress-free region in creep-failed samples.

The overview BSE images of creep-failed FSHS samples were taken at the polished stress-free region as shown in Figure 5.23. The image of the as-quenched FSHS sample is provided as a reference. Similar to stress-affected regions, both $M_{23}C_6$ and dark spots are observed in all of the samples, irrespective of the elevated temperature exposure time. As shown in Figure 5.13c and Figure 5.23c, the grain boundaries in FSHS sample with a lifetime of 2487.2 hours are relatively clearer than other samples. The grains are elongated according to the tensile direction in Figure 5.13c, while the grains maintain an equiaxed shape in Figure 5.23c. Zoom-in investigations were conducted on the stress-free regions as shown in Figure 5.24. W-rich precipitates are observed in the stress-free region of the sample with a lifetime of 2487.2 hours (Figure 5.24c).

The dark areas/spots generally exist in all samples in stress-affected and stress-free areas. Some of them are pores, while others are Si/C-rich impurities. Because characterizing the evolution of pores and cavities is significant in this study, distinguish the pores from the impurities is also vital. EDX scanning was done in the stress-free region of FSHS with a lifetime of 465.3 hours shown in Figure 5.25a, where a large dark area with sharp edges is shown, the zoom-in area is shown in Figure 5.25b. The EDX scanning atom percent maps of silicon and carbon are shown in Figure 5.25c and Figure 5.25d, respectively. The Si-rich area corresponds with the dark area shown in the BSE image, indicating that the dark area is indeed Si-rich impurities. The Si/C-rich impurities in the samples are generally large (over 1 μm) and have sharp edges.

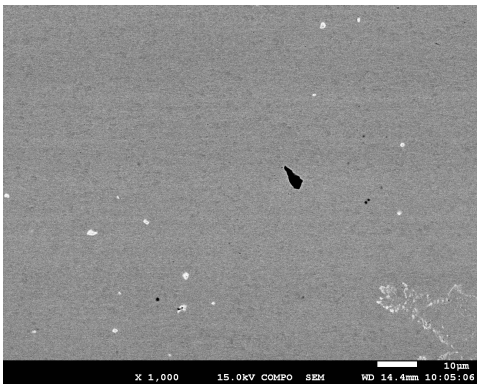

(a) FSHS sample with a lifetime of 73.9 hours.

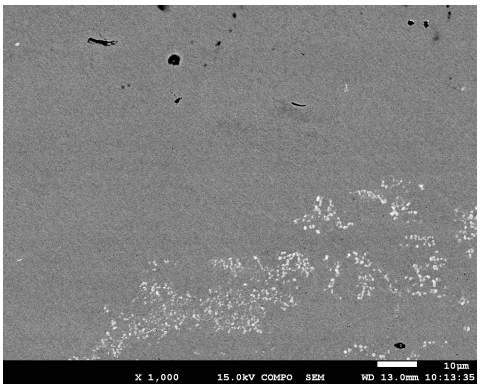

(b) FSHS sample with a lifetime of 465.3 hours.

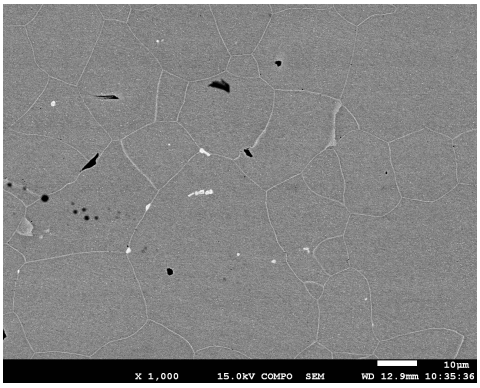

(c) FSHS sample with a lifetime of 2487.2 hours.

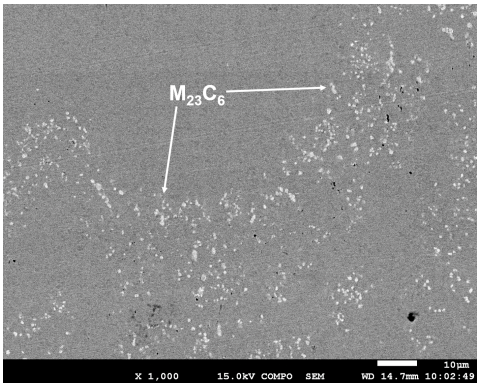

(d) As-quenched

Figure 5.23: BSE image of stress-free region taken from FSHS creep-failed samples and as-quenched sample.

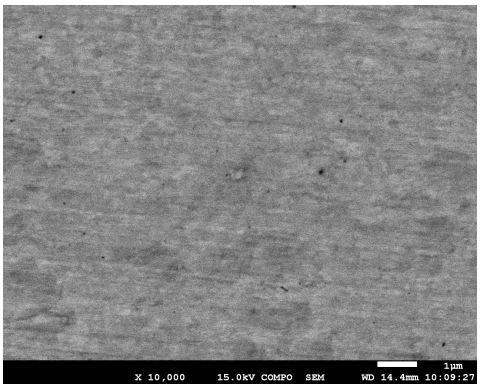

(a) FSHS sample with a lifetime of 73.9 hours.

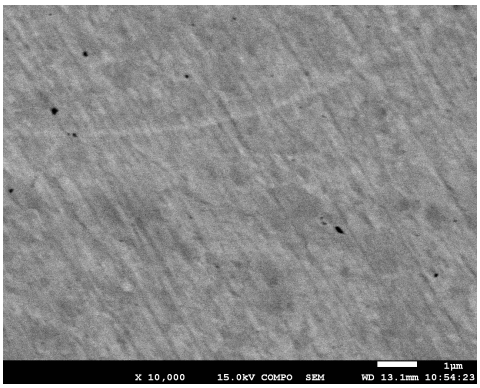

(b) FSHS sample with a lifetime of 465.3 hours.

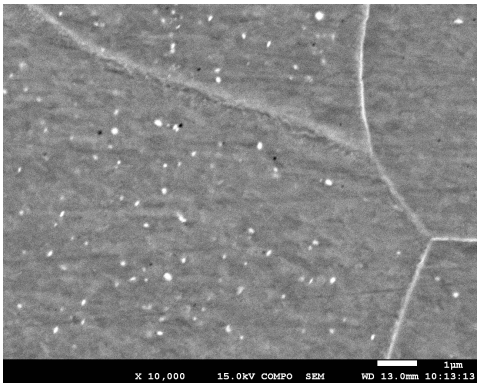

(c) FSHS sample with a lifetime of 2487.2 hours.

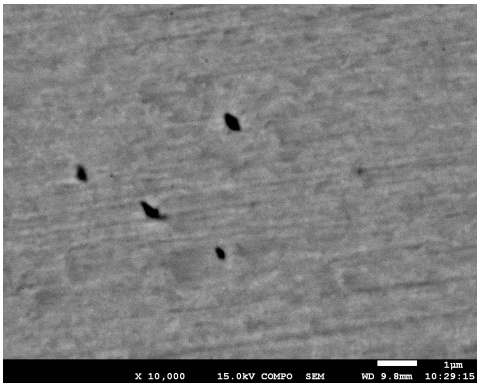

(d) As-quenched

Figure 5.24: BSE image of stress-free region taken from FSHS creep-failed samples and as-quenched sample with higher magnification.

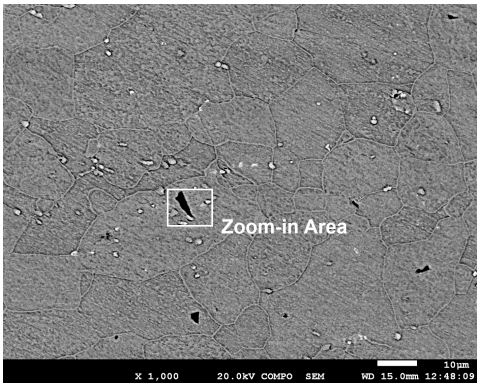

(a) Stress-free region of FSHS with a lifetime of 465.3 hours.

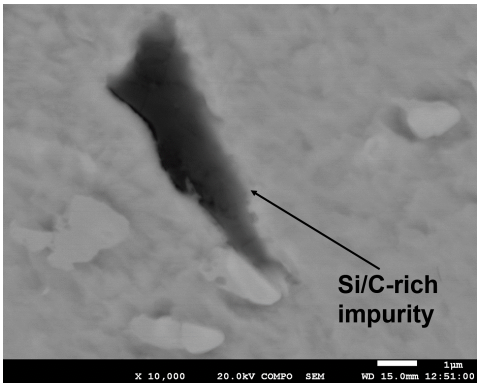

(b) Zoom-in view of Figure 5.24a showing the Si-rich impurty.

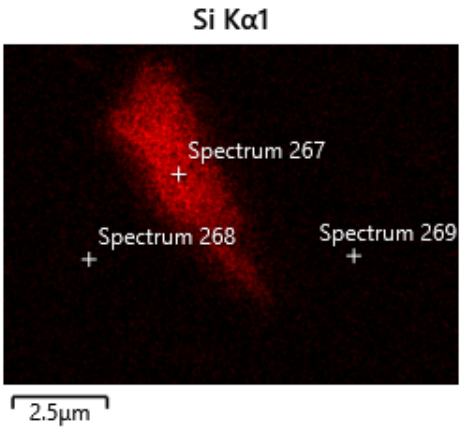

(c) EDX atom percent map of silicon.

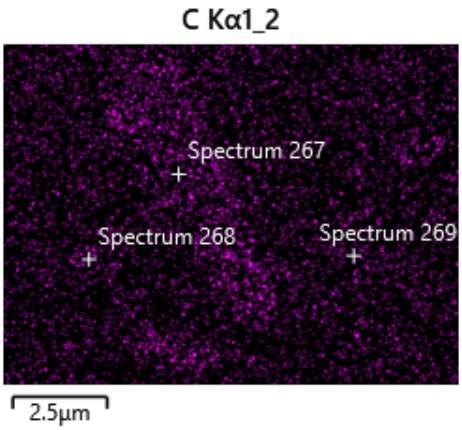

(d) EDX atom percent map of carbon.

Figure 5.25: Images showing a Si/C-rich impurity and relevant EDX elemental scanning maps.

SSHS

SEM observations was also conducted on the stress-free regions in SSHS samples with different lifetimes. The overview and zoom-in BSE images are shown in Figure 5.26 and Figure 5.27 respectively. The general characterisitcs of $M_{23}C_6$ precipitates and Si/C-rich impurities remain the same as the stress-affected regions. However, the W-rich precipitates are observed at the grain boundaries in the stress-free region of the SSHS with the lifetime of 1433.3 hours (Figure 5.27a), similar to the stress-affected region.

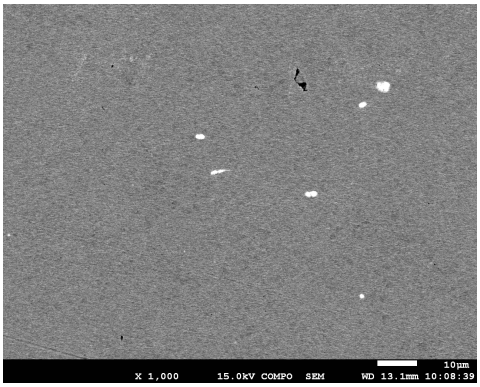

(a) SSHS sample with a lifetime of 33.6 hours.

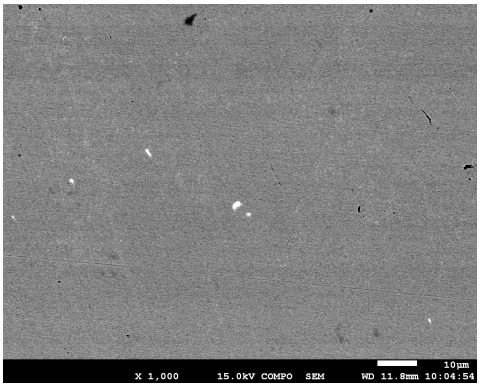

(b) SSHS sample with a lifetime of 307.5 hours.

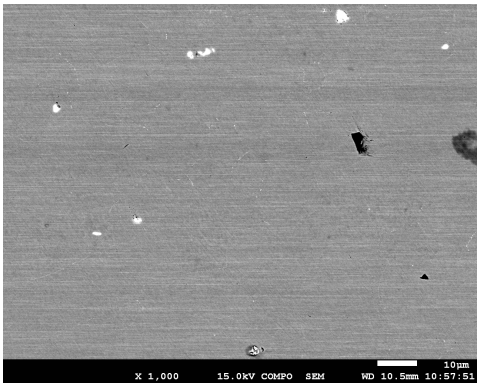

(c) SSHS sample with a lifetime of 1433.3 hours.

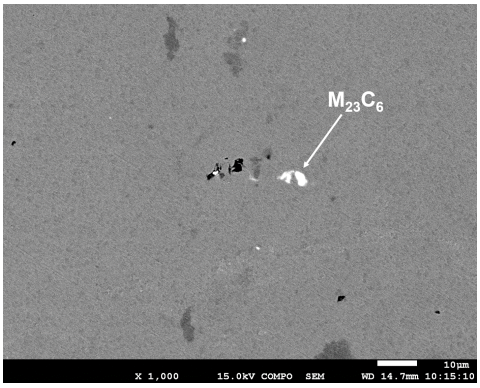

(d) As-quenched

Figure 5.26: BSE image of stress-free region taken from SSHS creep-failed samples and as-quenched sample.

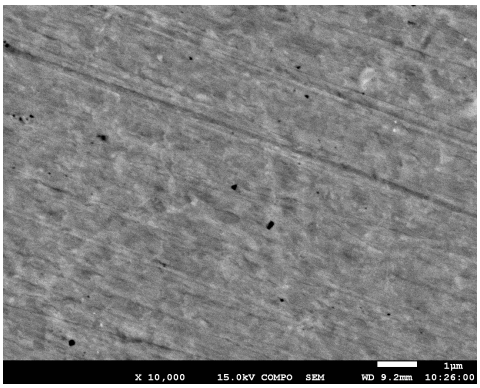

(a) SSHS sample with a lifetime of 33.6 hours.

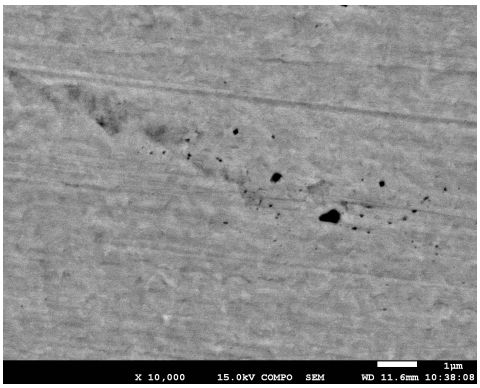

(b) SSHS sample with a lifetime of 307.5 hours.

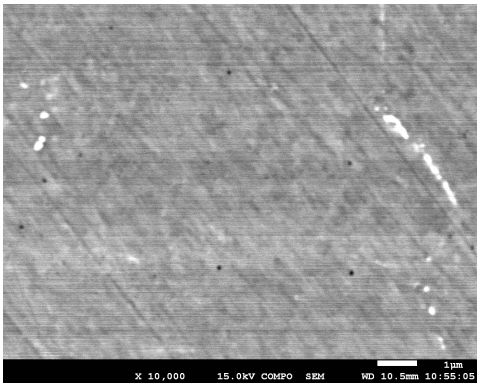

(c) SSHS sample with a lifetime of 1433.3 hours.

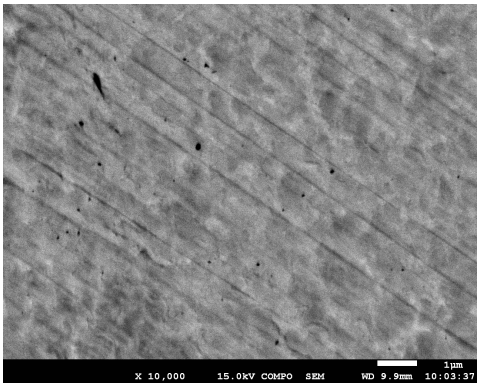

(d) As-quenched

Figure 5.27: BSE image of stress-free region taken from SSHS creep-failed samples and as-quenched sample with higher magnification.

5.2.4. Cavity Statistics

The healing in the newly designed 12Cr self-healing ferritic steel is dedicated to creep damage filling, which implies that the formation of creep cavities, such as wedge cracks or r-type cavities, is the prerequisite for the healing to come into effect. Investigation of the pores and cavities observed through SEM observation is needed to evaluate the performance of the newly designed 12Cr self-healing ferritic steel. Statistics of the pores and cavities are obtained from SSHS tested under 140 MPa (lifetime 33.6 h), 120 MPa (lifetime 307.5 h), and 100 MPa (lifetime 1433.3 h), as well as FSHS tested under 180 MPa (lifetime 73.9 h), 150 MPa (lifetime 465.3 h), and 130 MPa (lifetime 2487.2 h). Images were taken from both stress-affected and stress-free regions for each testing condition. The number and size of the pores were counted and measured using an open-source software named ImageJ. Eight random sites with a magnification of 10000 were taken to calculate the pores' number density. The number density is calculated by N/A, in which N is the number of pores found in one site, and A is the area of the site. SEM images with a magnification of 50000 were also taken to calculate the average size of the pores. Ten pores are involved in the statistics for each gauge area and stress-free areas. The size of the pores is described by equivalent diameter, d, in which the pores are considered circular and $d = \sqrt{A/\pi} * 2$. The pore statistics of as-quenched FSHS and SSHS are also obtained as references. Besides, all of the SEM images were taken from the polished surfaces without etching to prevent etching influence. The example of the BSE image used is shown in Figure 5.28 and Figure 5.29; the image was taken from stress-affected and stress-free areas of FSHS tested under 130 MPa, and SSHS tested under 100 MPa. The pores observed in these samples generally distribute randomly in the matrix and have no site preferences. To avoid taking Si/C-rich impurities as pores, secondary electron (SE) images were also compared for each site to double-check if the dark sites are pores or not; an example is provided in Figure 5.30.

The damage evolution is characterized by average number density and average equivalent diameter of the pores with respect to stress and lifetime. The data is presented in the form of net values (e.g., value of stress-affected region - value of corresponding stress-free region), as plotted in Figure 5.31 and Figure 5.32 for FSHS and SSHS, respectively.

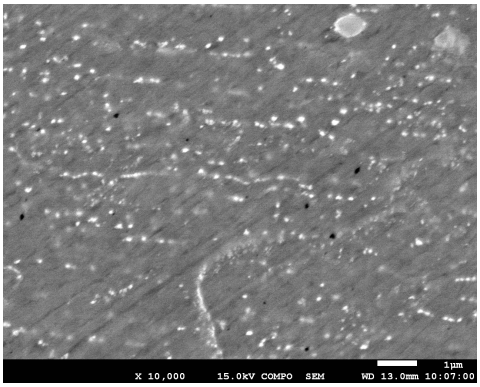

(a) Stress-affected region (magnification × 10000).

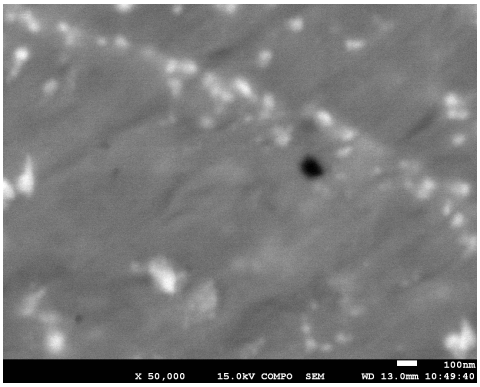

(b) Stress-affected region (magnification × 50000).

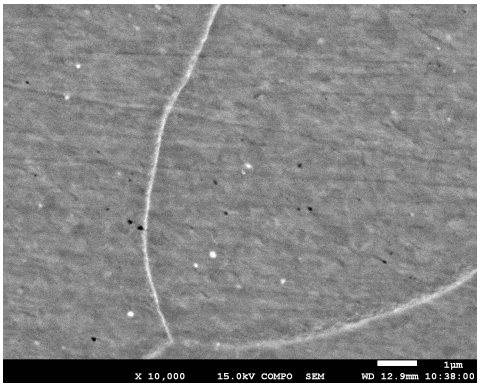

(c) Stress-free region (magnification × 10000).

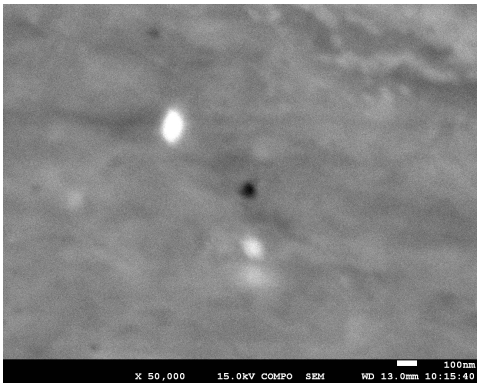

(d) Stress-free region (magnification × 50000.)

Figure 5.28: Example BSE images used for pore statistics taken from FSHS tested under 130 MPa (Lifetime 2487.2).

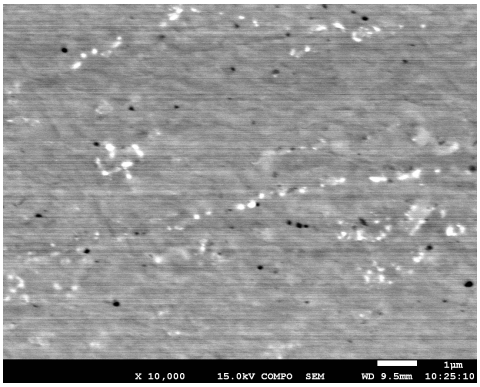

(a) Stress-affected region (magnification × 10000).

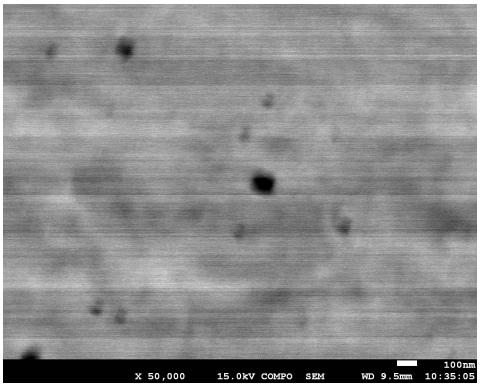

(b) Stress-affected region (magnification × 50000).

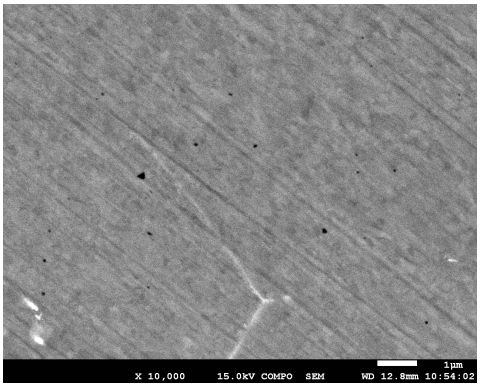

(c) Stress-free region (magnification × 10000).

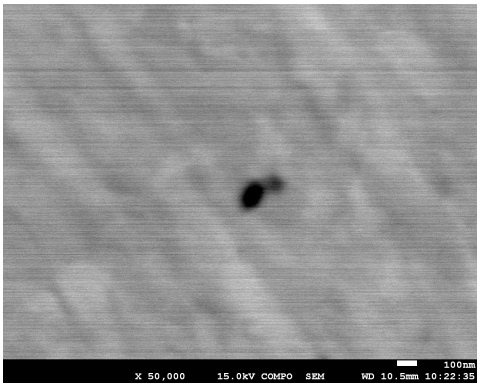

(d) Stress-free region (magnification × 50000.)

Figure 5.29: Example BSE images used for pore statistics taken from SSHS tested under 100 MPa (1433.3 h).

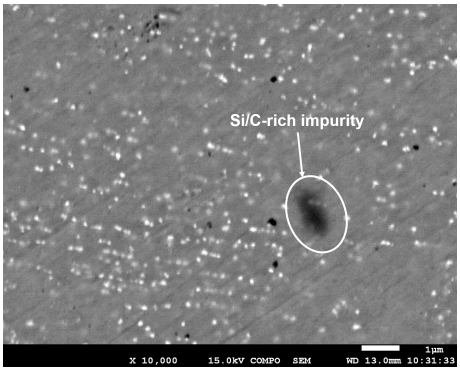

(a) BSE image.

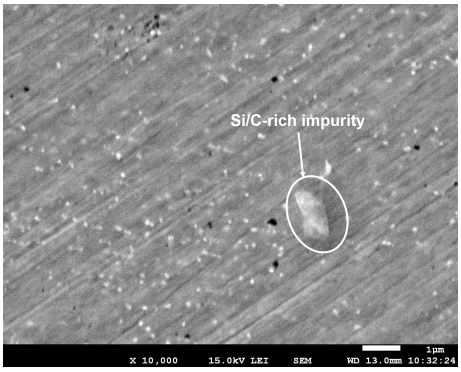

(b) SE image.

Figure 5.30: Same site but different electron signal image for pore statistics taken from FSHS tested under 130 MPa (Lifetime 2487.2 h).

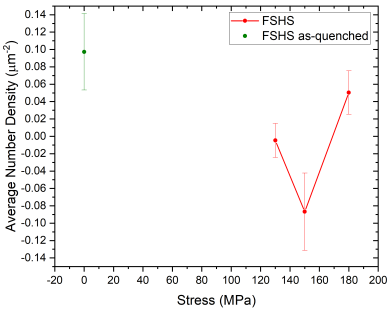

(a) Average number density vs. applied stress.

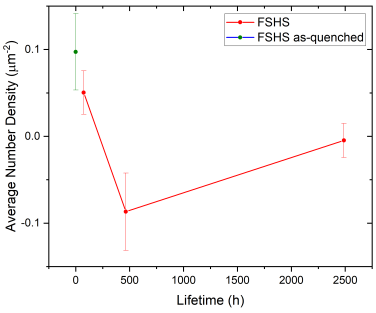

(b) Average number density vs. lifetime.

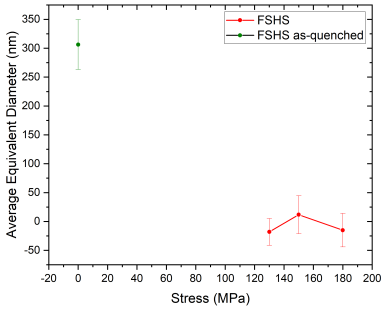

(c) Average equivalent diameter vs. stress.

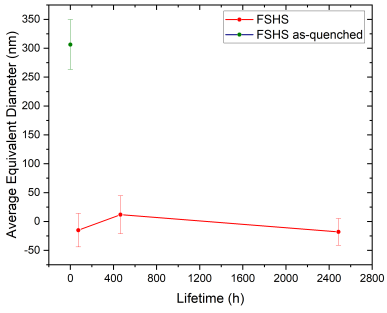

(d) Average equivalent diameter vs. lifetime.

Figure 5.31: Pore statistics in FSHS.

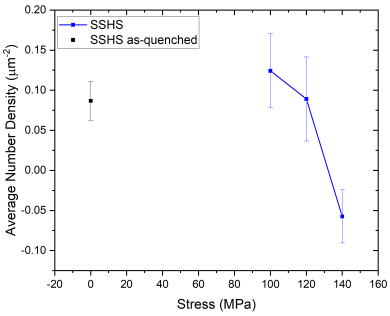

(a) Average number density vs. applied stress.

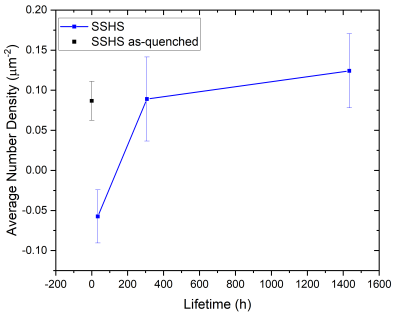

(b) Average number density vs. lifetime.

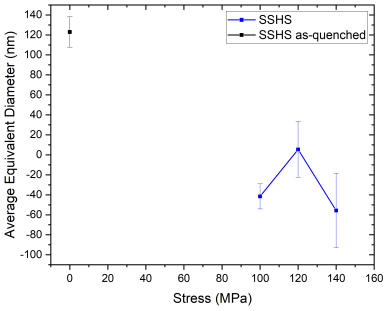

(c) Average equivalent diameter vs. stress.

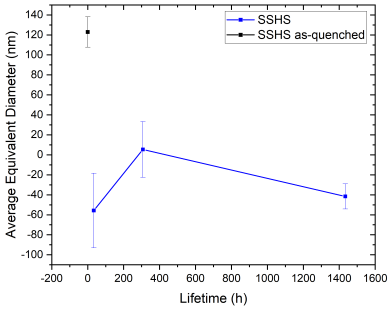

(d) Average equivalent diameter vs. lifetime.

Figure 5.32: Pore statistics in SSHS.

5.2.5. Laves Phase Precipitates Statistics

The Laves phase precipitates in FSHS were investigated using similar counting methods. Eight random sites were taken at the etched stress-affected and stress-free regions in FSHS tested under 130 MPa, 150 MPa, and 180 MPa. The BSE images were taken at the magnification of 20000. The number of the precipitates and their covered areas were counted and calculated using the open-source software ImageJ. For each site, the number densities of the precipitates were calculated using the same method as mentioned in the cavity development analysis, and the covered area percentage is calculated by $A_{Precipitate}/A_{FOV}$, in which FOV stands for field of view. W-rich Laves phase precipitates are observed in stress-affected and stress-free regions in the FSHS sample with a lifetime of 2487.2 hours and stress-affected regions in the FSHS sample with a lifetime of 465.3 hours; the example BSE images of the regions mentioned above are shown in Figure 5.33. The Laves phase precipitates are observed in the matrix and grain boundaries. The grain boundary precipitates are not taken into account since their contours are not clear enough for counting. The average number density and average precipitate area fraction are plotted against lifetime as shown in Figure 5.34.

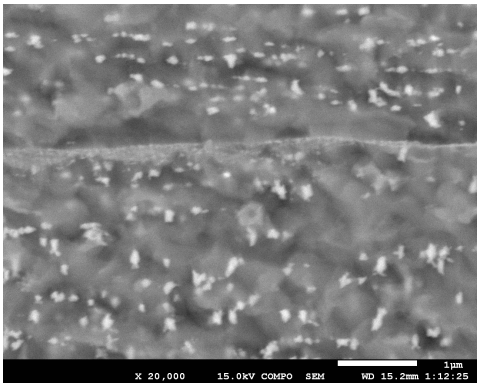

(a) Stress-affected region of FSHS with a lifetime of 2487.2 hours.

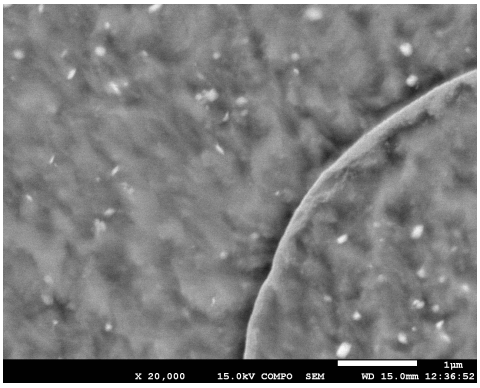

(b) Stress-free region of FSHS with a lifetime of 2487.2 hours.

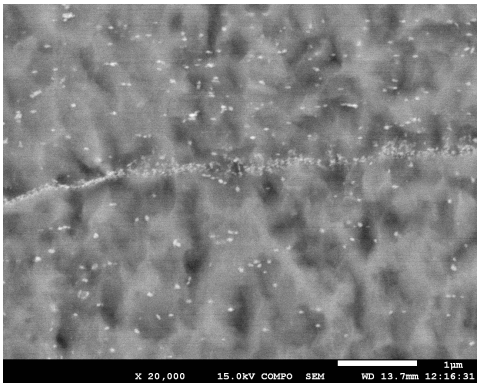

(c) Stress-affected region of FSHS with a lifetime of 465.3 hours.

Figure 5.33: Example BSE images used for precipitate statistics.

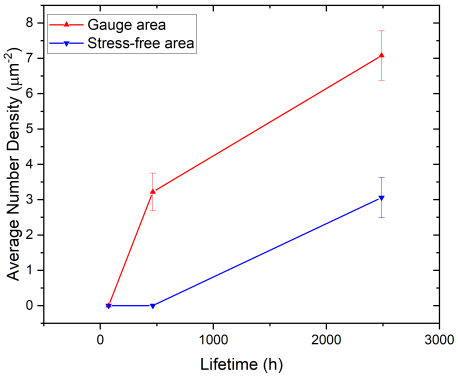

(a) Average number density vs. lifetime.

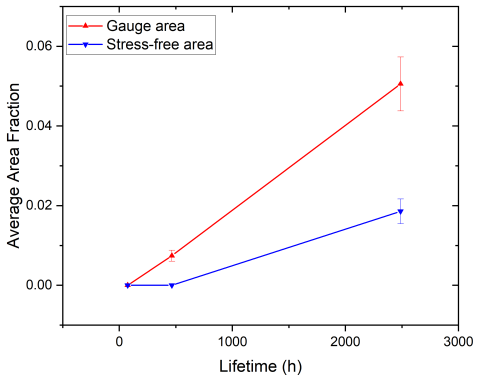

(b) Average precipitate area fraction vs. lifetime.

Figure 5.34: Lifetime dependence of the precipitate statistical data in FSHS.

6

Discussion

6.1. Creep-Rupture Properties

The overall creep behavior, including primary, secondary, and tertiary creep stages of FSHS and SSHS, shows a relatively conventional behavior and is in agreement with traditionally designed 9-12Cr ferritic steels [22, 23, 26, 74, 111]. Comparing the strain rate-strain plots between FSHS and SSHS, it is found that the creep rate for SSHS shows a sheer drop at an early stage and maintains a quasi-steady pattern before entering the tertiary creep stage, while the creep rate for FSHS shows a sheer drop at an early stage of the creep followed by a steady increase for samples tested above 180 MPa (including 180 MPa), the boundary between creep stages is not easy to identify. The FSHS samples tested below 180 MPa show similar trends to SSHS. Such phenomena can also be found in strain rate-time plots, except that the strain rate variation for SSHS is more prominent over time.

The relation between minimum creep rate and lifetime is usually characterized by the Monkman-Grant relationship (MGR) [112], and modified Monkman-Grant relationship (MMGR) [113]. The generalized form of these two relationships are shown in equation 5.1 and equation 5.2, respectively, where $\dot{\epsilon}_{min}$ is the minimum creep rate, t_r is the lifetime, ϵ_f is the strain to failure, α, α', C, and C' are constants. The modified Monkman-Grant relationship is used to reduce the scattering in the data caused by large tertiary creep and a decrease in creep strain to failure with increasing rupture life.

$$\dot{\epsilon}_{min}^{\alpha} \cdot t_r = C \tag{6.1}$$

$$\dot{\epsilon}_{min}^{\alpha'} \cdot \frac{t_r}{\epsilon_f} = C' \tag{6.2}$$

The MGR and MMGR is valid when ploting t_r or t_r/ϵ_f against $\dot{\epsilon}_{min}$ under double logarithmic scale, and α or α' equals to 1. The constant C or C' will then become C_{MG} or C_{MMG}. The $log t_r$ vs. $log\dot{\epsilon}_{min}$ and $log(t_r/\epsilon_f)$ vs. $log\dot{\epsilon}_{min}$ of FSHS and SSHS are plotted in Figure 6.1a and Figure 6.1b. The slopes of SSHS in both of the

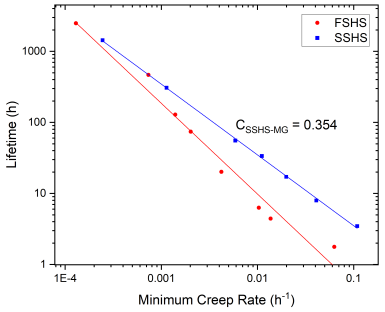

(a) Rupture time vs. minimum creep rate plot of FSHS and SSHS.

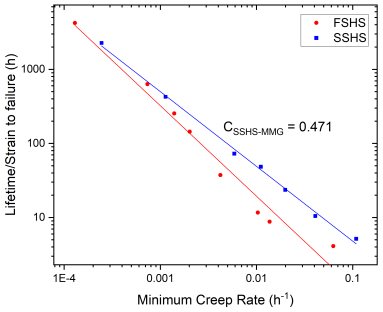

(b) Rupture time/strain to failure vs. minimum creep rate plot of FSHS and SSHS.

Figure 6.1: Validation graph of the MGR and MMGR in FSHS and SSHS.

graphs are very close to -1, which means SSHS obeys the MGR and MMGR, and

the calculated constants are $C_{SSHS-MG} = 0.354$ and $C_{SSHS-MMG} = 0.471$. However, the slopes of FSHS in $logt_r$ vs. $log\dot{\epsilon}_{min}$ and $log(t_r/\epsilon_f)$ vs. $log\dot{\epsilon}_{min}$ are -1.28 and -1.22, respectively, indicating an unstable secondary creep and possible shift in creep mechanisms between higher stress range (180-260 MPa) and lower stress range (130-180 MPa), which corresponds to the different strain rate-strain behavior between these two stress ranges as mentioned before. Choudhary and Samuel [22] reported the MGR and MMGR constant in their modified 9Cr-1Mo tested under different stresses at 550 °C, 575 °C, and 600 °C as $C_{MG} = 0.036$ and $C_{MMG} = 0.205$. They also mentioned that their relatively low values of C_{MG} and C_{MMG} indicate a small contribution of secondary creep strain to overall creep strain. Comparing the MGR and MMGR between SSHS and modified 9Cr-1Mo steel, the MGR constant of SSHS is almost ten times higher while the MMGR constant is two times higher than the modified 9Cr-1Mo steel, which means it is reasonable to infer a relatively higher contribution of secondary creep strain to overall creep strain in SSHS qualitatively. Moreover, the FSHS tested at lower stresses (130-180 MPa) with a similar quasi-steady stage as the SSHS could possess similar characteristics. The contribution of secondary creep strain to overall creep strain in FSHS tested at higher stresses (180-260 MPa) becomes less. This is consistent with the creep results as shown in section 5.1, where the strain rates for FSHS with high applied stresses (> 180 MPa) keep increasing during creep, instead of showing a steady secondary stage.

The overall strain of both FSHS and SSHS is relatively high compared to traditionally designed ferritic steels. The rupture elongation data of 12Cr steel from NIMS data sheet [74] together with elongation data of FSHS and SSHS are plotted against their lifetime using a common scale, as shown in Figure 6.2. A reference line is drawn at the strain of 0.5, among 72 data points obtained from NIMS datasheet, 28 data points stay beyond this value, which gives 38.9% of traditional 12Cr steel samples have a rupture strain beyond 0.5. For all the tested FSHS and SSHS samples, this ratio is 75% and 100%, respectively.

The lifetime of two traditional 12Cr steels, FSHS, and SSHS, is plotted against the applied stress to investigate the effect of self-healing design to creep lifetime, as shown in Figure 6.3. Among the 4 groups of steels, the 12Cr-2W-0.4Mo-1Cu-Nb-V steels show the highest lifetimes at the same stress level, mainly due to the precipitation straightening effect provided by MX precipitates. The FSHS and SSHS steels show comparable lifetimes with 12Cr steels, especially in the low-stress regime. Due to disobedience of the Monkman-Grant relationship and the design of the healing initiation time of FSHS, the linear regression for FSHS in Figure 6.3 is done separately in this chapter. The data dots of FSHS are divided into two groups. One is shown green in the graph, which has a lifetime longer than or close to the designed healing initiation time of the FSHS; the other is shown red in the graph, which has a lifetime shorter than the designed healing initiation time. However, the later microstructural investigation does not show expected cavity filling behavior. One of the reasons for the ”kink” shown in FSHS data could be a shift in the creep mechanism as the stress changes. The power law coefficients and exponents of these three groups of data are shown in Table 6.1.

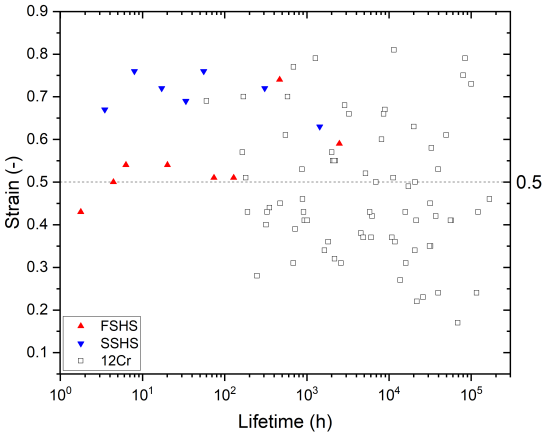

Figure 6.2: Strain at fracture vs. lifetime of FSHS, SSHS, and traditional 12Cr steel

Alloy Type	$t_R = A'\sigma^{-n'}$	
	A′ ($MPa^n h$)	n′
FSHS-SH	$10^{33\pm4}$	13.8 ± 2.0
FSHS-non-SH	$10^{24\pm2}$	9.8 ± 0.8
SSHS	$10^{22\pm1}$	9.4 ± 0.6

Table 6.1: Values of power law coefficients and stress exponents for the stress dependence of lifetime in Figure 6.3.

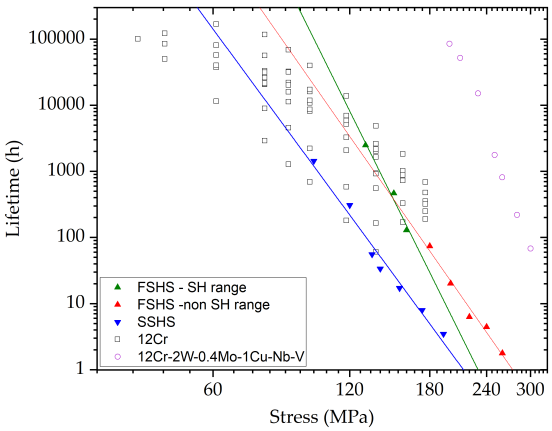

Figure 6.3: Stress dependence of lifetime for FSHS, SSHS, and traditional 12Cr steel.

The stress used to test the 12Cr self-healing ferritic steels in this research was relatively high compared to the testing stress used in NIMS data sheet for traditional 12Cr ferritic steel. Under such testing conditions, the FSHS and SSHS have much higher stress exponents than the traditional 12Cr ferritic steel with a similar average grain size. Relatively high values of stress exponents were found in many previous studies related to 9-12Cr ferritic steels tested in their high-stress regimes [22, 23, 26, 114–116]. The dislocation-controlled creep seems to be the dominant creep mechanism for modified 9Cr-1Mo (ASME Gr. 91) ferritic steel tested under high-stress regimes since the high exponent in power-law reveals dislocation domination in the creep deformation [22]. The dominance of the power-law breakdown (PLB) mechanism, known as one of the dislocation controlled creep mechanisms, was also found in G115 (9Cr) ferritic steel tested under high stresses. TEM image showing complicated dislocation structures in the tested samples provided further proof [110]. For the 12Cr self-healing ferritic steels showing high stress exponents and high strain before fracture, dislocation involvement is expected to be high. TEM images in the previous chapter with dislocation lines also provide experimental evidence for extensive dislocation involvement during creep deformation in the self-healing ferritic steels. Therefore, under current testing conditions, the dominant creep mechanism of 12Cr ferritic self-healing steels are likely to be the dislocation-dominated creep, despite some of the analysis being based on the behavior of 9Cr ferritic steels tested under their high stress regime.

In conclusion, the creep lifetime is comparable with traditional 12Cr steel; a detailed comparison reveals that FSHS and SSHS could surpass traditional 12Cr steel with similar average grain size in terms of lifetime if tested in lower stresses. The newly designed FSHS and SSHS have pretty high stress exponent and creep strain before rupture compared to traditional 12Cr steel. Compared with other 9-12Cr traditional ferritic steels, the dislocation controlled creep is considered the dominant creep mechanism in FSHS and SSHS under testing conditions in this research.

6.2. Cavity Development

As an essential premise for self-healing, creep cavities and damage observed in section 5.2.4 are discussed. The cavities generally have no site preference and show a random distribution over the observed area according to the example images shown in Figure 5.28 and Figure 5.29. The statistics show hardly any tendency in average number density and average equivalent diameter with respect to stress or lifetime for both FSHS and SSHS. Some abnormal data, such as negative average number density or negative equivalent diameter, implies that the pores found in the samples were not a result of creep. The nucleation and growth of the creep cavity have a close relationship with diffusion, which means the creep time plays a significant role in the size of creep cavities. In the creep cavity nucleation and growth model constructed by Ahmadi et al. [30], the creep cavity growth rate and mean diameter were both creep time-dependent functions. As a more intuitionistic comparison, in the creep test to verify their model, a traditional 9Cr ferritic steel sample tested for 8030 hours has an average pore diameter of 82 ± 6 nm, while the average pore diameter in FSHS tested for 2487 hours already reached 89 ± 12 nm.

Consequently, the pores found in FSHS and SSHS are considered to form before creep tests and are not related to creep.

Transgranular fracture and absence of typical creep damage in the form of wedge cracks or r-type cavities were reported for modified 9Cr-1Mo (ASME Gr. 91) ferritic steels being tested under high stress regime [22, 117, 118]. The absence of typical creep damage was attributed to the absence of precipitate free zone (PFZ) [117–119], which promotes strain concentration and subsequently promotes cavity nucleation and growth [120]. Some also suggest that the grain boundary cohesion of 9Cr-1Mo ferritic steel is high, and the strength of the matrix is similar to the strength of the grain boundaries, which reduces the stress concentration and is not in favor of grain boundary cavitation [117, 119]. However, the absence of creep cavities in FSHS and SSHS is unlikely to be attributed to the absence of PFZ as no aging treatments were performed on the self-healing steels to form strengthening precipitates at the grain boundaries. The matrix's coherency could be one reason for the absence of creep cavities, but it needs further investigation.

Considering the observation of creep cavities, the mean diameter of the creep cavities is also important as the size directly affects whether the cavity could be observed by the characterization methods or not. Wu and Sandström conducted detailed quantitative measurements on creep cavities found in 12Cr-Mo-V steel [27, 28], in which their samples underwent constant load creep tests (σ = 80 MPa, T = 600-670 °C) and constant temperature tests (σ = 90-185 MPa, T = 600°C). It was concluded that the mean cavity diameter is related to strain or creep time. The mean cavity diameter growth rate is positively related to temperature and stress. However, in the constant load tests, lower temperature leads to a larger mean cavity diameter, while in the constant temperature tests, the observed mean cavity diameter first decreases with the increasing stress and then increases with the increasing stress. Therefore, both stress and temperature control the mean cavity diameter at fracture by controlling the growth rate of mean cavity diameter and lifetime. Considering the situation in FSHS and SSHS, the stress used in the tests was relatively high compared to the tests conducted in the NIMS data sheets [74], while the temperature is relatively low compared to the literature [27, 28, 30], in which the creep cavities were observed. With relatively low temperature, the diffusion is less active, and the growth rate of the cavity diameter might be insufficient for the lifetime of FSHS and SSHS to generate observable cavities. The effect of growth rate becomes evident when the lifetime under current testing conditions is short. The chance of observing creep cavities in FSHS and SSHS might be higher if the samples could survive longer. Since the designed service temperature of the self-healing steel is not adjustable in this study, the only way to obtain a longer lifetime is to reduce the testing stress further. This becomes tricky because the mean cavity diameter growth rate will also decrease accrding to the literature results. Nevertheless, further experiment under lower stress is required.

The nucleation and growth of grain boundary cavities are dominated by diffusion, which intrinsically requires sufficient time under stress and elevated temperature. The applied stress should also be kept under a certain level for the diffusion mechanism to dominate. Ahmadi et al. [30] conducted creep tests on grade 91

under 66 MPa at 650 °C, which is a relatively high temperature and low stress, preferable for diffusional creep [121]. The grain boundary cavities were indeed found in the interrupted creep test samples, and the creep cavities' size depends on the creep time. Therefore, a possible reason for the absence of grain boundary cavity could be unsuitable testing conditions applied to FSHS and SSHS, leading to dislocation-dominated creep rather than diffusion-dominated creep. Besides, a relatively short lifetime might also be insufficient for the cavities to nucleate and grow.

The alloying elements could also affect the diffusion behavior of the matrix. According to the investigation on the effect of tungsten on creep behavior of 9Cr steels, the addition of tungsten could reduce the self-diffusion rate and microstructural evolution rate, thus increasing the creep performance by decreasing the minimum creep rate and increasing the apparent activation energy for the minimum creep rate [24]. Because specific reduction in self-diffusion rate was not specified using data and no investigation on creep cavity was conducted, the effect of tungsten on cavity nucleation and growth is not fully understood. The solubility of tungsten in the iron matrix is low, and its effect on matrix diffusion behavior remains doubtful. However, if the specific suggestion on the experimental conditions does not present the expected cavitation phenomenon, investigation of the creep cavity in plain 12Cr steel and tungsten added 12Cr steel is recommended.

As a result, the absence of grain boundary cavities is attributed to the unfavorable dominating creep mechanism and relatively short lifetime for creep cavity nucleation and growth. In order to fully understand the reason for the absence of grain boundary cavities and to obtain suitable creep damage for self-healing demonstration, the following investigations are recommended: 1) Microstructural investigation of the coherence of matrix in the current samples; 2) Further lowering the testing stress; 3) Independent investigation on the effect of tungsten on the creep cavitation behavior in 12Cr steel, if the previous two investigations do not give satisfactory results.

6.3. Behavior of W-rich Laves Phase

The behavior of the W-rich Laves phase is discussed in this section as it is crucial for the evaluation of the self-healing effect and the design. The designed driving force of the Laves phase in FSHS is 4849 J/mol, which corresponds to a healing initiation time of 280 hours. The statistics of the W-rich Laves phase observed in FSHS show that the volume and number of the Laves phase precipitates in FSHS are positively related to the creep lifetime, as shown in Figure 5.34. Such time dependence is expected according to the design. The W-rich precipitates were observed in the samples with a lifetime of 465.3 hours and 2487.2 hours, while no W-rich precipitates were observed in the sample with 73.9 hours. It is important to note that the precipitation behavior of the W-rich Laves phase in the computational model was based on the driving force of homogeneous precipitation. The actual chemical driving force of FSHS calculated using the composition of the as-received samples listed in Table 4.1 is 4362 J/mol, which corresponds to a healing initiation time of approximately 900 hours. Thus, the experimentally observed precipitation

time of the W-rich Laves phase is generally consistent with the design. The statistics also show that the stress-affected region dramatically surpasses the stress-free area in terms of volume and number of the precipitates, indicating a positive effect of applied stress on the precipitation of the Laves phase.

SSHS is the self-healing steel with a lower driving force of tungsten precipitation and is expected to show the healing effect after 27000 hours in service. The W-rich Laves phase precipitates were observed at the grain boundaries in the stress-affected region of the SSHS sample with a lifetime of 307.5 hours and both the stress-affected and stress-free region of the SSHS sample with a lifetime of 1433.3 hours, while no bulk precipitates were observed. According to the design, the precipitation of the W-rich Laves phase at the grain boundaries is not expected, but the bulk precipitation behavior also corresponds with the timing-related design.

Nevertheless, the distribution of the W-rich Laves phase precipitates is different from the expectation of the design. The W-rich precipitates were observed in both matrix and grain boundaries without apparent site preference in the stress-affected region of the FSHS samples with a lifetime of 465.3 and 2487.2 hours, respectively. The precipitates generally have no connections with the defects reported in section 5.2.4. Therefore, no direct experimental evidence for the cavity filling behavior was found in the FSHS. As mentioned before, the precipitation site selectivity is essential for a successful self-healing material. One reason for lacking site selectivity is the absence of grain boundary cavities, which provide preferred nucleation sites for the healing precipitates. As discussed in the previous section, the absence of grain boundary cavities results from dislocation-dominated creep.

Based on the homogeneous precipitation of the Laves phase in the stress-affected region and the Laves phase precipitates observed in the stress-free region of FSHS with a lifetime of 2487.2 hours. Another reason for lacking site selectivity is the limited strain energy that failed to keep the tungsten within the matrix when there was no damage. In other words, the chemical driving force of the FSHS might be too high for the matrix. The equation used to calculate the strain energy resulting from the mismatch between the precipitate and the matrix can be described as equation 6-1 [122].

$$\Delta G_s = \frac{v_p \epsilon_v^2 E_p E_m}{3[2(1-2\nu_p)E_m + (1+\nu_m)E_p]} \tag{6.3}$$

In which E_p and E_m are Young's moduli of the precipitate and the matrix, ν_p and ν_m are the Poisson's ratios of the precipitate and the matrix, $\epsilon = v_p/v_m - 1$ is the volume misfit between the precipitate and the matrix, v_p and v_m are the molar volumes of the precipitate and the matrix phase. Taking $E_m = 205$ GPa, $\nu_m = 0.29$ [123], $E_p = 337$ GPa, $\nu_p = 0.29$ [124], the molar strain energies for thr precipitation of the W-rich Laves phase in the *bcc* matrix under equilibrium conditions at 550 °C for FSHS and and SSHS are calculated as 2690 J/mol and 2461 J/mol, respectively. The chemical driving force calculated based on the as-recieved composition for FSHS and SSHS are 4362 J/mol and 2208 J/mol, respectively. The chemical driving force for the precipitation of W-rich Laves phase in FSHS is clearly beyond the strain energy, resulting extensive precipitation in the stress-free region.

The linear distribution pattern parallel to the tensile direction could indicate that some sub-structures (e.g., dislocation lines or sub-grain boundaries) provide preferable sites for precipitation. The fine W-rich Laves phase precipitated in the matrix, and the grain boundaries might strengthen the material during the creep and provide another explanation for the "kink" shown in the lifetime-stress graph of FSHS (Figure 6.3).

As a result, the matrix precipitation timing of the W-rich Laves phase in the newly designed self-healing steels generally follows the innovative relationship between the chemical driving force and incubation time of the Laves phase used in this computational design, and the stress helps reduce the strain energy barrier of the precipitation as expected. However, the expected cavity filling phenomena are not found in FSHS due to the absence of grain boundary creep cavities and excessive driving force of the Laves phase precipitation.

7

Conclusion

According to the creep test result of FSHS and SSHS and comparison with traditionally designed 12Cr steel, the creep-resistant property of two newly designed 12Cr self-healing ferritic steels are comparable with traditional 12Cr steels and would surpass them if tested under lower stresses. The FSHS and SSHS also show a higher total strain and power-law exponents than traditional 12Cr steels. The SSHS obeys the Monkman-Grant relationship and modified Monkman-Grant relationship while FSHS disobeys, indicating a varying creep process for FSHS under current testing conditions. Such variation corresponds with the ”kink” shown in the lifetime-stress graph of FSHS and could be due to 1) Change of creep mechanism as the testing stress decreases; 2) Strengthening effect caused by fine W-rich Laves phase precipitation during the creep. The dominant creep mechanism for FSHS and SSHS is likely to be the dislocation-dominated creep under current testing conditions. The microstructural analysis reveals that the observed pores in fractured FSHS and SSHS samples are not caused by creep. Typical creep damage may not exist in all tested samples. The absence of typical creep damage is attributed to the unfavorable dominating creep mechanism and relatively short lifetime for creep cavity nucleation and growth.

The W-rich Laves phase behavior investigation shows that the matrix precipitation timing of the W-rich Laves phase in FSHS generally follows the computational design. Although W-rich Laves phase precipitates are observed in the stress-affected FSHS samples with a lifetime of 2487.2 hours and 465.3 hours, they present a homogeneous precipitation behavior and have no connections to the existing pores. Therefore, the expected self-healing phenomena are considered not found in FSHS under current testing conditions due to the absence of grain boundary cavities, so the prerequisite for self-healing is not fulfilled. The precipitates observed in the stress-free region of FSHS tested under 2487.2 hours, and the calculation of the strain energy caused by the mismatch between the precipitation and the matrix reveals that the precipitation driving force design might need amendments to obtain a sufficient site selectivity. However, the volume and number of W-rich Laves phase precipitate in stress-affected regions surpass the stress-free regions according to the precipitate statistics in FSHS. This means the stress is indeed lowering the strain energy barrier and promoting Laves phase to precipitate in the stress-affected regions.

Based on the findings in the newly designed 12Cr self-healing steels, several recommendations are proposed to fully understand the reason for the absence of grain boundary cavities and obtain suitable creep damage for self-healing demonstration. The recommendations are: 1) Microstructural investigation of the coherency of the matrix in the current samples; 2) Further lowering the testing stress; 3) Independent investigation of the effect of tungsten on the creep cavitation behavior in 12Cr steel if the previous two investigations do not give satisfactory results. Considering the homogeneous precipitation in FSHS and waste of healing agents in the stress-free region, an upper limit of the precipitation driving force is needed. Introducing the strain energy of the matrix could be one of the solutions. Besides, some cavity nucleation and growth models include simple relations between applied stress, temperature, and growth rate of creep cavity diameter. Including these parameters

as the timing reference for the precipitation could also help reduce the number of creep tests.

Acknowledgements

First, I would like to thank my dear supervisors, Sybrand, Niels, and Yifan, for their patient guidance and always inspiring ideas. This precious chance to work together led me into the beautiful world of material science and self-healing material systems, one of the most sophisticated research fields. As a mechanical student with weak knowledge in the material field, I appreciate the understandings that my supervisors taught me in the progress of this study. I want to thank my parents. They provide both physical and spiritual backup during my way of breaking through the difficulties. I would also like to thank my friends, both by my side and those far away. Your accompany also gives me great confidence in pursuing a master's degree. Thanks to other staff members and teachers of the faculty of aerospace. You provide an excellent environment for us to absorb the truth of the scientific world. Thank you all!

Bibliography

[1] F. Abe. "Research and Development of Heat-Resistant Materials for Advanced USC Power Plants with Steam Temperatures of 700 °C and Above". In: *Engineering* 1.2 (2015), pp. 211–224. ISSN: 2095-8099.

[2] Z. Zhang et al. "Perspectives for 700°C ultra-supercritical power generation: Thermal safety of high-temperature heating surfaces". In: *Energy* 190 (2020), p. 116411. ISSN: 0360-5442.

[3] R. L. Klueh and E. E. Bloom. "The development of ferritic steels for fast induced-radioactivity decay for fusion reactor applications". In: *Nuclear Engineering and Design. Fusion* 2.3 (1985), pp. 383–389. ISSN: 0167-899X.

[4] T. Noda et al. "Development of low activation ferritic steels". In: *Journal of Nuclear Materials* 141-143 (1986), pp. 1102–1106. ISSN: 0022-3115.

[5] S. J. Zinkle and G. S. Was. "Materials challenges in nuclear energy". In: *Acta Materialia* 61.3 (2013), pp. 735–758.

[6] Y. Yu. "Precipitation behavior and simulation on the high temperature service performance of g115 martensitic heat resistant steel". Thesis. Tsinghua University, 2021.

[7] N. Nabiran, S. Weber, and W. Theisen. "Influence of intermetallic precipitates and heat treatment on the mechanical properties of high-temperature corrosion resistant ferritic steels". In: *Procedia Engineering* 10 (2011), pp. 1651–1656. ISSN: 1877-7058.

[8] N. Nabiran, S. Weber, and W. Theisen. "Ferritic stainless steels for high-temperature applications: Stabilization of the microstructure by solid state precipitation of mx carbonitrides". In: *High Temperature Materials And Processes* 32.6 (2013), pp. 563–572. ISSN: 0334-6455 2191-0324 J9 - HIGH TEMP MAT PR-ISR.

[9] F. Abe. "Development of creep-resistant steels and alloys for use in power plants". In: *Structural Alloys for Power Plants: Operational Challenges and High-Temperature Materials*. Elsevier Inc., 2014, pp. 250–293.

[10] S. van der Zwaag. "Self-healing materials: An alternative approach to 20 centuries of materials science". In: *Chemistry International – Newsmagazine for IUPAC* 30.6 (2008), pp. 20–21.

[11] N. Kuhl et al. "Self-healing polymer networks based on reversible michael addition reactions". In: *Macromolecular Chemistry and Physics* 217.22 (2016), pp. 2541–2550. ISSN: 1022-1352.

[12] A. Fathy et al. "Properties of bacteria-induced self-healing mortar". In: *GEN* 56.1 (2014).

[13] R. Micaelo, T. Al-Mansoori, and A. Garcia. "Study of the mechanical properties and self-healing ability of asphalt mixture containing calcium-alginate capsules". In: *Construction and Building Materials* 123 (2016), pp. 734–744. ISSN: 0950-0618.

[14] H. Yu, W. Xu, and S. van der Zwaag. "A first step towards computational design of w-containing self-healing ferritic creep resistant steels". In: *Science and Technology of Advanced Materials* 21.1 (2020), pp. 641–652. ISSN: 1468-6996.

[15] T. H. Alden. "Strain hardening during low temperature creep of 304 stainless steel". In: *Acta Metallurgica* 35.11 (1987), pp. 2621–2626. ISSN: 0001-6160.

[16] M. E. Kassner. "Chapter 1 - Fundamentals of creep in materials". In: *Fundamentals of Creep in Metals and Alloys (Third Edition)*. Ed. by M. E. Kassner. Boston: Butterworth-Heinemann, 2015, pp. 1–6. ISBN: 978-0-08-099427-7.

[17] M. E. Kassner. "Chapter 2 - five-power-law creep". In: *Fundamentals of Creep in Metals and Alloys (Third Edition)*. Ed. by M. E. Kassner. Boston: Butterworth-Heinemann, 2015, pp. 7–102. ISBN: 978-0-08-099427-7.

[18] Frederick Harwood Norton. *The creep of steel at high temperatures*. McGraw-Hill Book Company, Incorporated, 1929.

[19] T. G. Langdon. "Creep". In: *Concise encyclopedia of advanced ceramic materials*. Ed. by R. J. Brook. Oxford: Pergamon, 1991, pp. 92–96. ISBN: 978-0-08-034720-2.

[20] M. A. Morris and J. L. Martin. "Microstructural dependence of effective stresses and activation volumes during creep". In: *Acta Metallurgica* 32.10 (1984), pp. 1609–1623. ISSN: 0001-6160.

[21] WD Nix and B Ilschner. "Strength of Metals and Alloys". In: *Proc. ICSMA*. Vol. 5, pp. 1507–30.

[22] B. K. Choudhary and E. Isaac Samuel. "Creep behaviour of modified 9cr–1mo ferritic steel". In: *Journal of Nuclear Materials* 412.1 (2011), pp. 82–89. ISSN: 0022-3115.

[23] V. Sklenička et al. "Long-term creep behavior of 9-12%cr power plant steels". In: *Materials Characterization* 51.1 (2003), pp. 35–48.

[24] F. Abe and S. Nakazawa. "The effect of tungsten on creep". In: *Metallurgical Transactions A* 23.11 (1992), pp. 3025–3034. ISSN: 1543-1940.

[25] R. Agamennone et al. "Evolution of microstructure and deformation resistance in creep of tempered martensitic 9–12% cr–2% w–5% co steels". In: *Acta Materialia* 54.11 (2006), pp. 3003–3014. ISSN: 1359-6454.

[26] K. Kimura, H. Kushima, and K. Sawada. "Long-term creep deformation property of modified 9cr-1mo steel". In: *Materials Science and Engineering A* 510-511.C (2009), pp. 58–63.

[27] R. Wu and R. Sandström. "Creep cavity nucleation and growth in 12cr–mo–v steel". In: *Materials Science and Technology* 11.6 (1995), pp. 579–588. ISSN: 0267-0836.

[28] R. Wu and R. Sandström. "Strain dependence of creep cavity nucleation in low alloy and 12%cr steels". In: *Materials Science and Technology* 12.5 (1996), pp. 405–415. ISSN: 0267-0836.

[29] B. J. Cane and G. W. Greenwood. "The nucleation and growth of cavities in iron during deformation at elevated temperatures". In: *Metal Science* 9.1 (1975), pp. 55–60.

[30] M. R. Ahmadi et al. "Modelling and simulation of diffusion driven pore formation in martensitic steels during creep". In: *Materials Science and Engineering: A* 712 (2018), pp. 466–477. ISSN: 0921-5093.

[31] M. E. Kassner. "Chapter 10 - Creep fracture". In: *Fundamentals of Creep in Metals and Alloys (Third Edition)*. Ed. by M. E. Kassner. Boston: Butterworth-Heinemann, 2015, pp. 233–260. ISBN: 978-0-08-099427-7.

[32] Rishi Raj and M. F. Ashby. "Intergranular fracture at elevated temperature". In: *Acta Metallurgica* 23.6 (1975), pp. 653–666. ISSN: 0001-6160.

[33] C. W. Chen and E. S. Machlin. "On the mechanism of intelcrystalline cracking". In: *Acta Metallurgica* 4.6 (1956), pp. 655–656. ISSN: 0001-6160.

[34] R. G. Fleck, D. M. R. Taplin, and C. J. Beevers. "An investigation of the nucleation of creep cavities by 1 MV electron microscopy". In: *Acta Metallurgica* 23.4 (1975), pp. 415–424. ISSN: 0001-6160.

[35] C. Gandhi and R. Raj. "Intergranular fracture in bicrystals—II". In: *Acta Metallurgica* 30.2 (1982), pp. 505–511. ISSN: 0001-6160.

[36] B. F. Dyson. "Continuous cavity nucleation and creep fracture". In: *Scripta Metallurgica* 17.1 (), pp. 31–38. ISSN: 0036-9748.

[37] B. F. Dyson. "Continuous cavity nucleation and creep fracture". In: *Scripta Metallurgica* 17.1 (1983), pp. 31–37. ISSN: 0036-9748.

[38] T. G. Nieh and W. D. Nix. "A comparison of the dimple spacing on intergranular creep fracture surfaces with the slip band spacing for copper". In: *Scripta Metallurgica* 14.3 (1980), pp. 365–368. ISSN: 0036-9748.

[39] J. N. Greenwood, D. R. Miller, and J. W. Suiter. "Intergranular cavitation in stressed metals". In: *Acta Metallurgica* 2.2 (1954), pp. 250–258. ISSN: 0001-6160.

[40] T. Watanabe and P. W. Davies. "Grain boundary sliding and intergranular fracture behaviour of copper bicrystals". In: *Philosophical Magazine A* 37.5 (1978), pp. 649–681. ISSN: 0141-8610.

[41] Josef Cadek. "Creep in metallic materials". In: *Materials Science Monographs* 48 (1988). ISSN: 0166-6010.

[42] A. Baldan. "On the creep rupture life prediction". In: *Journal of Materials Science* 33.14 (1998), pp. 3629–3637. ISSN: 1573-4803.

[43] B. Choi et al. "Characterization of the cavity nucleation factor for life prediction under creep-fatigue interaction". In: *Journal of Materials Science* 31.18 (1996), pp. 4957–4966. ISSN: 1573-4803.

[44] Y. Yu et al. "Correlation of creep fracture lifetime with microstructure evolution and cavity behaviors in G115 martensitic heat-resistant steel". In: *Materials Science and Engineering: A* 788 (2020), p. 139468. ISSN: 0921-5093.

[45] D. Hull and D. E. Rimmer. "The growth of grain-boundary voids under stress". In: *The Philosophical Magazine: A Journal of Theoretical Experimental and Applied Physics* 4.42 (1959), pp. 673–687. ISSN: 0031-8086.

[46] W. D. Nix, K. S. Yu, and J. S. Wang. "The effects of segregation on the kinetics of irrtergranular cavity growth under creep conditions". In: *Metallurgical Transactions A* 14.3 (1983), pp. 563–570. ISSN: 1543-1940.

[47] H. Riedel. *Fracture at high temperatures*. Springer, 2014. ISBN: 3642829619.

[48] I.-W. Chen. "Mechanisms of cavity growth in creep". In: *Scripta Metallurgica* 17.1 (1983), pp. 17–22. ISSN: 0036-9748.

[49] JW Hancock. "Creep cavitation without a vacancy flux". In: *Metal Science* 10.9 (1976), pp. 319–325. ISSN: 0306-3453.

[50] W. D. Nix. "Mechanisms and controlling factors in creep fracture". In: *Materials Science and Engineering: A* 103.1 (1988), pp. 103–110. ISSN: 0921-5093.

[51] F. Abe. "Progress in creep-resistant steels for high efficiency coal-fired power plants". In: *Journal of Pressure Vessel Technology, Transactions of the ASME* 138.4 (2016).

[52] K. Maruyama, K. Sawada, and J. Koike. "Strengthening Mechanisms of Creep Resistant Tempered Martensitic Steel". In: *ISIJ International* 41.6 (2001), pp. 641–653.

[53] M. Taneike, F. Abe, and K. Sawada. "Creep-strengthening of steel at high temperatures using nano-sized carbonitride dispersions". In: *Nature* 424.6946 (2003), pp. 294–296. ISSN: 1476-4687.

[54] M. Taneike, K. Sawada, and F. Abe. "Effect of carbon concentration on precipitation behavior of m23c6 carbides and mx carbonitrides in martensitic 9cr steel during heat treatment". In: *Metallurgical and Materials Transactions A* 35.4 (2004), pp. 1255–1262. ISSN: 1543-1940.

[55] F. Abe. "Precipitate design for creep strengthening of 9% cr tempered martensitic steel for ultra-supercritical power plants". In: *Science and Technology of Advanced Materials* 9.1 (2008), p. 013002. ISSN: 1468-6996.

[56] P. J. Ennis and A. Czyrska-Filemonowicz. "Recent advances in creep-resistant steels for power plant applications". In: *Sadhana* 28.3-4 (2003), p. 709. ISSN: 0973-7677 0256-2499.

[57] F. Abe, H. Araki, and T. Noda. "The effect of tungsten on dislocation recovery and precipitation behavior of low-activation martensitic 9cr steels". In: *Metallurgical Transactions A* 22.10 (1991), pp. 2225–2235. ISSN: 1543-1940.

[58] F. Abe. "Effect of fine precipitation and subsequent coarsening of fe2w laves phase on the creep deformation behavior of tempered martensitic 9cr-w steels". In: *Metallurgical and Materials Transactions A-physical Metallurgy and Materials Science - METALL MATER TRANS A* 36 (2005), pp. 321–332.

[59] L. Tan et al. "Microstructure control for high strength 9cr ferritic–martensitic steels". In: *Journal of Nuclear Materials* 422.1 (2012), pp. 45–50. ISSN: 0022-3115.

[60] J. Vanaja et al. "Effects of tungsten and tantalum on creep deformation and rupture properties of reduced activation ferritic-martensitic steel". In: *Procedia Engineering* 55 (2013), pp. 271–276. ISSN: 1877-7058.

[61] Y. Toda et al. "Effects of w and co on long-term creep strength of precipitation strengthened 15cr ferritic heat resistant steels". In: *ISIJ International* 43.1 (2003), pp. 112–118.

[62] Y. Chen et al. "Enhanced creep resistance of y-bearing 9cr ferritic/martensitic steel via vacuum casting technique". In: *Journal of Materials Research and Technology* 8.5 (2019), pp. 4588–4597.

[63] S. Kobayashi and T. Hara. "Effect of different precipitation routes of fe2hf laves phase on the creep rate of 9cr-based ferritic alloys". In: *Applied Sciences (Switzerland)* 11.5 (2021), pp. 1–13.

[64] B. K. Choudhary. "Tertiary creep behaviour of 9cr–1mo ferritic steel". In: *Materials Science and Engineering: A* 585 (2013), pp. 1–9. ISSN: 0921-5093.

[65] C. Cao et al. "Intermediate-temperature creep deformation and microstructural evolution of an equiatomic fcc-structured cocrfenimn high-entropy alloy". In: *Entropy* 20.12 (2018), p. 960. ISSN: 1099-4300.

[66] F. Abe et al. "The role of microstructural instability on creep behavior of a martensitic 9cr-2w Steel". In: *Metallurgical Transactions a-Physical Metallurgy and Materials Science* 23.2 (1992), pp. 469–477. ISSN: 0360-2133.

[67] *NIMS creep data Sheet No. 52A*. National Institute for Materials Science. Tokyo, Tsukuba, 2013.

[68] *NIMS creep data Sheet No. 48B*. National Institute for Materials Science. Tokyo, Tsukuba, 2018.

[69] *NIMS creep data Sheet No. 43A*. National Institute for Materials Science. Tokyo, Tsukuba, 2014.

[70] *NIMS creep data Sheet No. 9B*. National Institute for Materials Science. Tokyo, Tsukuba, 1990.

[71] *NIMS creep data Sheet No. 1B*. National Institute for Materials Science. Tokyo, Tsukuba, 1996.

[72] *NIMS creep data Sheet No. 3B*. National Institute for Materials Science. Tokyo, Tsukuba, 1986.

[73] *NIMS creep data Sheet No. 19B*. National Institute for Materials Science. Tokyo, Tsukuba, 1997.

[74] *NIMS creep data Sheet No. 13B*. National Institute for Materials Science. Tokyo, Tsukuba, 1994.

[75] K. Sawada, K. Kubo, and F. Abe. "Creep behavior and stability of MX precipitates at high temperature in 9Cr–0.5Mo–1.8W–VNb steel". In: *Materials Science and Engineering: A* 319-321 (2001), pp. 784–787. ISSN: 0921-5093.

[76] J. Hald. "Microstructure and long-term creep properties of 9–12% cr steels". In: *International Journal of Pressure Vessels and Piping* 85.1 (2008), pp. 30–37. ISSN: 0308-0161.

[77] A. Dronhofer, J. Pešička, and G. Eggeler. "On the relation between carbide density and grain boundary character in tempered martensite ferritic steels". In: *steel research international* 76.9 (2005), pp. 656–659. ISSN: 1611-3683.

[78] C. Herring. "Diffusional viscosity of a polycrystalline solid". In: *Journal of Applied Physics* 21.5 (1950), pp. 437–445.

[79] P. Caron and T. Khan. "Improvement of creep strength in a nickel-base single-crystal superalloy by heat treatment". In: *Materials Science and Engineering* 61.2 (1983), pp. 173–184. ISSN: 0025-5416.

[80] H. Kim and I. Kim. "Effect of austenitizing temperature on microstructure and mechanical properties of 12% cr steel". In: *ISIJ International* 34.2 (1994), pp. 198–204.

[81] K. S. Chandravathi et al. "Effect of isothermal heat treatment on microstructure and mechanical properties of Reduced Activation Ferritic Martensitic steel". In: *Journal of Nuclear Materials* 435.1 (2013), pp. 128–136. ISSN: 0022-3115.

[82] A. Dronhofer et al. "On the nature of internal interfaces in tempered martensite ferritic steels". In: *Zeitschrift Fur Metallkunde* 94.5 (2003), pp. 511–520. ISSN: 0044-3093.

[83] M. Hayakawa et al. "Observation of multi-scale structure for a creep-fatigued ferritic 12cr-2w steel". In: *Materials Transactions* 45.12 (2004), pp. 3291–3297.

[84] H. Wang et al. "On the 650 °C thermostability of 9–12cr heat resistant steels containing different precipitates". In: *Acta Materialia* 134 (2017), pp. 143–154.

[85] C. Mulyana et al. "Quantitative analysis of microstructure deformation in creep fenomena of ferritic sa-213 t22 and austenitic sa-213 tp304h material". In: *AIP Conference Proceedings* 1554.1 (2013), pp. 126–130.

[86] P. Kral et al. "The effect of ultrafine-grained microstructure on creep behaviour of 9% cr steel". In: *Materials* 11.5 (2018), p. 787. ISSN: 1996-1944.

[87] M. E. Abd El-Azim, O. H. Ibrahim, and O. E. El-Desoky. "Long term creep behaviour of welded joints of p91 steel at 650°C". In: *Materials Science and Engineering: A* 560 (2013), pp. 678–684. ISSN: 0921-5093.

[88] T. Hayashi et al. "Creep response and deformation processes in nanocluster-strengthened ferritic steels". In: *Acta Materialia* 56.7 (2008), pp. 1407–1416. ISSN: 1359-6454.

[89] J. Kyono and N. Shinya. "Self-healing of creep cavities formed in austenitic stainless steel". In: *Zairyo/Journal of the Society of Materials Science, Japan* 52.10 (2003), pp. 1211–1216.

[90] N. Shinya, J. Kyono, and K. Laha. "Self-healing effect of boron nitride precipitation on creep cavitation in austenitic stainless steel". In: *Journal of Intelligent Material Systems and Structures* 17.12 (2006), pp. 1127–1133.

[91] K. Laha et al. "Improved creep strength and creep ductility of type 347 austenitic stainless steel through the self-healing effect of boron for creep cavitation". In: *Metallurgical and Materials Transactions A* 36.2 (2005), pp. 399–409. ISSN: 1543-1940.

[92] N. Shinya, J. Kyono, and K. Laha. "Self-healing effect of b segregation on creep cavitation in type 347 austenitic stainless steel". In: *Zairyo/Journal of the Society of Materials Science, Japan* 55.3 (2006), pp. 317–322.

[93] S. Zhang, N. van Dijk, and S. van der Zwaag. "A review of self-healing metals: Fundamentals, design principles and performance". In: *Acta Metallurgica Sinica (English Letters)* 33.9 (2020), pp. 1167–1179. ISSN: 2194-1289.

[94] N. van Dijk and S. van der Zwaag. "Self-Healing Phenomena in Metals". In: *Advanced Materials Interfaces* 5.17 (2018), p. 1800226. ISSN: 2196-7350.

[95] S. M. He et al. "In situ determination of aging precipitation in deformed fe-cu and fe-cu-b-n alloys by time-resolved small-angle neutron scattering". In: *Physical Review B* 82.17 (2010), p. 174111.

[96] S. M. He et al. "Thermally activated precipitation at deformation-induced defects in fe-cu and fe-cu-b-n alloys studied by positron annihilation spectroscopy". In: *Physical Review B - Condensed Matter and Materials Physics* 81.9 (2010).

[97] S. M. He et al. "Positron annihilation study on repeated deformation/precipitation aging in fe-cu-b-n alloys". In: *Journal of Materials Science* 48.18 (2013), pp. 6150–6156. ISSN: 0022-2461.

[98] S. Zhang et al. "Positron annihilation study of ageing precipitation in deformed fe-cu-b-n-c". In: *Philosophical Magazine* 93.34 (2013), pp. 4182–4197. ISSN: 1478-6435.

[99] S. Zhang et al. "Self healing of creep damage by gold precipitation in iron alloys". In: *Advanced Engineering Materials* 17.5 (2015), pp. 598–603. ISSN: 1438-1656.

[100] S. Zhang et al. "Autonomous repair mechanism of creep damage in fe-au and fe-au-b-n alloys". In: *Metallurgical and Materials Transactions A* 46.12 (2015), pp. 5656–5670. ISSN: 1543-1940.

[101] H. Fang et al. "Autonomous filling of creep cavities in fe-au alloys studied by synchrotron x-ray nano-tomography". In: *Acta Materialia* 121 (2016), pp. 352–364. ISSN: 1359-6454.

[102] S. Zhang et al. "Defect-induced au precipitation in fe–au and fe–au–b–n alloys studied by in situ small-angle neutron scattering". In: *Acta Materialia* 61.18 (2013), pp. 7009–7019. ISSN: 1359-6454.

[103] S. Zhang et al. "Preferential au precipitation at deformation-induced defects in fe–au and fe–au–b–n alloys". In: *Journal of Alloys and Compounds* 584 (2014), pp. 425–429. ISSN: 0925-8388.

[104] S. Zhang et al. "Positron annihilation study on deformation-induced au precipitation in fe-au and fe-au-b-n alloys". In: *Journal of Materials Science* 49.6 (), pp. 2509–2518. ISSN: 0022-2461.

[105] S. Zhang et al. "Autonomous filling of grain-boundary cavities during creep loading in fe-mo alloys". In: *Metallurgical and Materials Transactions A* 47.10 (2016), pp. 4831–4844. ISSN: 1543-1940.

[106] H. Fang et al. "Self healing of creep damage in iron-based alloys by supersaturated tungsten". In: *Acta Materialia* 166 (2019), pp. 531–542. ISSN: 1359-6454.

[107] Y. Fu et al. "Competitive healing of creep-induced damage in a ternary fe-3au-4w alloy". In: *Metallurgical and Materials Transactions A* 51.9 (2020), pp. 4442–4455. ISSN: 1543-1940.

[108] H. Yu. "Computational design of high temperature alloys". Thesis. 2019.

[109] B. Xiao et al. "Tensile mechanical properties, constitutive equations, and fracture mechanisms of a novel 9% chromium tempered martensitic steel at elevated temperatures". In: *Materials Science and Engineering: A* 690 (2017), pp. 104–119. ISSN: 0921-5093.

[110] B. Xiao et al. "Microstructure evolution and fracture mechanism of a novel 9cr tempered martensite ferritic steel during short-term creep". In: *Materials Science and Engineering: A* 707 (2017), pp. 466–477. ISSN: 0921-5093.

[111] P. J. Ennis et al. "Microstructural stability and creep rupture strength of the martensitic steel P92 for advanced power plant". In: *Acta Materialia* 45.12 (1997), pp. 4901–4907. ISSN: 1359-6454.

[112] F. C. Monkman. "An empirical relationship between rupture life and minimum creep rate in creep rupture tests". In: *proc. ASTM*. Vol. 56, pp. 91–103.

[113] F. Dobeš and K. Milička. "The relation between minimum creep rate and time to fracture". In: *Metal Science* 10.11 (1976), pp. 382–384. ISSN: 0306-3453.

[114] S. Spigarelli, L. Kloc, and P. Bontempi. "Analysis of creep curves in a 9Cr-1Mo modified steel by means of simple constitutive equations". In: *Scripta Materialia* 37.4 (1997), pp. 399–404. ISSN: 1359-6462.

[115] E. Cerri et al. "Evolution of microstructure in a modified 9Cr–1Mo steel during short term creep". In: *Materials Science and Engineering: A* 245.2 (1998), pp. 285–292. ISSN: 0921-5093.

[116] P. J. Ennis et al. "Microstructural stability and creep rupture strength of the martensitic steel P92 for advanced power plant". In: *Acta Materialia* 45.12 (1997), pp. 4901–4907. ISSN: 1359-6454.

[117] B. K. Choudhary et al. "Creep-rupture behavior of forged, thick section 9Cr-1Mo ferritic steel". In: *Metallurgical and Materials Transactions A* 30.11 (1999), pp. 2825–2834. ISSN: 1543-1940.

[118] B. K. Choudhary. "Tensile, creep and low cycle fatigue behaviour of forged thick section 9Cr–1Mo ferritic steel". Thesis. 1997.

[119] E. Barker, G. J. Lloyd, and R. Pilkington. "Creep fracture of a 9Cr□1Mo steel". In: *Materials Science and Engineering* 84 (1986), pp. 49–64. ISSN: 0025-5416.

[120] B. J. Cane. "Creep fracture of dispersion strengthened low alloy ferritic steels". In: *Acta Metallurgica* 29.9 (1981), pp. 1581–1591. ISSN: 0001-6160.

[121] M. T. Perez-Prado and M. E. Kassner. "Chapter 3 - Diffusional Creep". In: *Fundamentals of Creep in Metals and Alloys (Third Edition)*. Ed. by M. E. Kassner. Boston: Butterworth-Heinemann, 2015, pp. 103–108. ISBN: 978-0-08-099427-7.

[122] D. Kashchiev. "Chapter 20 - Strain energy". In: *Nucleation*. Oxford: Elsevier, 2000. ISBN: 0080537839.

[123] ASM International. Handbook Committee. *ASM handbook*. Vol. 8. Asm International, 1990. ISBN: 0871703890.

[124] S. Yamasaki et al. "Evaluation of cleavage fracture behavior of c14 fe2w laves phase by first principle calculation and crystal orientation analysis". In: *Tetsu-To-Hagane/J. Iron Steel Inst.* 107.11 (2021), pp. 81–89. ISSN: 0021-1575.